

IMPROVING THE SIGNAL-TO-NOISE OF NANOPORE SENSORS

Matthew Puster

A DISSERTATION

in

Materials Science and Engineering

Presented to the Faculties of the University of Pennsylvania in Partial Fulfillment of the
Requirements for the Degree of Doctor of Philosophy

2015

Supervisor of Dissertation

Marija Drndić, Professor, Physics and Astronomy

Graduate Group Chairperson

Shu Yang, Professor, Materials Science and Engineering

Dissertation Committee

Cherie R. Kagan, Professor, Materials Science and Engineering

A.T. Charlie Johnson, Professor, Physics and Astronomy

Ritesh Agarwal, Professor, Materials Science and Engineering

UMI Number: 3709542

All rights reserved

INFORMATION TO ALL USERS

The quality of this reproduction is dependent upon the quality of the copy submitted.

In the unlikely event that the author did not send a complete manuscript and there are missing pages, these will be noted. Also, if material had to be removed, a note will indicate the deletion.



UMI 3709542

Published by ProQuest LLC (2015). Copyright in the Dissertation held by the Author.

Microform Edition © ProQuest LLC.

All rights reserved. This work is protected against unauthorized copying under Title 17, United States Code



ProQuest LLC.
789 East Eisenhower Parkway
P.O. Box 1346
Ann Arbor, MI 48106 - 1346

Dedicated to my parents,
to whom I am more grateful than words can express

Acknowledgements

I am fortunate to have had several mentors through the years, whose guidance has influenced the ideas, enthusiasm, and ambition that went into this thesis.

It all starts with my parents. I don't have a good explanation for it, but when you dig down to the roots, they are the ones to thank and blame.

Then I'd like to thank my mentors from a number of formative years in North Carolina: Laure McNeil, Yaakov Ariel, and Peter Kaufman. It's relationships like these that really shape a young student, and their influence will follow me regardless of what I undertake.

From the start of grad school there were several post-docs whom I looked up to for both guidance and inspiration. I'd like to thank Tali Dadosh, Ken Healy, Eric Lewandowski, Meni Wanunu, and Chris Merchant for taking me under their wing(s) in those early grad school years.

I've had the privilege to work closely with many other fantastic scientists from whom I am constantly learning new things. I'd specifically like to thank Julio A. Rodríguez-Manzo, Adrian Balan, Mike Fischbein, and Gaby Shemer. Many of the results

reported in this thesis were a direct result of work with them, but my thanks extend well beyond the lab.

Through almost seven years here I've been surrounded by friendly, open, and enthusiastic lab mates — Siying Wang, Vishva Ray, Jessamyn Fairfield, Lauren Willis, Kim Venta, David Niedzwiecki, and Will Parkin — whom I'd like to thank both for intense scientific discussions but also for making lab fun.

I'd also like to thank the Johnson lab, the Murray lab, and the Stebe lab for being welcoming neighbors, collaborators, and constant consultants.

And thanks to all the relative newcomers in the lab — Gopinath Danda, Jae-Hyuk Ahn, Chien Chen-Chi, Paul Masih Das, Ravit Dung, and Jothi Priyanka T. — for keeping up the mood and scientific rigor.

At this point we come full circle because all of these fantastic people find themselves in the same lab because of my advisor Marija Drndić. She is the unifying force who is constantly leading the lab in new and interesting directions. I would like to thank her for creating an atmosphere where it is possible to enjoy science and where I have had the freedom to think creatively and pursue new ideas. As she once said at a particularly stressful time: *this is as good as it gets!*

Last but certainly not least, I'd like to thank Kathleen Molnar for her overwhelming support.

ABSTRACT

IMPROVING THE SIGNAL-TO-NOISE OF NANOPORE SENSORS

Matthew Puster

Marija Drndić

Over the last five years, solid state nanopore technology advanced to rival biological pores as a platform for next generation DNA sequencing. Fabrication improvements led to a reduction in nanopore diameter and membrane thickness, offering high precision sensing. Custom electronics were developed concomitant with low capacitance membranes for low-noise, high-bandwidth measurements. These advances improved our ability to detect small differences between translocating molecules and to measure short molecules translocating at high speeds.

This work focuses specifically on the challenge of maximizing the signal magnitude generated by the solid state nanopore. One way that this can be achieved is by thinning the membrane. We prove that it is possible to differentiate between DNA homopolymers by using nanopores with < 6 nm thickness and < 2 nm diameter. The results imply that solid state nanopores offer higher signal-to-noise than what is currently achieved with biological pores.

Attempts to reduce membrane thickness further by making nanopores in 2D materials proved to be limited by wetting and noise considerations. Instead, we developed an electron-irradiation-based thinning technique to thin Si-based films to the limit of their stability in order to determine the intrinsic limit of their detection capabilities. At these small thicknesses, we discovered unexpected blocked current structure in the translocation events, which we hypothesize to be related to the DNA molecule blocking current flow before entering the nanopore.

Then we outline an alternative technique for high signal-to-noise single-molecule measurement by using a nanopore to localize the molecule near a charge sensor. The design of such a device required the development of a technique to make nanopores without damaging the sensor. Results from measurements of these devices in solution are reported, along with discussion of methods for improving the sensitivity.

In the last section we report on somewhat unrelated experiments that involve imaging charge flow through structured quantum dot films. We use a combination of AFM, EFM, and TEM to map the topography, charge flow, and structural features in high resolution. We show that charge flow patterns can be clearly correlated with structural details in the film.

Contents

Acknowledgements	iii
Abstract	v
List of Table	xii
List of Figures	xiii
Preface	xv
1 Introduction to Nanopores	1
1.1 Nanopores as an Analytic Tool	1
1.2 Solid State Nanopores	3
1.3 Measurement of Ionic Current through Nanopores	5
1.4 The Nanopore Circuit Diagram	7
1.5 Noise in Nanopores	8
1.6 Outline of Results	10
1.7 References	12

2	Thin Nanopore Sensors	15
2.1	Introduction	15
2.2	Methods	17
2.3	Homopolymer Discrimination with Thinned Silicon Nitride	20
2.4	Graphene and Boron Nitride Nanopore Sensors	26
2.5	On the Detection Limit of Ionic Conductance Variation through Silicon-Based Nanopores	29
2.5.1	STEM Thinning	30
2.5.2	MD Simulations to Determine the Minimum <i>a</i> -Si Membrane Thickness	34
2.5.3	Nanopore Formation in STEM	37
2.5.4	DNA Translocation Measurements of STEM Thinned Nanopores	39
2.5.5	Comparison with Literature Results	42
2.5.6	Data Trends for Small Nanopores in Thin Membranes	45
2.6	Prospectus on DNA Sequencing with Solid State Nanopores	48
2.7	References	50
3	Positioning a Charge Sensor Near the Nanopore	54
3.1	Introduction	54
3.2	Fabrication	57

3.2.1	Design Criteria and Challenges	57
3.2.2	Standard Graphene Nanoribbon Design	59
3.2.3	Alternative Graphene Nanoribbon Designs	62
3.3	Mechanism of Detection.	63
3.4	Nanopore Formation in STEM to Reduce Electron Damage	67
3.4.1	Damage to Graphene Ribbons in TEM	67
3.4.2	<i>In Situ</i> of Electron-Beam-Induced Damage	70
3.4.3	Nanopore Formation in STEM	73
3.4.4	Comparison of STEM and TEM Nanopore Drilling Methods .	76
3.5	Graphene Nanoribbon Measurements during DNA Translocation . .	79
3.5.1	Methods	79
3.5.2	Ribbon Detection Results	81
3.5.3	Circuit Simulation to Explain Correlation	85
3.6	Conclusions and Prospectus.	87
3.7	References	90
4	EFM Imaging of Charge Transport through Quantum Dot Arrays	93
4.1	Introduction	93
4.2	Theoretical Description of AFM Techniques	95
4.3	EFM Imaging Correlated with TEM and AFM	98
4.3.1	Methods	98

4.3.2	Results	99
4.4	Conclusions	107
4.5	References	108
Appendix A		111
Appendix B		113

List of Tables

2.1	Comparison of Solid State and Biological Nanopores	23
2.2	Comparison of RIE and STEM Thinning	29
2.3	Literature Results for Membrane Thicknesses < 10 nm	44

List of Figures

1.1	Comparison of Solid State and Protein Pores	2
1.2	Tilted Nanopore	4
1.3	Experimental Setup and Sample Translocations	6
2.1	TEM Images of Nanopores	16
2.2	TEM Images of Thinned Membranes	18
2.3	Homopolymer Differentiation Translocation Results	21
2.3	TEM Images of Boron Nitride Membranes	27
2.4	Quantitative STEM Thinning	32
2.5	AFM Image of STEM Thinning.	34
2.6	MD Simulations of Thin <i>a</i> -Si	36
2.7	Nanopores Made with STEM	38
2.8	Translocations through STEM Nanopores	40
2.9	Thin Membrane Translocation Trends	47
3.1	Graphene Nanoribbon Measurement Introduction	56
3.2	Graphene Hexagon Devices.	60
3.3	AFM Image of Graphene Nanoribbon	61

3.4	Graphene Nanoribbon Gate-Response Curve	66
3.5	Potential Field Calculations	66
3.6	Graphene Nanoribbon TEM Damage Bar Graph	67
3.7	TEM Image of Damage with ALD Layer	69
3.8	TEM Image of Damage, no ALD Layer	69
3.9	<i>In Situ</i> Measurement of Graphene Resistance upon TEM Beam Exposure in TEM-mode and STEM-mode	71
3.10	STEM Nanopore Formation Next to Graphene Nanoribbon	75
3.11	Graphene Nanoribbon STEM Damage Bar Graph	76
3.12	Comparison of Graphene Nanoribbon Electrical Properties after STEM and TEM Nanopore Drilling	78
3.13	PCB and Microfluidic Cell	80
3.14	DF-TEM Image of Graphene Nanoribbon and STEM Pore	80
3.15	Correlation of Ionic Translocation Signal and Graphene Ribbon Signal	83
3.16	Correlation of Ionic Translocation Signal and Graphene Ribbon Signal	84
3.17	PSD of Graphene Nanoribbon Current	85
3.18	Circuit Simulation	87
4.1	Modified AFM Stage	99
4.2	AFM and EFM Images of Bare Device	100
4.3	AFM and EFM Images of QD Film Before Annealing	101
4.4	AFM and EFM Images of QD Film After Annealing	102

4.5	Voltage Dependence of Charging	103
4.6	AFM / EFM / TEM Images Showing Limits to Charge Propagation . .	104
4.7	Wide Device Geometry, AFM / EFM / TEM	106
4.8	EFM Image Overlaid on TEM, Wide Gap	106
4.9	EFM Image Overlaid on TEM, Zoom-In	107

Preface

Many people contributed to the results reported in this thesis, and I would like to acknowledge their contributions.

In Chapter 2, Meni Wanunu and Tali Dadosh introduced the idea of thinning the membrane to our lab, and that idea has proven to be highly influential in the field and throughout my own work.

Kim Venta and Gaby Shemer led the team that worked on homopolymer differentiation. I contributed by calibrating the thinning technique, by making thinned samples and nanopores based on feedback from the experiments, and through discussions of the ionic current analysis and translocation statistics. This work was published in an ACS Nano paper [1].

For the 2D materials translocation experiments, many students in the Johnson lab helped with graphene growth over a number of years, and Ganghee Han in particular helped with the boron nitride growth.

The idea to use the electron beam in the TEM to thin samples was proposed by Julio A. Rodríguez-Manzo. Julio performed most of the TEM work in that study, while I performed the translocation measurements and analysis. Ken Healy wrote our custom

acquisition software for nanopore measurements. Our collaborators Vincent Meunier and Adrien Nicolai at RPI carried out the molecular dynamics simulations. We submitted these results for publication in Nano Letters [2].

In Chapter 3, several researchers were involved at various points in developing the procedures used for the graphene nanoribbon-nanopore devices, including Chris Merchant, Kim Venta, Adrian Balan, and Julio A. Rodríguez-Manzo. Paul Masih Das developed the recipes for the single-crystal graphene hexagons. Gautam Nagaraj spent a summer working on the new fluid cell design. Adrian Balan performed the circuit simulations. A first paper was published in ACS Nano on the topic of graphene nanoribbon damage in the TEM, and STEM formation of the nanopore without graphene damage [3]. A second paper on the translocation measurements, potential field calculations, and circuit simulations is in preparation [4].

In Chapter 4, Michael Fischbein introduced me to EFM, and we worked together on the measurements. That work was published in Nano Letters [5].

Published Works:

* indicates equal contribution

- [1] *Venta, K., *Shemer, G., **Puster, M.**, Rodríguez-Manzo, J.A., Balan, A., Rosenstein, J.K., Shepard, K. & Drndić, M., Differentiation of Short, Single-Stranded DNA Homopolymers in Solid-State Nanopores. *ACS Nano* **7**, 4629–4636 (2013).
- [2] *Rodríguez-Manzo, J. A., ***Puster, M.**, Nicolai, A., Meunier, V. & Drndić, M. On the Detection Limit of Ionic Conductance Variations Through Silicon-Based Nanopores. Submitted to *Nature Nano* (2015).
- [3] ***Puster, M.**, *Rodríguez-Manzo, J. A., *Balan, A. & Drndić, M. Toward Sensitive Graphene Nanoribbon–Nanopore Devices by Preventing Electron Beam-Induced Damage. *ACS Nano* **7**, 11283–11289 (2013).
- [4] **Puster, M.**, Balan, A., Rodríguez-Manzo, J. A. & Drndić, M. *In Preparation* (2015).
- [5] Fischbein, M. D., **Puster, M.** & Drndić, M. Monolayer Suppression of Transport Imaged in Annealed PbSe Nanocrystal Arrays. *Nano Lett.* **10**, 2155–2161 (2010).

Chapter 1

Introduction to Nanopores

1.1 Nanopores as an Analytic Tool

The development of nanopores as an analytic tool was in large part motivated by efforts to develop a next generation DNA sequencing technique with fast, direct sequence read-out from long DNA-fragment lengths without the need for labeling or enzymes.¹ As originally conceived, the measurement setup is similar to voltage-clamp measurements of ion channels in cell membranes; however, rather than measuring the opening and closing of ion channels made by pore-forming proteins in the cell membrane, a patch-clamp amplifier is used to apply a fixed voltage bias and record ionic current through a single protein channel with a fixed open state (frequently referred to as a biological nanopore), spanning an artificial lipid bilayer. DNA molecules injected into the electrolyte reservoir on one side of the membrane are electrophoretically driven through the pore, causing temporary blockades in ionic current flow.

In essence, this type of measurement is analogous to that of a Coulter Counter, which is used to measure the concentration and size of particles in electrolyte. The frequency of current blockade events gives information about the concentration of the particles, and the magnitude of blocked current reveals information about the size of the particles.

The first nanopore measurements of DNA for applications in sequencing employed α -hemolysin protein pores, with inner diameters just larger than a single-stranded DNA molecule (ssDNA) (Fig. 1.1a).²⁻⁴ Other protein pores were engineered for specific shapes and residues, and the MspA pore in particular (Fig. 1.1c) proved capable of distinguishing between DNA nucleotides when combined with a polymerase that ratchets the DNA through the pore.^{5,6} While these results are the most exciting nanopore proof-of-principle sequencing results to date, the future of the field may lie in equivalent solid state nanopores (Fig. 1.1b).

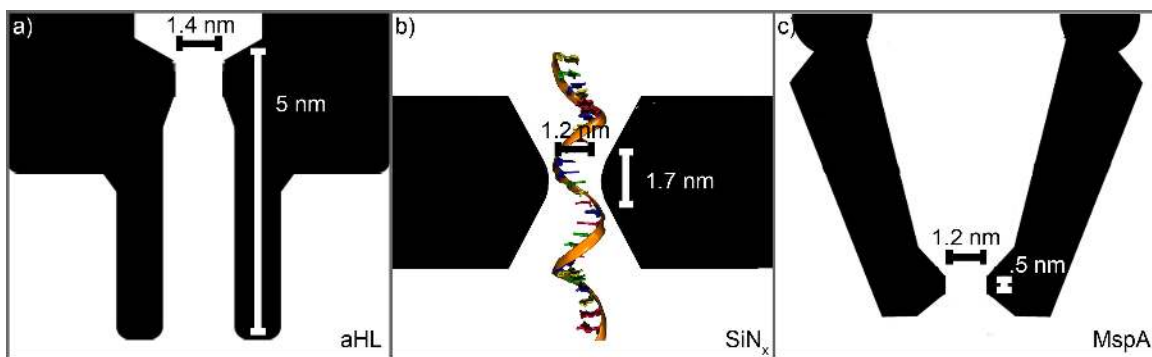


Figure 1.1. Protein pores a) α -hemolysin and c) MspA. b) Thin solid state silicon nitride pore with an hourglass shape. The images are drawn to be on the same scale.⁷

1.2 Solid State Nanopores

A solid state nanopore is a synthetic pore in a solid, thin, suspended film, modeled after the biological nanopores α -hemolysin and MspA in a lipid bilayer. These pores have traditionally been made in suspended silicon nitride (SiN_x) membranes, which are fabricated as $50 \times 50 \mu\text{m}$ windows on $5 \times 5 \text{ mm}$ chips, each of which contains a single membrane. The chips are patterned using standard photolithography and etching procedures on $50 \text{ nm SiN}_x / 5 \mu\text{m SiO}_2 / 500 \mu\text{m}$ doped Si wafers. The SiO_2 layer reduces capacitance across the membrane. These types of membranes are commonly used as substrates for transmission electron microscope (TEM) imaging.

Nanopores can be formed with a variety of techniques that involve ablating or sputtering a small hole in the membrane, including irradiation with Argon ions,⁸ Ga^+ ions in a conventional focused-ion beam (FIB) instrument,⁹ helium ions in a helium-ion microscope,¹⁰ or electrons in a TEM.¹¹ All of the nanopores measured in this thesis – typically 1–5 nm in diameter – were made using the condensed electron beam of the TEM, which can produce the smallest nanopores (the diameter of a single stranded DNA molecule is roughly 1.1 nm). The process of forming the pore in the TEM takes seconds to minutes, depending on the membrane thickness.

Whereas a functioning biological pore is engineered to have a specific size and shape, a solid state nanopore offers flexibility in its dimensions and can be tailored to fit the molecule of study. To make larger diameters, we simply increase the electron beam dwell time, probe size, or beam current in the TEM. By adjusting the beam convergence

angle and membrane composition and thickness we can also tailor the pore shape from an hourglass structure¹² to a truncated cone (Fig. 1.2), or for thin films, to a cylinder. In addition, solid state nanopores allow for a wide range in pH, electrolyte concentration, temperature, and voltage bias.

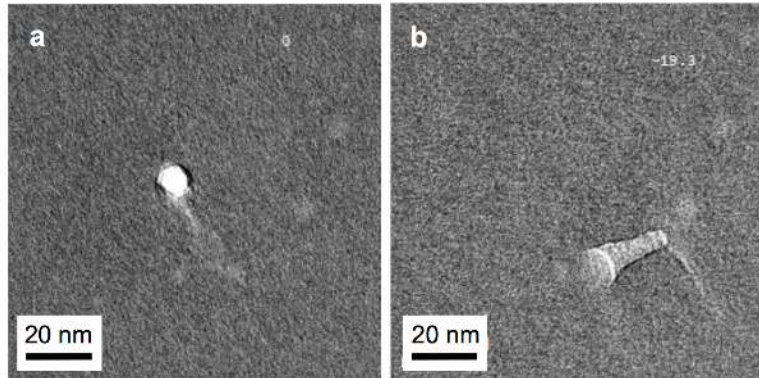


Figure 1.2. a) Pore formed in Scanning-TEM (STEM) in a 100 nm silicon nitride film. b) Pore from (a) at -19.3° tilt to show truncated cone pore shape.

An illustration of the dimensions of a thin solid state nanopore in comparison to α -hemolysin and MspA is shown in Fig. 1.1.⁷ Only recently have techniques been developed to scale both the membrane thickness and pore size down to the dimensions of the biological pores. In principle, one might expect comparable ionic current levels and resolution from a solid state nanopore of the same inner dimensions as a biological pore, but in fact the measured current levels are 2 to 10 times higher for solid state nanopores for similar measurement conditions. Our work toward this end is highlighted in two papers^{7,13} and will be discussed in Chapter 2.

1.3 Measurement of Ionic Current through Nanopores

Once the pore is formed in the TEM, the piece of wafer containing the nanopore (Fig. 1.3b) is inserted into a home-built PDMS microfluidic cell which feeds electrolyte to each side of the membrane (Fig. 1.3c). The single pore in the membrane separates reservoirs of electrolyte on either side and serves as a channel for molecules to pass from one reservoir to the other. A patch-clamp amplifier is used to apply a constant voltage bias across the membrane and measure the ionic current flow through the pore (depicted in Fig. 1.3a). DNA fragments (either single-stranded or double-stranded) are added to one electrolyte reservoir, and under the applied field, they are driven through the pore. When a DNA molecule enters the pore, there is a reduction in the ionic current flow, and once the molecule is driven fully through the pore, the current returns to its open pore state. Typical ssDNA translocation events are shown in Fig. 3d-e.⁷

Standard concentrations of DNA used in translocation experiments are 1-10 nM, typically in 1 M KCl + 10 mM Tris + 1 mM EDTA at pH ~ 7.5, and the segments range from 25 base pairs (25 bp) to 48,000 base pairs (48 kbp). The duration of each event varies from tens of microseconds to milliseconds,¹⁴ depending on the length of molecule, thickness of pore, and applied voltage (0.1–1 V). Among many applications, this technique has been used to measure concentrations of miRNA,¹⁵ to characterize the binding of RNA-antibiotic complexes,¹⁶ to diagnose modifications to cytosine in DNA fragments (differentiating between methylation and hydroxymethylation),¹⁷ to detect an HIV biomarker,¹⁸ and to determine the surface charge on colloidal nanoparticles.¹⁹

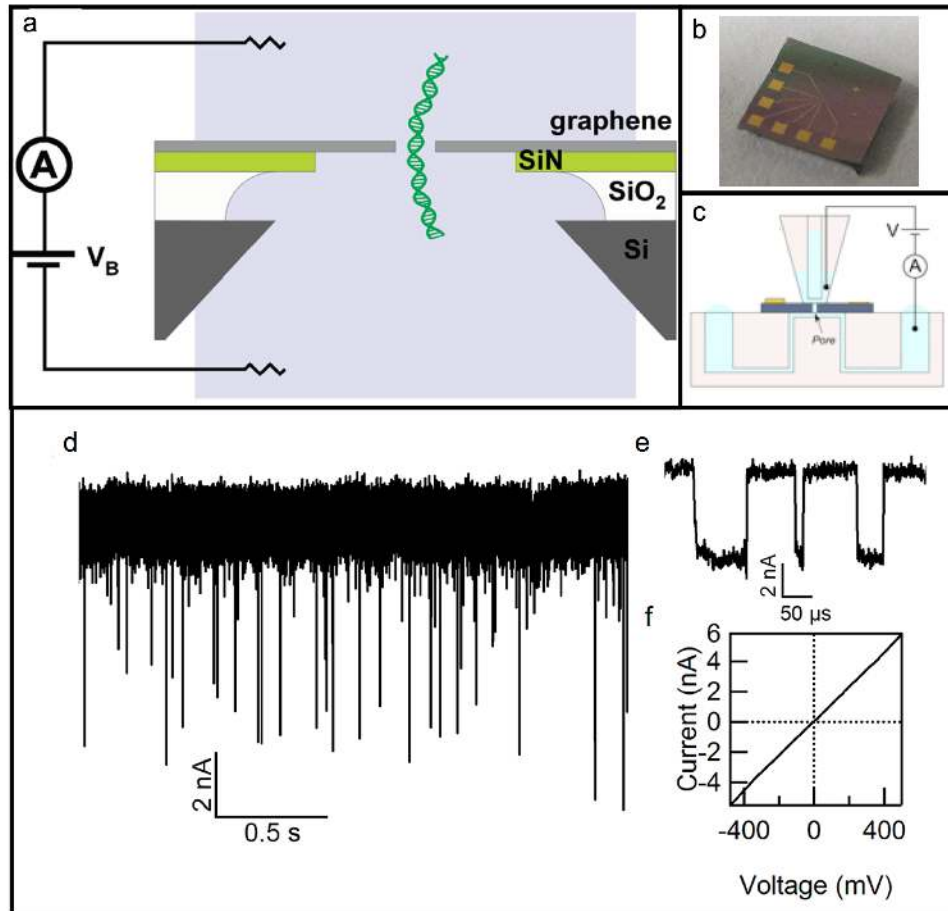


Figure 1.3. a) Diagram depicting a nanopore in a thin membrane (in this case graphene). b) Image of 5×5 mm wafer containing the SiN_x membrane in the center and large gold contacts leading to a graphene device (to be discussed in Chapter 3). c) Schematic of home-built PDMS microfluidic cell that guides buffered salt solution to both sides of the membrane. d) Ionic current through the pore plotted as a function of time.⁷ When the ssDNA enters the pore, there is a blockade of, on average, 3 nA (25%). The diameter of this pore is 2.4 nm and the membrane thickness is 7.6 nm. The open-pore baseline current is 12 nA. e) Zoom-ins of three individual translocation events. f) Current vs. voltage curve showing Ohmic resistance.

1.4 The Nanopore Circuit Diagram

The current through the nanopore as a function of voltage is shown in Fig. 1.3f. A cylindrical nanopore is characterized by an ohmic resistance where:

$$R_{pore} = \frac{t}{\sigma A} = \frac{4t}{\sigma \pi d^2} \quad (1.1)$$

t is the membrane thickness, d is the nanopore diameter, A is the nanopore cross-sectional area, and σ is the electrolyte conductivity.

In series with the nanopore resistance on both sides of the membrane is the access resistance,²⁰ which is associated with ion entry into the small circular cross-sectional area of pore:

$$R_{access} = \frac{1}{2\sigma d} \quad (1.2)$$

Therefore the total nanopore conductance through a cylindrical pore (*i.e.* the open pore conductance), neglecting surface charge effects, can be described as²¹

$$G_0 = \frac{1}{R_{tot}} = \sigma \left(\frac{4t}{\pi d^2} + \frac{1}{d} \right)^{-1} \quad (1.3)$$

The access resistance term becomes prominent when the diameter of the nanopore is close to or larger than the thickness of the film. This was first observed for very large pores²¹ but also becomes important for small pores in very thin films (as we will describe in Chapter 2).

When the DNA molecule enters the pore, the change in ionic conductance can be described as $\Delta G = G_0 - G_{with\ molecule}$,

$$G_{\text{with molecule}} = \sigma \left(\frac{4t}{\pi(d^2 - d_{DNA}^2)} + \frac{1}{\sqrt{d^2 - d_{DNA}^2}} \right)^{-1} \quad (1.4)$$

where $G_{\text{with molecule}}$ is the conductance when the nanopore is partially blocked by the translocating molecule, observed as a conductance drop (Fig. 1.3d). Here Eq. 1.3 is modified such that the diameter is now defined as the diameter of an equivalent pore that matches the area unoccupied by the DNA molecule.

Equations 1.1 through 1.4 do a good job at capturing the dynamics of current flow through a cylindrical nanopore to first order at high salts and will be used mainly as a guide for intuition in the following sections, rather than as a rigorous model. Several modifications to this model have been proposed based on experimental evidence — including the incorporation of pore shape,²¹ surface charge, and counter-ions around the molecule²² — but in general the models converge for small membrane thicknesses and nanopore diameters, and experimental measurements lack the precision in estimates of the physical shape and dimensions of the nanopore to truly discriminate between the finer differences of the models.

1.5 Noise in Nanopores

The current noise in solid state nanopore measurements is comprised of roughly three regimes: 1) high $1/f$ noise, associated with low frequency fluctuations in the ionic

current, that falls with increasing frequency to the thermal noise floor around 100 Hz, 2) a lower thermal noise in the range of 100–10,000 Hz, and 3) a high frequency noise, increasing with frequency beyond 10 kHz, dominated by the capacitance of the membrane and Si-wafer, which amplify the voltage noise from the amplifier.²³⁻²⁹

The increasing capacitive noise at high frequencies is the predominant bandwidth limitation for solid state nanopores. The magnitude of the conductance blockades ΔG (or ΔI , since $\Delta G = \Delta I / V$) dictate the tolerance to noise and thereby the maximum measurement bandwidth and minimum time resolution. Bandwidths of up to 100 kHz can be measured with conventional patch-clamp amplifiers, and a custom amplifier developed by collaborators in the Shepard lab (Columbia University) offers measurement bandwidths up to 1 MHz for ultra-low capacitance membranes.^{7,29,30} Thus, methods to enhance ΔG and reduce capacitance (and other sources of noise) are both active research fields within the solid state nanopore community.

The ultimate promise for solid state nanopores is to record larger ΔG magnitudes than biological pores (possible because of the larger voltage range and apparently, higher intrinsic conductances), with sufficiently low noise such that it is possible to resolve nucleotides (or combinations of nucleotides) without slowing the DNA molecule down during translocation (biological pores utilize a polymerase, which ratchets the DNA through the pore, to slow the translocation and allow for measurements at lower bandwidths for lower noise). A solid state nanopore platform with a membrane thickness of four DNA bases (~ 1.3 nm) featuring ~10 MHz bandwidth electronics, with the most recent noise reduction techniques,³⁰ and discrete signals for all possible combinations of

the four DNA bases,⁶ could conceivably sequence an entire human genome in minutes, without the need to slow down the molecule translocation speed of $\sim 10^7$ bases per second. However, because of the ease of tuning the nanopore dimensions, the applications for solid state nanopores extend well beyond sequencing as well.

1.6 Outline of Results

In this thesis, I outline two broad approaches to obtain improved signal-to-noise from nanopore measurements that will allow us to measure faster and to more easily discriminate between nucleotides.

For the first approach, which will be described in Chapter 2, SiN_x membranes were thinned with a reactive-ion etch (RIE) and nanopores were made with diameters just larger than a single stranded DNA molecule (ssDNA). By thinning the nanopore membrane, R_{pore} is reduced and both G_0 and ΔG increase, without significant increase in noise. With these nanopores, on the same scale as biological pores, we were able to discriminate between short homopolymers of the different nucleotides (the first such proof for solid state nanopores).⁷ Those thinned membranes also improve the spatial resolution, allowing for measurement of shorter molecules or of structure within the translocating molecule.

Then, to explore the limits of ΔG in Si-based nanopores, we developed a technique for thinning the membrane using electrons, which provides enough precision to

thin SiN_x membranes to the limit of their structural stability, as determined by MD simulations. The resulting films provide the upper limit of ΔG in Si-based nanopores, and show that Si-based pores perform as well as any 2D material.

The second approach, which will be described in Chapter 3, involves developing a new technique to detect nucleotides electronically with a graphene nanoribbon charge sensor next to the pore. The nanopore serves as a means to localize the DNA near the detector, which has an active layer that is the same thickness as the spacing between nucleotides along the DNA backbone (~ 0.3 nm). Each nucleotide is predicted to perturb the electrostatic potential uniquely such that, as the DNA molecule translocates through the pore, the DNA sequence could be read as modulations in the conductance of the ribbon.³¹⁻³⁴ Electronic detection has the potential to exhibit higher signal-to-noise than traditional nanopore ionic current measurements and would allow us to measure at higher bandwidths than any previous ionic nanopore measurement.

1.7 References

1. Branton, D. *et al.* The potential and challenges of nanopore sequencing. *Nat Biotechnol* **26**, 1146–1153 (2008).
2. Bezrukov, S. & Kasianowicz, J. Current noise reveals protonation kinetics and number of ionizable sites in an open protein ion channel. *Phys. Rev. Lett.* **70**, 2352–2355 (1993).
3. Kasianowicz, J. J. & Bezrukov, S. M. Protonation dynamics of the alpha-toxin ion channel from spectral analysis of pH-dependent current fluctuations. *Biophysj* **69**, 12–12 (1995).
4. Song, L. *et al.* Structure of staphylococcal α -hemolysin, a heptameric transmembrane pore. *Science* **274**, 1859–1865 (1996).
5. Butler, T. Z., Pavlenok, M., Derrington, I. M., Niederweis, M. & Gundlach, J. H. Single-molecule DNA detection with an engineered MspA protein nanopore. *Proc Natl Acad Sci U S A* **105**, 20647–20652 (2008).
6. Manrao, E. A. *et al.* Reading DNA at single-nucleotide resolution with a mutant MspA nanopore and phi29 DNA polymerase. *Nat Biotechnol* **30**, 349–353 (2012).
7. Venta, K., Shemer, G., Puster, M. *et al.* Differentiation of Short, Single-Stranded DNA Homopolymers in Solid-State Nanopores. *ACS Nano* **7**, 4629–4636 (2013).
8. Li, J. *et al.* Ion-beam sculpting at nanometre length scales. *Nature* **412**, 166–169 (2001).
9. Lo, C. J., Aref, T. & Bezryadin, A. Fabrication of symmetric sub-5 nm nanopores using focused ion and electron beams. *Nanotechnology* **17**, 3264–3267 (2006).
10. Yang, J. *et al.* Rapid and precise scanning helium ion microscope milling of solid-state nanopores for biomolecule detection. *Nanotechnology* **22**, 285310 (2011).
11. Storm, A. J., Chen, J. H., Ling, X. S., Zandbergen, H. W. & Dekker, C. Fabrication of solid-state nanopores with single-nanometre precision. *Nat Mater* **2**, 537–540 (2003).

12. Kim, M. J., Wanunu, M., Bell, D. C. & Meller, A. Rapid Fabrication of Uniformly Sized Nanopores and Nanopore Arrays for Parallel DNA Analysis. *Adv. Mater.* **18**, 3149–3153 (2006).
13. Rodriguez-Manzo, J. A., Puster, M., Nicolai, A., Meunier, V. & Drndic, M. On the Detection Limit of Ionic Conductance Variations Through Silicon-Based Nanopores. *Submitted to Nano Letters* (2015).
14. Storm, A. J. *et al.* Fast DNA Translocation through a Solid-State Nanopore. *Nano Lett.* **5**, 1193–1197 (2005).
15. Wanunu, M. *et al.* Rapid electronic detection of probe-specific microRNAs using thin nanopore sensors. *Nature Nanotech* **5**, 807–814 (2010).
16. Wanunu, M. *et al.* Nanopore Analysis of Individual RNA/Antibiotic Complexes. *ACS Nano* **5**, 9345–9353 (2011).
17. Wanunu, M. *et al.* Discrimination of Methylcytosine from Hydroxymethylcytosine in DNA Molecules. *J. Am. Chem. Soc.* **133**, 486–492 (2011).
18. Niedzwiecki, D. J., Iyer, R., Borer, P. N. & Movileanu, L. Sampling a biomarker of the human immunodeficiency virus across a synthetic nanopore. *ACS Nano* **7**, 3341–3350 (2013).
19. Venta, K. E. *et al.* Gold nanorod translocations and charge measurement through solid-state nanopores. *Nano Lett.* **14**, 5358–5364 (2014).
20. Hall, J. E. Access resistance of a small circular pore. *The Journal of general physiology* **66**, 531–532 (1975).
21. Kowalczyk, S. W., Grosberg, A. Y., Rabin, Y. & Dekker, C. Modeling the conductance and DNA blockade of solid-state nanopores. *Nanotechnology* **22**, 315101 (2011).
22. Carlsen, A. T., Zahid, O. K., Ruzicka, J., Taylor, E. W. & Hall, A. R. Interpreting the conductance blockades of DNA translocations through solid-state nanopores. *ACS Nano* **8**, 4754–4760 (2014).
23. Tabard-Cossa, V., Trivedi, D., Wiggin, M., Jetha, N. N. & Marziali, A. Noise analysis and reduction in solid-state nanopores. *Nanotechnology* **18**, 305505 (2007).

24. Smeets, R. M. M., Keyser, U. F., Dekker, N. H. & Dekker, C. Noise in solid-state nanopores. *Proceedings of the National Academy of Sciences* **105**, 417–421 (2008).
25. Smeets, R. M. M., Dekker, N. H. & Dekker, C. Low-frequency noise in solid-state nanopores. *Nanotechnology* **20**, 095501 (2009).
26. Hoogerheide, D. P., Garaj, S. & Golovchenko, J. A. Probing Surface Charge Fluctuations with Solid-State Nanopores. *Phys. Rev. Lett.* **102**, 256804 (2009).
27. Beamish, E., Kwok, H., Tabard-Cossa, V. & Godin, M. Precise control of the size and noise of solid-state nanopores using high electric fields. *Nanotechnology* **23**, 405301 (2012).
28. Sakmann, B. & Neher, E. *Single Channel Recording*. (Springer, 2009).
29. Rosenstein, J. K., Wanunu, M., Merchant, C. A., Drndic, M. & Shepard, K. L. Integrated nanopore sensing platform with sub-microsecond temporal resolution. *Nat Meth* **9**, 487–492 (2012).
30. Balan, A. *et al.* Improving Signal-to-Noise Performance for DNA Translocation in Solid-State Nanopores at MHz Bandwidths. *Nano Lett.* **14**, 7215–7220 (2014).
31. Nelson, T., Zhang, B. & Prezhdo, O. V. Detection of Nucleic Acids with Graphene Nanopores: Ab Initio Characterization of a Novel Sequencing Device. *Nano Lett.* **10**, 3237–3242 (2010).
32. Avdoshenko, S. M. *et al.* Dynamic and Electronic Transport Properties of DNA Translocation through Graphene Nanopores. *Nano Lett.* **13**, 1969–1976 (2013).
33. Saha, K. K., Drndic, M. & Nikolić, B. K. DNA Base-Specific Modulation of Microampere Transverse Edge Currents through a Metallic Graphene Nanoribbon with a Nanopore. *Nano Lett.* **12**, 50–55 (2012).
34. Girdhar, A., Sathe, C., Schulten, K. & Leburton, J.-P. Graphene quantum point contact transistor for DNA sensing. *Proceedings of the National Academy of Sciences* **110**, 16748–16753 (2013).

Chapter 2

Thin Nanopore Sensors

2.1 Introduction

Solid state nanopores were envisioned as a solid state analogue to biological nanopores nearly 15 years ago,¹ but only in the last five years have they been scaled down to those physical dimensions.² As a point of comparison, a conventional 50 nm thick SiN_x membrane is ten times thicker than a lipid bilayer (~ 5 nm). A 10 nm diameter pore in a 50 nm membrane allows DNA molecules to translocate in folded configurations, with more than a hundred bases in the pore at a time.

Thin membrane materials provide two distinct advantages: 1) the spatial resolution is improved because there is physically a smaller length of the molecule inside the nanopore at once, and 2) the magnitude of the blocked current as the molecule translocates through the pore (ΔI) increases relative to the noise, in essence improving the signal-to-noise ratio of the measurement.

The origin of the ΔI enhancement is rooted in the reduction in the resistance for ion flow through the pore (R_{pore}) upon thinning. At a given voltage, a decrease in R_{pore} produces an increase in the open-pore current (I_0). If we assume that the percentage of current blocked by a translocating molecule (% blocked) is constant for a fixed nanopore diameter, regardless of thickness, (*n.b.* this is an approximation) then as the thickness decreases and I_0 increases, ΔI increases proportionally ($\Delta I = I_0 \times (\% \text{ blocked})$).² Thin films show larger capacitance during the nanopore measurement, but if the thinned area is small, that increase in capacitance is negligible, and the increase in ΔI is greater than the increase in capacitive noise.

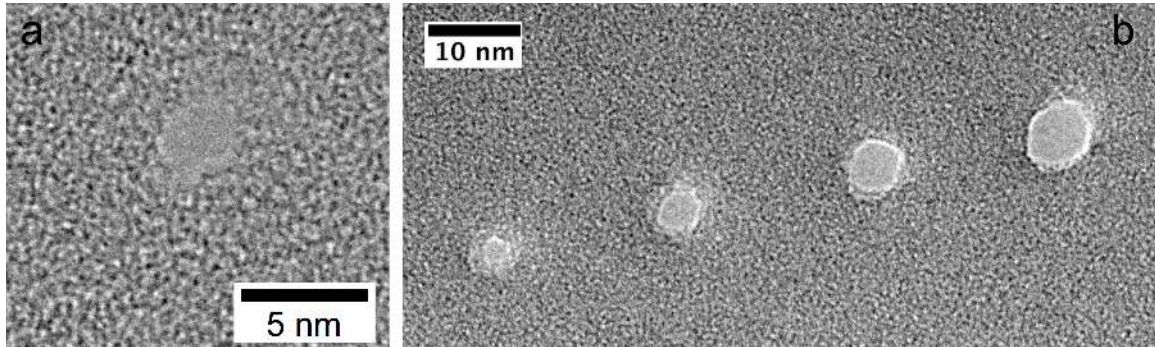


Figure 2.1. TEM images of nanopores made using the condensed electron beam in TEM-mode. a) 2.4 nm nanopore in a 5 nm membrane, b) four nanopores of different diameters in a 50 nm membrane, illustrating the control over size possible with the TEM.

Currently the only method to consistently produce a solid state nanopore as small in diameter as biological pores (< 1.5 nm) is with the electron beam in a field-emission TEM, which offers both high magnification (on a JEOL 2010F operated at 200 kV, we routinely use 1.5 million times magnification) and small probe size (0.5 nm probe is a

standard choice). A series of pores of different sizes made using the TEM are shown in Fig. 2.1.

Membrane thicknesses on the scale of a lipid bilayer were first reproducibly made by Wanunu, *et al.*² by thinning 250 nm × 250 nm squares on the SiN_x membrane from a thickness of 50 nm down to 6 nm with a reactive ion etch (RIE). Later, a He-ion beam was used to thin SiN_x down to comparable levels,^{3,4} and thin ALD films of HfO₂ were grown and then suspended by etching the supporting layer.⁵ At the same time, three papers were published showing translocations through nanopores in suspended graphene membranes.⁶⁻⁸ At ~ 0.3 nm, the thickness of graphene is almost exactly the spacing between nucleotides along the DNA backbone.

In the following sections I will show that when the nanopore size is brought down to the size of biological pores, it is possible to differentiate between DNA homopolymers, and that the differences between nucleotide signals are actually larger than those measured with biological pores. Then we examine the limit of detection with Si-based nanopores and compare it with published results from other materials in the literature.

2.2 Methods

Following the procedure outlined by Wanunu, *et al.*,² 150 nm × 150 nm squares were defined with electron beam lithography in PMMA resist spun on the SiN_x membrane and then etched using a reactive ion etch from a thickness of 50 nm down to 5

nm (Fig. 2.2a-c). Film thicknesses were calibrated using an AFM to measure the etched step height as a function of etch time. With RIE, we found the limit of thinning for SiN_x to be ~ 5 nm. Films thinner than ~ 5 nm are unstable in the TEM and disintegrate or crumble upon exposure to even low doses of the spread electron beam (Fig. 2.2d,e).

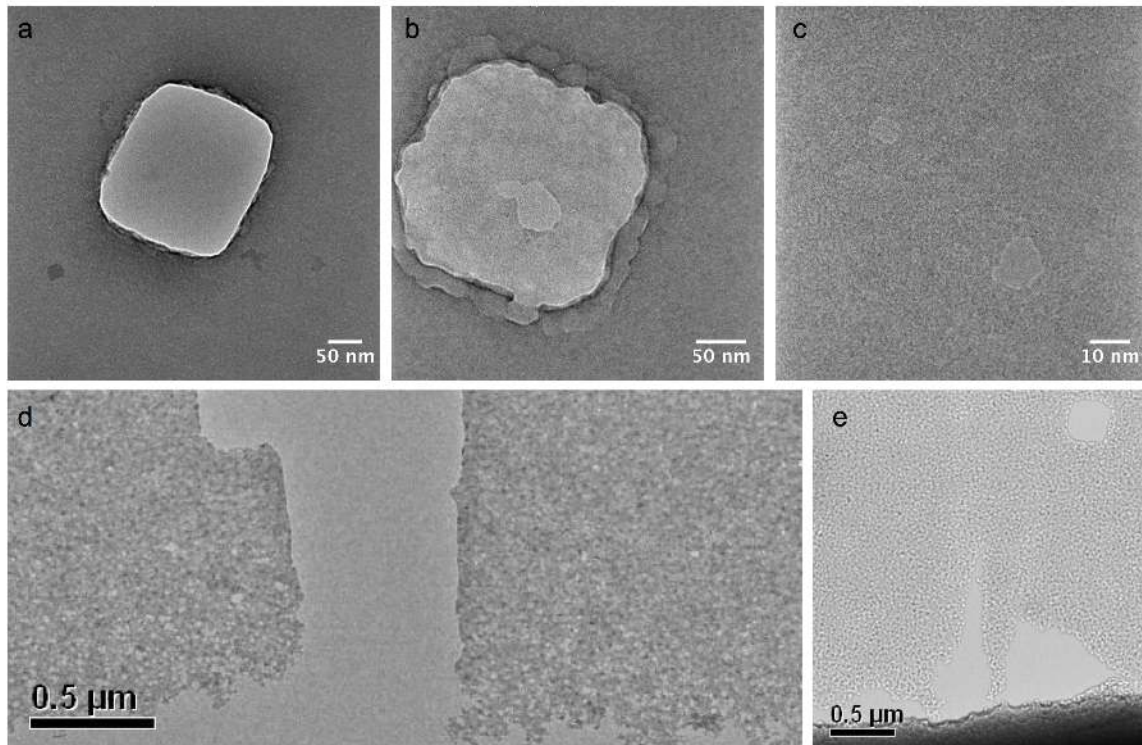


Figure 2.2. a) TEM image of a region of SiN_x thinned by RIE, b) large pore in thinned region, c) two smaller pores in thinned region, d) a crack that formed in a membrane thinned below ~ 5 nm, e) voids in another membrane thinned below ~ 5 nm.

For the homopolymer differentiation measurements, nanopores were drilled in standard TEM imaging mode (bright-field imaging) by condensing the beam to a point on the membrane at the maximum magnification (1.5 million times magnification). Upon condensing the beam, nanopores formed immediately. To prevent pore expansion, most pores were not imaged. Nanopore size was estimated based on markers on the TEM

fluorescent screen before immediately closing the beam-valve. TEM-mode nanopore formation in thicker films yields hourglass shaped nanopores.⁹ We did not precisely determine the shape of the nanopores in these thinner films, but we assume the same shape given the similar formation conditions (Fig. 1.1b).

Error in the thickness estimation of the thinned regions across the wafer for RIE thinned pores amounts to as much as ten nanometers. The predominant sources of that error are: a) uniformity of starting window thicknesses across the membrane after the wet etching step in HF to remove the underlying SiO₂ layer (~ 5 nm) and b) uniformity of the RIE etch across the wafer (~ a few nm, depending on size and shape of wafer).

If a membrane was found in the TEM to be slightly thicker than 5 nm (*i.e.* if a pore did not form immediately upon condensing the beam), the film could be thinned further *in situ* by illuminating a small area (a circle with diameter ~ 20 nm) of the thinned membrane for several seconds with the electron beam. The exposed area becomes brighter, indicating an increase in transmitted electrons and therefore a thinner film. When the beam is brought back down to a point, a small pore forms immediately. Thinning too much results in spontaneous pore formation and rapid pore expansion (Fig. 2.2b). In Section 2.5, we will show that this electron-based thinning concept can be quantified and used to controllably thin the membrane with high precision.

For measurements of nanopores in suspended 2D materials, the same RIE procedure was followed, but instead of stopping the etch with a thin SiN_x film remaining, the film was completely etched through. Then the 2D material was deposited on top of the hole.

For measurements of SiN_x nanopores, samples were cleaned in hot piranha to remove any residues and render the surface hydrophilic (the contact angle of a water droplet becomes zero). This procedure is not viable for measurements of 2D materials because it delaminates the 2D layer. A discussion of alternative procedures is found in Section 2.4.

2.3 Homopolymer Discrimination with Thinned Silicon Nitride

In this section, I present the first measurement to combine the capabilities of thin solid state membranes with small pore size. We made membranes down to 5 nm with pores just larger than the diameter of ssDNA (~ 1.1 nm) and demonstrated their sensitivity by using them to discriminate the small chemical differences between short (30 base), single-stranded DNA homopolymers (Fig. 2.3).¹⁰ Short molecules were chosen to avoid known secondary structures. At the same time, the high fields applied to drive DNA through the pore have been reported to linearize the structures of such molecules.¹¹ Guanine was not included in these experiments due to G-tetrad formation in homopolymers longer than four bases.

These pores, of similar physical dimensions as biological pores, show differences in blocked currents from translocating homopolymers of 200-900 pA measured at 1 V (Fig. 2.3b-d), as compared to reports from protein pores of 5-15 pA with limitations on

voltages of 180 mV.¹²⁻¹⁵ These larger differences allow us to measure at higher bandwidths (500 kHz for these experiments) than biological pores (typically measured at 10 kHz), preserving the intrinsic speed of the measurement, rather than needing to slow down the DNA molecule to gain resolution.

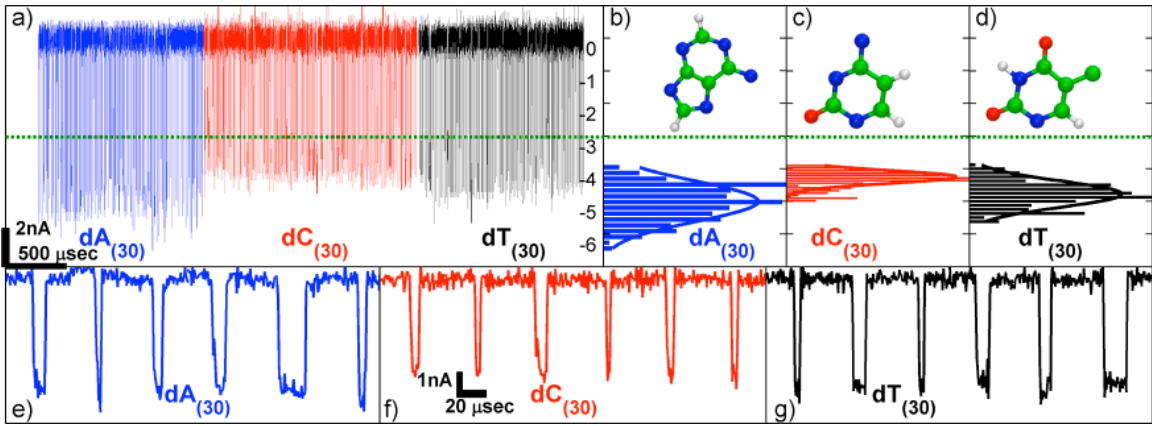


Figure 2.3. a) Translocations of short ssDNA homopolymers through a nanopore of $t = 1.4$ nm and $d = 5$ nm, measured at 1 V with a bandwidth of 500 kHz. The green line shows the threshold for defining events. b-d) Histograms of the event depths. Mean event depths: $\text{poly}(\text{dA})_{30} = 5.1 \pm 0.4$ nA, $\text{poly}(\text{dC})_{30} = 4.2 \pm 0.1$ nA, and $\text{poly}(\text{dT})_{30} = 4.8 \pm 0.2$ nA. e)-g) Zoom-ins of individual events from the data shown in a).¹⁰

The blocked current levels in Fig. 2.3 show qualitative agreement with the physical size of each base, as shown by the atomic structures of adenine, cytosine, and thymine in the inset. The largest blocked current comes from translocations of homopolymers comprised of adenine (a purine and the largest of the three measured here). Homopolymers of the pyrimidines cytosine and thymine (the smaller molecules) block the least ionic current. The standard deviation of blocked current levels, shown by the histograms in Fig. 2.3b-d, is also largest for poly(dA)₃₀ (± 0.4 nA) and smaller for

poly(dC)_{30} (± 0.1 nA) and poly(dT)_{30} (± 0.2 nA). This may be related to the orientation of the bases as the molecule translocates through the pore. If we assume that the distribution of ions in the pore is non-homogeneous (including counter-ions from both the DNA molecule and the charged pore walls), rotations and fluctuations of the larger adenine base may result in a wider range of blocked current values compared to cytosine and thymine.

The ratios of blocked currents between homopolymers (e.g. $\Delta I_A / \Delta I_C$) were the same across three experiments for a range of pore diameters (1-2 nm) and membrane thicknesses (5-8 nm). The ratio of blocked currents for homopolymers of adenine to cytosine was $\Delta I_A / \Delta I_C = 1.25 \pm 0.05$, and the ratio of blocked currents for homopolymers of thymine to cytosine was $\Delta I_T / \Delta I_C = 1.16 \pm 0.02$. If the blocked current during molecule translocation can be approximated by $\Delta I \sim \sigma \times A/h$ — where σ is the electrolyte conductivity, A is the cross-sectional area of the homopolymer, and h is the thickness of the nanopore — then the ratio of blocked current levels between homopolymers can be approximated by the ratio of homopolymer cross-sectional areas and does not depend on membrane thickness (e.g. $\Delta I_T / \Delta I_C = A_T / A_C$). The difference between blocked current levels, however, would be dependent on the membrane thickness (e.g. $\Delta I_T - \Delta I_C \sim (A_T - A_C) / h$). The fact that the different homopolymers were resolved for a range of nanopore diameters and membrane thicknesses implies that some variability in nanopore dimensions may be tolerable for the application of DNA sequencing.

Table 2.1. Comparison of physical dimensions (see Fig. 1.1 for images of the pores) and experimental results between silicon nitride nanopores and prevalent biological nanopores. All measurements were made in 1 M KCl. The measurements of biological pores were taken at room temperature, while the silicon nitride measurements were cooled. Scaling for variations in solution conductivity as a function of measurement temperature was not taken into consideration in this table.^{10,13-19}

	α -hemolysin	MspA	Silicon nitride (SiN _x)
Nanopore diameter (nm)	1.4 ¹⁶	1.2 ¹⁷	1-3
Nanopore thickness (nm)	5 ¹⁶	0.5 ¹⁷	5-8 (or $t_{\text{eff}} = 1.7-2.7$)
Typical operating voltage (mV)	120	180	up to 1000
Open pore conductance, G_0 (nS)	1 ^{13,18}	1.8 ¹⁹	3-14
Blocked current, ΔI (pA)	100 ¹³	150-260 ^{14,15}	1000-5000
Blocked conductance, ΔG (nS)	0.83	0.83-1.4	1-5
Percent of current blocked (%)	83-95 ¹³	48-82 ^{14,15,19}	30-80
Difference in ΔI between nucleotides, ΔI_{bases} (pA)	5-15 ¹³	6-11 ¹⁴	200-900
Difference in ΔG between nucleotides, ΔG_{bases} (nS)	0.042-0.125	0.033-0.061	0.2-0.9

These represent the first measurements of homopolymers using solid state nanopores of the same size as biological pores. The differences in measured values between the solid state pores and measurements of similar molecules in protein pores are shown in Table 2.1. In general, the biological pores can only withstand low voltages (< 200 mV, in contrast with measurements up to 1 V in the solid state measurements presented here), therefore the measured currents are expected to be an order of magnitude smaller. When the current values are scaled for voltage (Table 2.1, Rows 4, 6, and 9),

however, we observe G_0 ($G_0 = I_0 / V$), ΔG ($\Delta G = \Delta I / V$), and variations in conductance between nucleotides (ΔG_{bases}) that are 2–10 times larger than the results from biological pores.

The increase in G_0 could be explained by an underestimate of the nanopore diameter, but that would not explain the concurrent increase in ΔG and ΔG_{bases} , which vary from the biological pore values by approximately the same factor as G_0 . If the nanopore diameter were an underestimate, ΔG would necessarily be smaller, not larger. This suggests that the conductances through solid state nanopores of the same size as biological pores are intrinsically larger, a fact that was perhaps dismissed in earlier literature as a consequence of large nanopore diameter. While a 5 nm SiN_x membrane is still an order of magnitude larger than the thickness of the most narrow constriction point in MspA, the hourglass shape of the SiN_x pore produces a smaller effective thickness (t_{eff}), usually considered to be ~1/3rd of the total film thickness (illustration of the shape in Fig. 1.1). The explanation for the lower currents (*i.e.* higher resistances) in biological pores must be due to either a) a contribution to the channel resistance from the extensions of the biological pores in the direction normal to the bilayer (in α -hemolysin this is referred to as the beta barrel) or b) a difference in the density of water molecules and salt ions inside the pore as compared to those of the solid state nanopore, causing a smaller amount of ion flow through a biological pore of the same geometric dimensions. The predominant conductance models in the literature are purely geometric and may not adequately describe the motions of ions and water molecules inside the nano-scale pore.

Molecular dynamics simulations could offer a more accurate picture of the conductance behavior and shed some light on these experimental findings.

It is also important to note the breadth of the distribution in blocked current for each homopolymer (Fig. 2.2 b-d). At lower bandwidths the ΔI peaks would be more distinct, as long as the short molecule could be fully resolved. However, sequencing at fast speeds is one of the potential advantages of solid state nanopores, and a large degree of overlap between nucleotide blocked current levels makes it difficult to unambiguously distinguish between nucleotides in a random measurement. The standard deviations in the histograms are comparable to the open pore current noise, which is dominated by the capacitance. A reduction of the capacitance by reducing the membrane area exposed to solution, as outlined in a recent publication from our lab,²⁰ would offer a decrease in noise by a factor of ~ 5 in both the open pore current noise and the ΔI noise, reducing the overlap in data from the different nucleotides at these bandwidths. The amount of overlap between different nucleotide distributions can be related to an error rate, whereby the larger the error rate, the more translocations must be measured to unambiguously determine the sequence in a random sample.

2.4 Graphene and Boron Nitride Nanopore Sensors

Given the improvement in signal-to-noise made possible with thin SiN_x membranes, it seemed only a matter of time before even larger signals were measured with nanopores in suspended 2D materials. Our lab was one of the first to fabricate and measure nanopores in suspended graphene,⁶⁻⁸ but from the outset it was clear that small pores were difficult to form in the suspended single atomic layer. It is well documented that electrons accelerated at 200 kV (our usual operating voltage for the TEM) have enough energy to rapidly knock out carbon atoms in suspended graphene.²¹ The practical consequence of this is that even at low beam currents in the TEM, pores frequently nucleate in undesired locations, and when formed, they rapidly expand. The common solution to this problem — how to prevent damage to graphene in the TEM — is to operate the TEM at lower accelerating voltages (typically 80 kV). Most of the results reported from 2D materials to-date, however, show low ΔG values, in large part because the diameters of the nanopores are too large (more on this in Section 2.5).^{6-8,22-25}

Nanopore formation dynamics aside, the even more significant problem proved to be that ionic current through graphene nanopores is plagued by high capacitance and high 1/f noise, limiting the signal-to-noise advantages expected from such a thin membrane.^{7,26} Moreover, at voltages over ~250 mV it is possible to generate electrochemical reactions with the graphene membrane which effectively short the two reservoirs (seen experimentally in my own measurements). Voltages > 250 mV can also cause nanopore expansion and tearing of the suspended film. It is safe to say that what was gained in

terms of thickness reduction came at the expense of operational voltage range, ease and ability to form small nanopores in the TEM, and lower noise.

Boron nitride (BN) (Fig. 2.3) looked like a promising alternative from the perspective that it offers a similar thickness to graphene and, as an electrical insulator, it could potentially generate a lower capacitance. Reducing the suspended area would lower the capacitance even more (Fig. 2.3b).

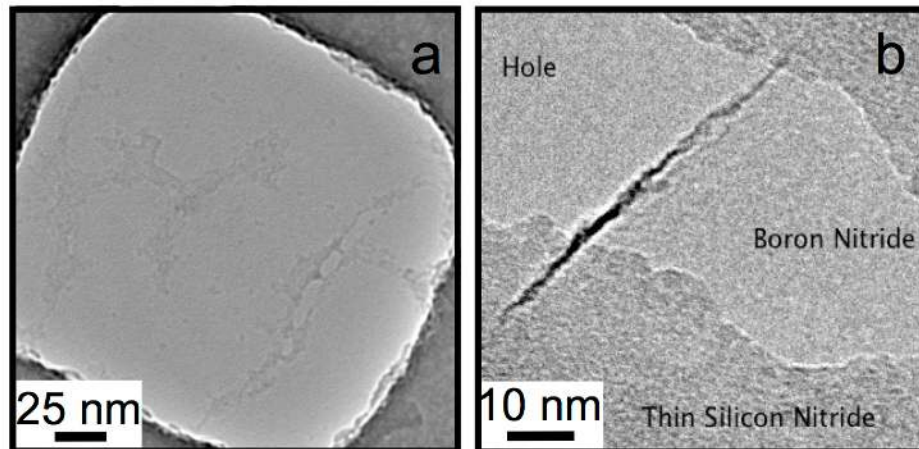


Figure 2.3. a) Square hole in a silicon nitride window over which boron nitride is suspended. Contrast on the boron nitride film is caused by PMMA residues. b) A smaller silicon nitride hole with suspended boron nitride. Exposure to the electron beam caused the left-most side of the BN film to roll up, leaving a hole with no BN.

Graphene, boron nitride, and untreated SiN_x are all hydrophobic though, and the inconsistencies in wetting of those materials proved to be prohibitive, both in terms of generating stable open pore currents and noise. SiN_x is typically made hydrophilic for nanopore experiments by cleaning the membrane in hot piranha solution or with oxygen

plasma. Neither piranha cleaning nor oxygen plasma can be used once the BN layer is deposited because the treatments will delaminate or damage the BN layer. Treatment for hydrophilicity of the SiN_x at the start of the fabrication process does not last through all of the steps necessary to fabricate the device before the ionic current measurement. We attempted several strategies for wetting the pore without use of piranha or O₂ plasma, including: 1) wetting with ethanol and flushing with water and then electrolyte, 2) electrowetting, 3) UV-ozone exposure, and 4) coating the 2D material with an organic molecule with a hydrophilic end-group²⁷ (there are similar attempts in the literature as well^{28,29}), but none of these solutions were able to consistently produce stable open pore currents without compromising the BN layer.

Even if a reliable technique were to be found to obtain stable ionic currents, the low frequency noise may be an intrinsic limitation to nanopores in hydrophobic 2D materials like graphene and BN. The high 1/*f* noise of hydrophobic nano-channels is likely a characteristic trait, caused by atomistic dynamics of the water and ions near the hydrophobic surface.³⁰⁻³⁴ In this instance, again, MD simulations would illuminate the atomic behavior, which might explain experimental results that appear inconsistent when considering geometry alone.

2.5 On the Detection Limit of Ionic Conductance Variations through Silicon-Based Nanopores

Given the success of RIE thinned nanopores and the limitations of nanopores in 2D materials, we returned to SiN_x nanopores to establish the limit of ionic conductance variations for DNA translocations through thinned Si-based nanopores. By using a scanning electrode probe in the TEM to sputter atoms from the SiN_x film (we will refer to this as STEM thinning), we produce an amorphous silicon (*a*-Si) film, which we were able to thin down to < 2 nm — beyond the capabilities of RIE (a comparison of the RIE thinning method to the STEM thinning method is given in Table 2.2) — and do so with greater control and reproducibility, albeit on a smaller production scale. Large-scale molecular dynamics (MD) simulations of thickness limits in these films match our experimental determination of the thickness limit, showing that free-standing *a*-Si membranes become unstable for thicknesses of ~ 1 nm. In this previously unexplored thin-pore regime, we examined dsDNA translocation through nanopores with diameters barely larger than the molecule itself, and the results make a case for Si-based nanopores over the 2D materials.

We also discovered an unexpected blocked current structure in the translocation events, which we attribute to the DNA molecule blocking current flow before entering the nanopore.

Table 2.2. Comparison of RIE thinning and STEM thinning.

RIE thinning	STEM thinning
SF ₆ , CF ₄ , or CHF ₃ + O ₂ ions	electrons
thins from one side of membrane	thins from both sides of membrane
fast (seconds)	slow (tens of minutes)
no <i>in situ</i> monitor of film thickness	EELS shows change in mass, which can be correlated with film thickness
no change in SiN _x composition	nitrogen atoms sputter more quickly leaving <i>a</i> -Si matrix
wafer scale process	single membrane process

2.5.1 STEM Thinning

SiN_x membranes were thinned in the TEM in STEM-mode with the scanning electron beam by rastering the 200 kV electron probe, with a 0.5–2.4 nm diameter, over a defined film area while high-angle annular dark-field (HAADF) STEM images and energy electron-loss spectra (EELS) were acquired continuously and simultaneously, as depicted in Fig. 2.4b. Electron irradiation of the membrane results in sputtering of nitrogen (N) and silicon (Si) atoms,³⁵ and over time (or as a function of electron dose, defined as the total charge deposited per unit area) the film is thinned. The film thickness is monitored and controlled by observing and quantifying this mass loss with the HAADF STEM images and EELS. The sputtering rate of nitrogen is faster than that of silicon,^{36,37} resulting in an amorphous silicon (*a*-Si) membrane for our thinnest films, where all of the nitrogen has been sputtered, leaving only an *a*-Si matrix. Accordingly, we find that thin *a*-

Si membranes are more stable under electron irradiation than silicon nitride membranes of the same thickness. The spatial resolution of this technique is sub-nanometer in scale and is defined by the spatial resolution of the scanning electron probe in STEM (and the electron-sample interaction volume).³⁸

The evolution of the HAADF and EELS signals during STEM thinning of a 50-nm-thick Si₃N₄ film are shown in Fig. 2.4c-d. In this example, a 2.4-nm-diameter electron probe (current density of $4.8 \times 10^9 \text{ A m}^{-2}$) was rastered continuously over a 63 × 63 nm square area (256 × 256 pixels) until all of the atoms in the film were completely sputtered. For film thicknesses less than the scattered electron's mean free path (>100 nm for 200 keV electrons scattered elastically or inelastically in *a*-Si³⁹), the intensity of the HAADF signal (elastic scattering) is proportional to number and mass of atoms in the interaction volume. The EELS signal (inelastic scattering), which is collected simultaneously, can be correlated with the HAADF signal and provides information about the composition of the film. As the film is thinned, the magnitude of the EELS signal at all energies drops, but the N *K*-edge falls faster than the Si *L*-shell ionization edge.^{36,37} These two signals (HAADF and EELS) provide real-time feedback of film thickness and composition as the film is thinned.

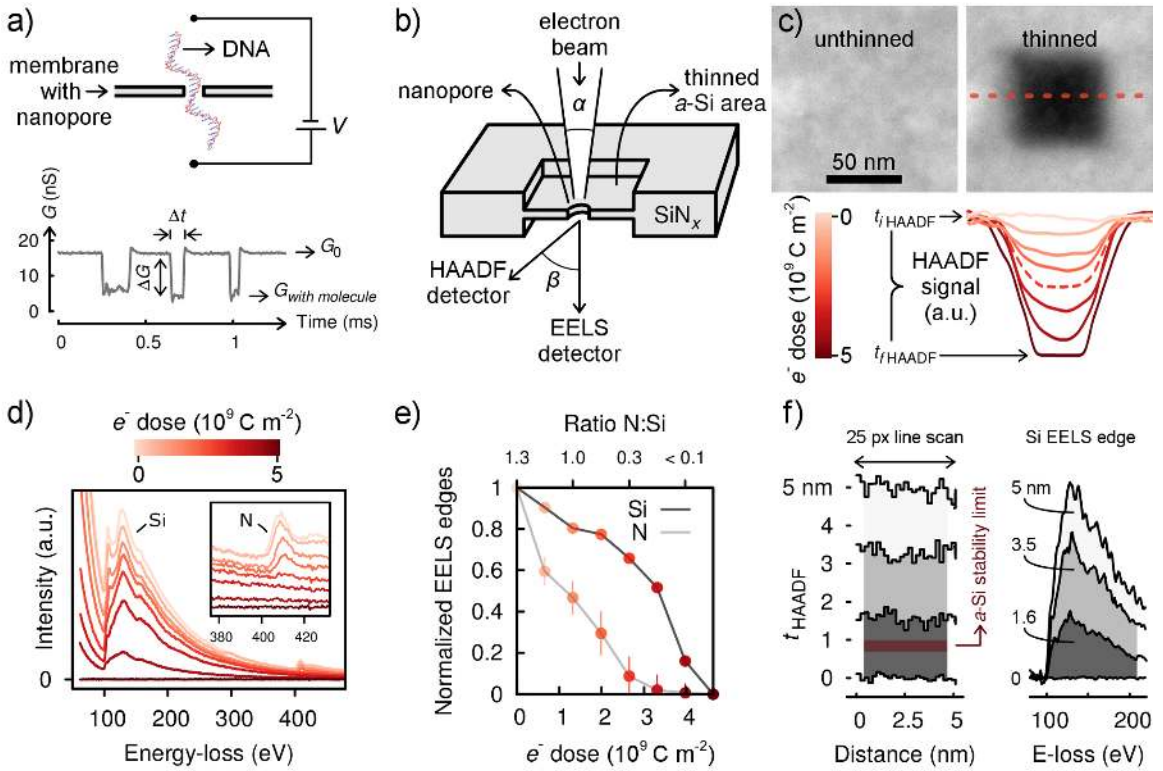


Figure 2.4. Electron-irradiation-based thinning of Si-based films for nanopore sensors. a) Schematic of DNA translocation measurement through a nanopore. b) Diagram of STEM thinning method. c) HAADF STEM images of a Si₃N_x area before (left) and after (right) thinning. Line profiles, indicated by the dashed line, acquired during thinning for increasing electron dose, showing an HAADF signal drop with thinning. HAADF signals corresponding to the initial (50 nm) and final (0 nm) thicknesses are indicated by t_i^{HAADF} and t_f^{HAADF} , respectively. d) EELS signals acquired simultaneous with HAADF signals, where the electron dose correlates with those in (c). The Si *L*-edge maximum shifts from 106 to 101 eV with thinning. The Si *L* and N *K*-edges occur at 100 and 400 eV, respectively. e) Si *L* (dark gray) and N *K*-edge (light gray) EELS signals from (d) normalized by highest magnitude (such that each peak's normalized signal starts at a magnitude of 1) and plotted as a function of electron dose. The top axis indicates the ratio of N to Si atoms. f) HAADF signal (left) and EELS Si *L*-edge (right) measured during the thinning of a 5-nm-thick a -Si membrane to 3.5 and 1.6 nm. The HAADF signal represents a line scan of 25 pixels in the HAADF image, and the EELS signal is an average from 160 pixels. The a -Si thickness limit as determined by MD simulation (0.7–1.0 nm) is indicated by a red band in the HAADF signal.

After an electron dose of $4 \times 10^9 \text{ C m}^{-2}$, the 50-nm-thick Si_3N_4 film, initially with a ratio of N:Si atoms of 1.3, reaches a point where it is predominantly Si and has a ratio of N:Si atoms of < 0.1 (depicted in Fig. 2.4e, where the EELS Si and N ionization edge signals are normalized by the initial highest magnitude and plotted as a function of electron dose). At this point the EELS N K -edge is at the level of the EELS background noise, meaning that this is now an a -Si film. To produce the thinnest membranes, thinning was performed as a two-step process where milder irradiation conditions (for example, 1.6-nm-diameter probe with current density of $0.4 \times 10^9 \text{ A m}^{-2}$) were used in a second, smaller area to reduce the sputtering rate and give finer control over the thinning ($\sim 1 \text{ nm}$ per minute). The noise levels (and thereby the thickness resolution limits) of the HAADF and EELS signals are shown in Fig. 2.4f for an example of one of the thinnest a -Si films (down to $1.6 \text{ nm} \pm 5 \%$ error). The thinnest membrane measured here had a thickness (t) of $1.4 \pm 0.1 \text{ nm}$.

As depicted in Fig. 2.4b, the STEM thinning process thins the membrane from both sides. The AFM image in Fig. 2.5 shows both sides of the STEM thinned film, where thinning was performed in two areas for the same dose, with the only difference being that the substrate was flipped to the other side when performing the second thinning. In this way, we are able to see with the AFM how the film is thinned on each side of the membrane. The image shows the two step thinning process, with the smaller, dark square on the right representing the thinnest region, which was thinned with a second milder dose (shown in TEM images in Fig. 2.7).

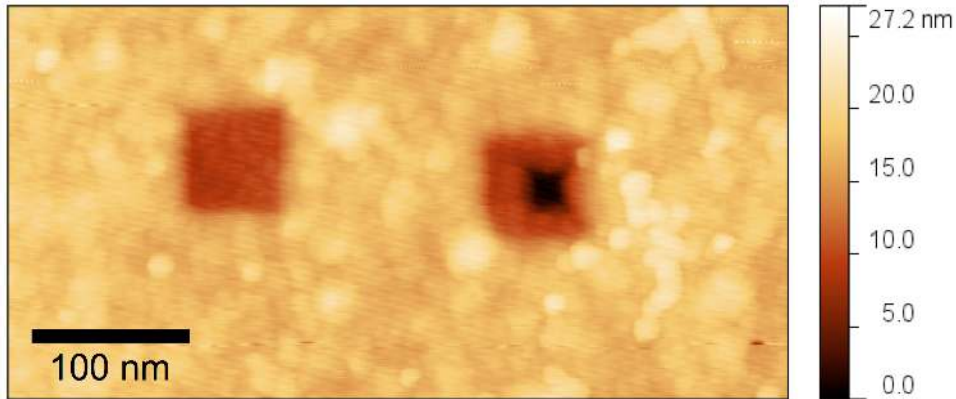


Figure 2.5. AFM image showing both sides of a membrane thinned with a two step STEM thinned procedure. During STEM thinning, thinning occurs on both sides of the membrane. The left square shows the bottom side of the membrane. The right square shows the top side for the same doses in both steps. The small, dark square inside the right thinned region is the second, milder thinning step, but that region is not distinguishable on the opposite side of the membrane.

2.5.2 MD Simulations to Determine the Minimum *a*-Si Membrane Thickness

Our collaborators Adrien Nicolaï and Vincent Meunier at RPI used MD simulations to build model *a*-Si membranes, of thicknesses ranging from 0.5 to 5.0 nm, to establish a theoretical minimum thickness estimate, in comparison to the thinnest membranes we fabricated experimentally (~ 1.4 nm). This theoretical minimum thickness was determined by correlating calculations of the surface energy with the atomic structure, the Si atom coordination, and membrane stability during the MD simulation.

As the film thickness decreases from $t = 5.0$ nm down to 1.5 nm, the calculated surface energy of the film increases linearly (Fig. 2.6a). At thicknesses lower than 1.5 nm,

there is a sharp drop in surface energy (with a minimum for $t = 0.7$ nm) down to the level for a 10-nm-thick film, but then below $t = 0.7$ nm the surface energy again increases rapidly. The atomic models shown in Fig. 2.6b, along with the Si density profile along the direction normal to the film, show that at $t = 0.7$ nm there is a transition to a film with no bulk Si atoms – essentially the film is so thin that all Si atoms are on the surface. This is illustrated by the two density maxima for $t \leq 0.7$ nm (the top and bottom surfaces) and the three maxima for $t > 0.7$ nm (top surface, bulk, bottom surface).

The coordination of the Si atoms can also be used as an indicator of thin α -Si film stability (Fig. 2.6c). A large reduction in Si atom coordination (*i.e.* a reduction in chemical binding) can result in instability of the film. The MD simulations show that the Si atom coordination remains nearly constant and close to bulk levels until $t = 1.0$, when it rapidly drops to under four bonds per Si atom.

The calculations of surface energy, atomic structure, and atomic coordination are all static metrics that point to an α -Si film stability limit in the range of 0.7–1.0 nm. The atomic energy and atomic position fluctuations during MD relaxation provide the last pieces of evidence for the thickness stability limit. This is quantified by the root-mean-square deviation (RMSD) in Si atom position and the variance in atomic energy (Fig. 2.6d). Very similar to the static evidence, there is a large deviation in energetics and structural deformation of α -Si films for $t < 1.0$ nm; while for $t > 1.0$ nm the fluctuations of these parameters during the MD simulations were negligible. These various metrics support the experimental evidence that the thickness limit lies at ~ 1 nm.

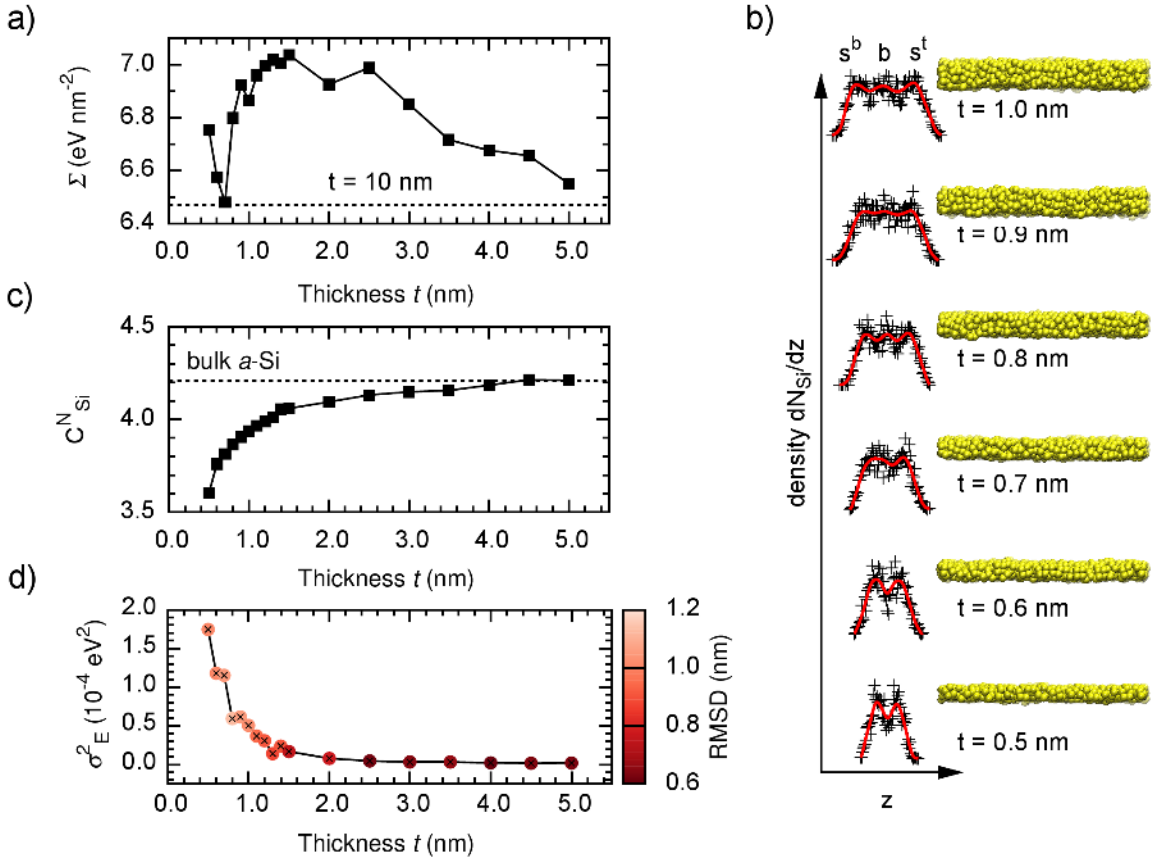


Figure 2.6. Molecular dynamic simulations and stability analysis of a -Si membranes. a) Surface energy Σ as a function of membrane thickness. The dashed line indicates the Σ for a 10 nm thick a -Si film. b) Density of Si atoms (dN_{Si} / dz) along the normal direction (z) perpendicular to the film surface. The bottom surface, top surface, and bulk are labeled as s_b , s_t , and b , respectively. On the right of each density profile is the atomic model for each thickness, where atoms are represented by spheres with van der Waals radius. c) Average number of bonds per Si atom ($C_{N_{Si}}$) as a function of membrane thickness. This is determined by calculating the average number of Si atoms within a 0.15 nm radius of each atom. The dashed line shows the atomic coordination in bulk a -Si. d) Variance (σ^2_E) of the energy per Si atom and Si atom distance root mean square deviation (RMDS) computed during the relaxation of a -Si films as a function of a -Si film thickness.

2.5.3 Nanopore Formation in STEM

Once the film is thinned down to the desired thickness with the scanning electron beam in the TEM, the nanopore can be made by acquiring a STEM HAADF image of the membrane, stopping the scanning motion of the beam, and choosing a pixel where the electron beam will dwell to form the nanopore. The EELS signal is monitored continuously while the beam is fixed, and the drop in the Si peak indicates when the remaining thin film material ($\sim 10^3$ Si atoms) is sputtered in the chosen pixel (Fig. 2.7a). Nanopores were made with electron probe diameters of 1.3–2.4 nm with a current density of 0.3×10^{-9} A m⁻². For membranes with thicknesses < 10 nm, nanopores form within a few seconds under these conditions, with diameters (d) a few angstroms wider than the probe. By calibrating the nanopore size with the electron probe properties (*i.e.* the probe size, convergence angle, and electron dose) we can achieve nanopore size control with sub-nanometer precision (Fig. 2.7b). For thick membranes (for example, 100 nm), these drilling conditions generate a nanopore with a truncated cone shape (Fig. 2.7c). For membranes < 5 nm thick, the nanopore shape is approximated as a cylinder, but at that scale, the shape is defined by only a small number of Si atoms (*e.g.* for a 2.0 nm membrane, < 5 Si atoms span the length of the nanopore). A typical nanopore fabricated this way is modeled in Fig. 2.7d, showing its scale with respect to a dsDNA molecule in solution.

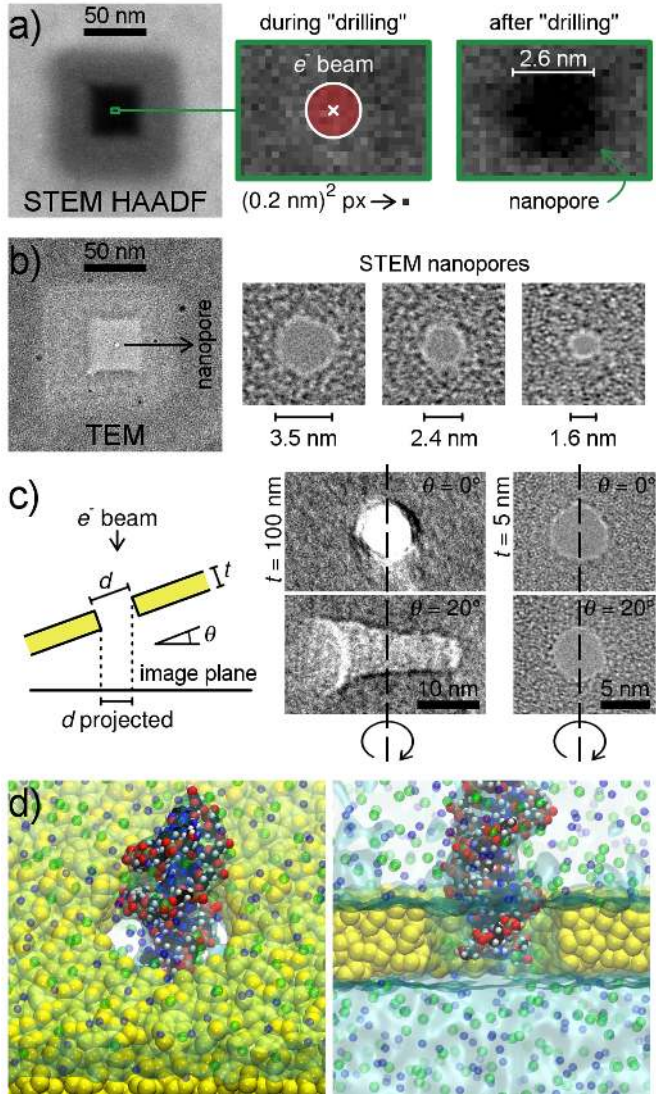


Figure 2.7. Fabrication and characterization of nanopores in thinned *a*-Si membranes. a) STEM HAADF images depicting the nanopore drilling procedure. Here a two-step thinning process was performed with a high current density for more rapid thinning over a large area ($110 \times 110 \text{ nm}^2$) followed by a lower current density for finer control of thinning in a smaller area ($40 \times 40 \text{ nm}^2$). In this example the electron probe size (2.6 nm) is larger than the pixel size ($0.2 \times 0.2 \text{ nm}^2$), and the two right panels show a magnified view of the area before and after nanopore formation. b) Standard TEM images of the resulting *a*-Si thin films with examples of three nanopores (diameters 3.5, 2.4, and 1.6 nm) made in STEM mode with different electron probe conditions. c) Images of nanopores in 100- and 5-nm-thick SiN_x membranes when the TEM sample holder is tilted to 20 degrees. The dashed line indicates the rotation axis. For the 5-nm-thick membrane, the projected nanopore looks the same as the non-tilted image, a further indication of the thickness. d) Images from the molecular dynamics simulations showing a dsDNA molecule translocating through a 2-nm-thick *a*-Si nanopore with 2.7 nm diameter. Legend: Si = yellow, water = depicted as blue ripples, positive ions = blue, negative ions = green.

2.5.4 DNA Translocation Measurements of STEM Thinned Nanopores

To assess the ΔG obtained from nanopores made in thinned *a*-Si membranes we measured translocation dynamics of dsDNA (15 kbp and 400 bp) in buffered 1 M KCl solution as a standard molecule to allow for comparison with published literature. We present data from twelve nanopores in *a*-Si membranes, with 2.5–5.3 nm diameters and thicknesses < 10 nm, of which ten had thicknesses \leq 4 nm, and four had thicknesses < 2 nm. TEM images of three individual nanopores are shown in Fig. 2.8a-c, along with a representative 12 second long raw trace of ionic current measured during DNA translocations, and a zoom-in of individual translocation events at shorter time-scales. The single-point-per-event scatter plots show the distribution of events in translocation duration along with the percentage of current blocked during DNA translocation ($\Delta G/G_0$) and its corresponding histogram. These events show ΔG as high as 10.8 ± 0.4 nS for measured conductivity of 12.0 S m^{-1} , corresponding to a solution concentration of 1.1 M KCl at 23°C (or $\Delta G = 9.7 \pm 0.4$ nS when scaled to 1 M KCl at 23°C). We did not observe a dependence of ΔG on the applied voltage up to 500 mV, which implies that data acquired at different voltages can be directly compared (Fig. 2.8d-e). Other reports in the literature do show a voltage dependence on ΔG – always an increase in ΔG for higher voltages; although there is no consensus as to why that might occur – and in those instances, we consider the highest voltage data available for comparison.

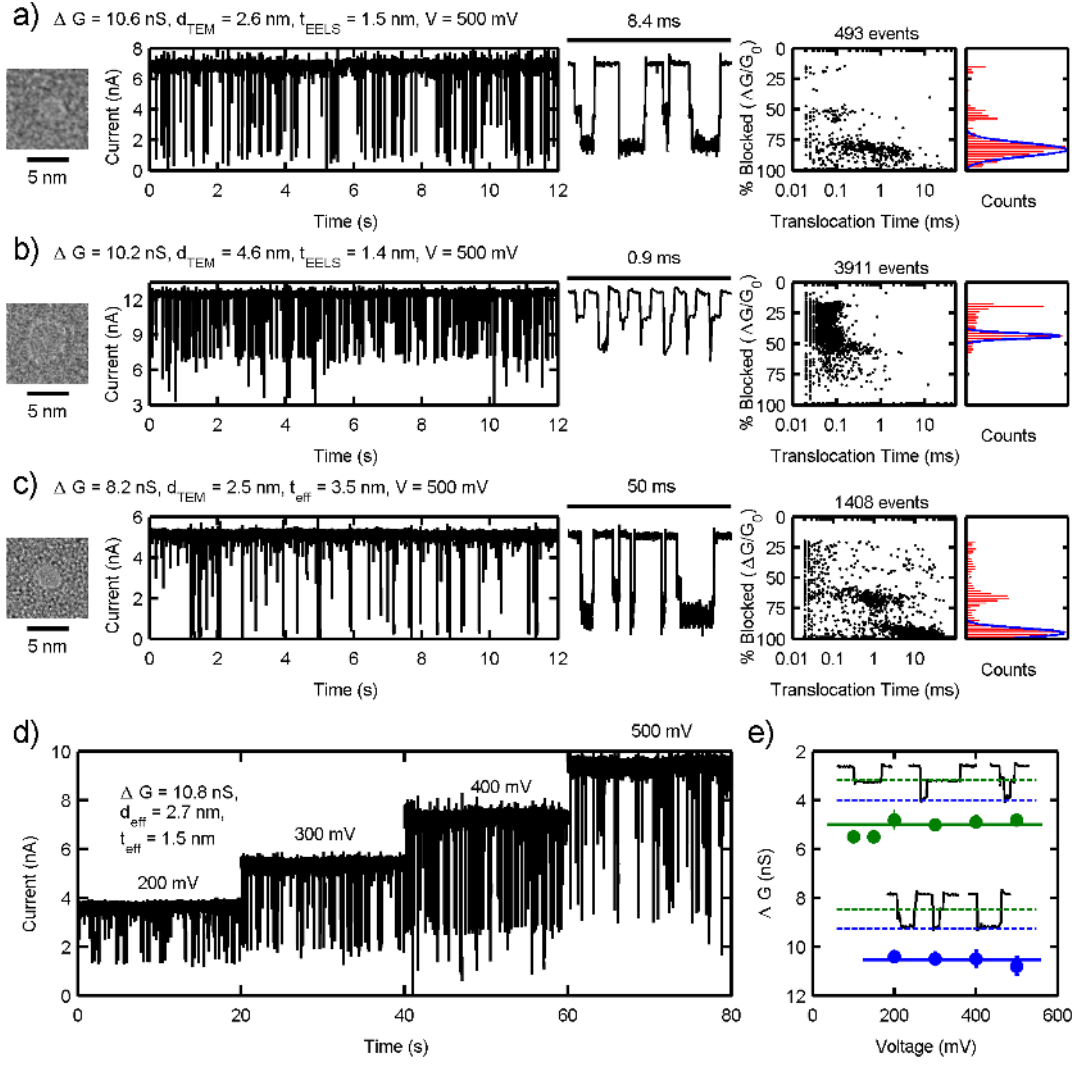


Figure 2.8. Measurements of dsDNA translocations through nanopores in thinned *a*-Si membranes. a-c) Data from three nanopores with dimensions indicated. From left to right: i) TEM images, ii) ionic current time traces showing 15 kbp dsDNA translocations, iii) representative concatenated events shown at shorter time-scales with the same y-axes scale as (ii), iv) single-point-per-event scatter plots showing event distributions in $\Delta G / G_0$ and translocation time, and v) histograms of events for $\Delta G / G_0$ with gaussian fit of the primary translocation peak. TEM images were taken with a low electron dose and resolution to avoid altering nanopore size. All data sets were measured at 500 mV in KCl solution. The solution conductivity and temperature were measured before each experiment. d) Ionic current translocation time traces measured for several voltages from the same nanopore. e) The blue points show ΔG for each voltage shown in (d), and the green points represent the shallow ΔG_s level. Neither the shallow ΔG_s level, nor the full-translocation level exhibit voltage-dependence, emphasized with solid trend lines. Inset shows six representative translocations at 300 mV that demonstrate the structure of the two levels (also seen in a-c). Dashed lines depict where the shallow and full levels lie on the translocations.

As the nanopore diameter is decreased down to the dsDNA diameter, the noise in ionic conductance during translocation (ΔG_{RMS}) becomes larger than G_0 RMS, and the duration of the events increases up to two orders of magnitude (Fig. 2.8a-c). For measurements of dsDNA through nanopores narrower than 2.5 ± 0.2 nm in diameter, nanopore clogging occurs quickly. $\Delta G / G_0$ plateaus at 85 % for dsDNA translocations through nanopores down to 2.5 nm in diameter (Fig. 2.9c).

For all measurements, nanopore diameters were estimated from TEM images (d_{TEM}), and for the thinnest membranes we also calibrated the membrane thickness from EELS (t_{EELS}). When an EELS-based estimate of membrane thickness was not obtained, we used the measured G_0 and ΔG to extract an effective membrane thickness estimate (t_{eff}), as shown in Fig. 2.9a and Appendix A, using a cylindrical model for nanopore conductance.⁴⁰ Nanopore dimensions and DNA translocation results for all measured nanopores are given in Appendix B.

Upon closer inspection of translocation events at short time-scales, it is clear that a significant number of events contain two distinct levels (similar to recent reports^{41,42,43}): a shallow level (ΔG_s) and a deep level (ΔG), indicated by green and blue dashed lines, respectively, in Fig. 2.8e. This type of event structure is unexpected because in pores of this size (down to $d = 2.5$ nm), the DNA molecule cannot translocate in a folded configuration. Typically over 50 % of events contain two levels though, and in some samples it is an even higher percentage.

It may be that this structure is related to the molecule approaching the pore and increasing the access resistance before actually entering the pore, as suggested in a recent

paper with a similar observation.⁴² This seems plausible because R_{pore} (Eq. 1.1), for nanopores of these dimensions (especially $d < 4$ nm and $t < 4$ nm), is no longer the dominant resistance. As much as half of the total resistance in these pores comes from access resistance⁴⁴ ($1/(2\sigma d)$) (Eq. 1.2), so a change in access resistance due to the DNA approach could cause a reduction in current similar to the ΔG_s level. Furthermore, ΔG of the deep level scales with membrane thickness, indicating that that level represents full molecular translocation,² while the magnitude of the shallow level ΔG_s is not dependent on membrane thickness (Fig. 2.9b).

2.5.5 Comparison with literature results

By measuring translocation of dsDNA under standard nanopore measurement conditions, we are able to compare quantitatively between the best ΔG reported in the literature in order to assess the best choice for membrane materials and nanopore dimensions for future nanopore applications. Table 2.3 ranks results from across the literature according to ΔG , for nanopores made in membranes with thicknesses < 10 nm, together with the highest ΔG for dsDNA obtained in this work. Four out of the top six results from Table 2.3, including ours, were measured with Si-based nanopores.

The electrolyte conductivity was not measured in all published studies. In these cases, we assumed standard values, but the error bars for those measurements are accordingly very large. It is important to note that ionic current data is exceptionally sensitive to the electrolyte conductivity. An increase in temperature of 5°C can give a 10

% change in conductivity for the same nanopore diameter and thickness. Similarly, a 0.2 M increase in KCl concentration produces an error in conductivity that can yield an 18 % change in ΔG .

Table 2.3 : Literature results for nanopores with thicknesses < 10 nm, ranked best to worst, according to the scaled ΔG . Only the maximum ΔG is quoted for each reference. The next to last column scales all ΔG to values of 1 M KCl electrolyte at room temperature ($(\Delta G / \sigma_{\text{given}}) \times \sigma_{1 \text{ M KCl}}$). The last column weights ΔG by electrolyte conductivity and DNA diameter (2.2 and 1.1 nm, respectively, for dsDNA and ssDNA). Gray rows correspond to measurements made with ssDNA. The yellow row indicates the highest ΔG obtained in this work.

Reference	Material	t (nm)	d (nm)	DNA	Electrolyte solution	σ (S m^{-1})	V (V)	ΔI (nA)	ΔG (nS)	ΔG scaled to 1 M KCl	ΔG / ($\sigma \times d_{\text{DNA}}$) (dimensionless)
Carlsen <i>et al.</i> ⁴²	SiN _x	4.5	3.4	ds 3 kbp	0.9 M NaCl	7.6 [†]	0.4	3.5	8.7	12.4	0.52
Larkin <i>et al.</i> ⁵	HfO ₂	2 [*]	1.7 [*]	ss 89 b	1 M KCl	9.6	0.4	1.9	4.7	5.3	0.44
Garaj <i>et al.</i> ²²	Graphene	0.6 [*]	2.8	ds 10 kbp	3 M KCl	27.5	0.16	4.1	25.6	10.1	0.42
Wanunu <i>et al.</i> ²	SiN _x	6	4	ds 3 kbp	1 M KCl	13.7	0.3	3.8	12.7	10.0	0.42
This work	a-Si	1.5	2.7	ds 15 kbp	1.1 M KCl	12.0	0.5	5.4	10.8	9.7	0.41
Yanagi <i>et al.</i> ⁴⁵	SiN _x	3.7 [*]	2.3 [*]	ss 5.3 kb	1 M KCl	10.5	0.3	1.4	4.7	4.8	0.40
Merchant <i>et al.</i> ⁷	Graphene/ TiO ₂	6–10	5 × 7	ds 400 bp	1 M KCl	10.8 [†]	0.15	1.1	7.3	7.3	0.31
Liu <i>et al.</i> ²³	BN	1.1	5 × 6	ds 10 kbp	3 M KCl	28.7 [†]	0.16	1.6	10.0	3.8	0.16
Zhou <i>et al.</i> ²⁴	BN	–	4	ds 48 kbp	1 M KCl	10.8 [†]	0.15	0.4	2.8	2.8	0.12
Garaj <i>et al.</i> ⁶	Graphene	0.6 [*]	4.6 [*]	ds 10 kbp	3 M KCl	28.9 [†]	0.16	1.2	7.8	2.9	0.12
Liu <i>et al.</i> ²⁵	MoS ₂	1.6 [*]	20	ds 48 kbp	2 M KCl	20.0	0.2	1.0	5.0	2.7	0.11
Schneider <i>et al.</i> ⁸	Graphene	0.3	22	ds 48 kbp	1 M KCl	10.8 [†]	0.2	0.3	1.5	1.5	0.06

t : thickness. d : nanopore diameter. σ : electrolyte conductivity. V : voltage. ΔV : change in ionic current. ΔG : change in ionic conductance.

^{*} Indicates when values of σ were not quoted in the reference; we assumed values of 7.0, 7.8 and 10.8 S m⁻¹ for 1 M solutions of Li, Na and K chloride at 23°C, respectively.

2.5.6 Data Trends for Small Nanopores in Thin Membranes

The trends in ΔG based on material choice, membrane thickness, and nanopore diameter become even more evident in Fig. 2.9d (errors listed in Appendix B and appear in the graph when the error is larger than the datapoint markers), where ΔG is plotted with respect to the corresponding G_0 for all compiled data from the literature for dsDNA translocations through nanopores < 10 nm thick. Data was scaled to an electrolyte conductivity of 10.8 S m^{-1} , representing 1 M KCl at 23°C . ΔG and G_0 are the directly measured experimental quantities, and this allows a comparison of published results without any fitting for membrane thickness or nanopore diameter, keeping in mind that error bars for published results where electrolyte conductivity was not measured may be large. The upper limit of 100 % conductance blocked ($\Delta G = G_0$) is indicated by a straight dashed line in Fig. 2.9d. To achieve a higher ΔG , one may move up the $\Delta G = G_0$ line by decreasing the membrane thickness for a constant nanopore diameter, which increases both G_0 and ΔG . At the limit of vanishing thickness, the resistance is determined by the access resistance alone for a given nanopore diameter, and any subsequent increase in G_0 can only be achieved by an increase in diameter. When the diameter increases, however, ΔG begins to decrease. Conceptually, this should result in a maximum peak in ΔG as a function of G_0 , and in fact that trend proves to be experimentally true (Fig. 2.9d). To visualize this trend dashed lines of either constant membrane thickness or constant nanopore diameter portray the dependence of ΔG on G_0 , based on the cylindrical model referenced before. Instead of a sharp peak, as predicted by that model, there appears to be a rounded maximum. To achieve the maximum ΔG , both the membrane thickness and

nano pore diameter must be small. Thus, although according to their thicknesses nanopores made in 2D materials should yield the highest ΔG , the majority of reported results for 2D materials fall short of the ΔG values reported for Si-based nanopores either because a) the diameter is too large, b) the film is thicker than expected, or c) the density of water flow through the hydrophobic pore is low when compared to hydrophilic pores.

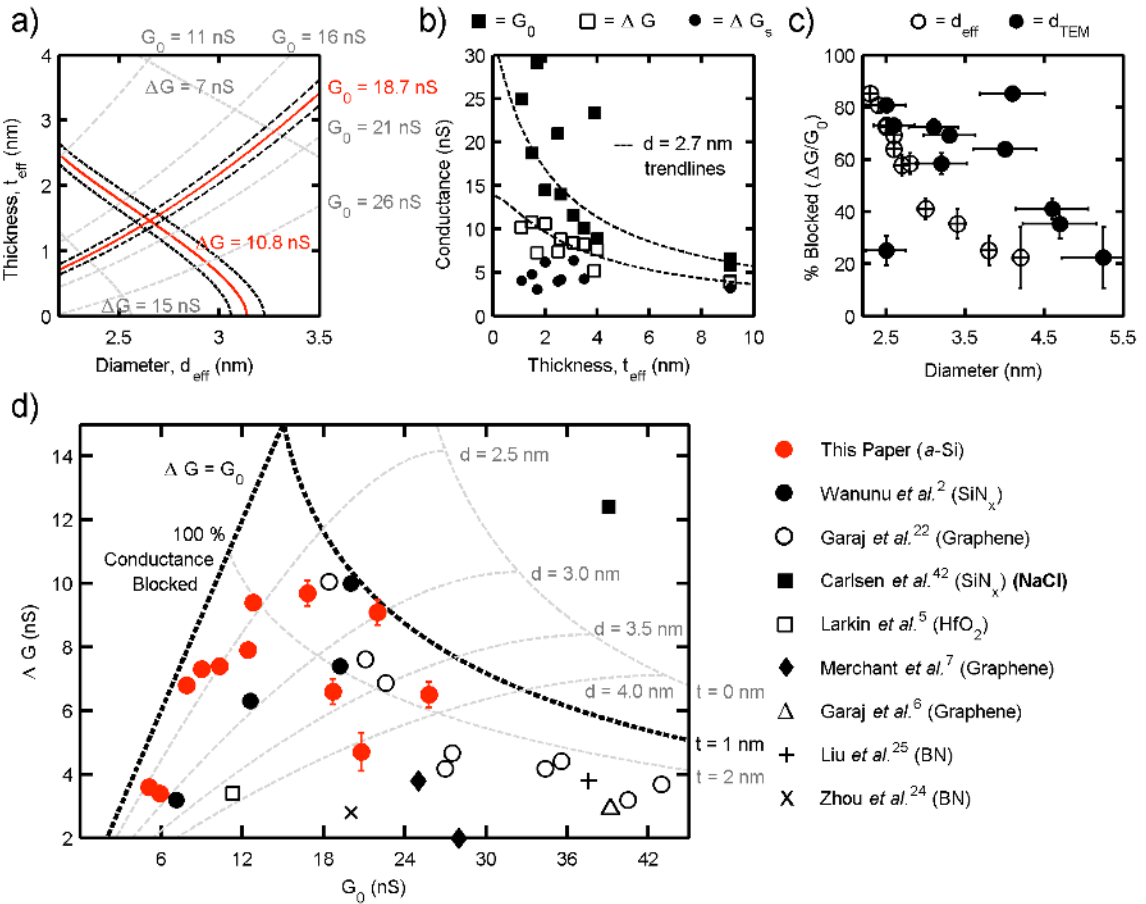


Figure 2.9. Conductance results from *a*-Si nanopores as a function of nanopore diameter and thickness and comparison with sub-10 nm solid-state nanopores in the literature. a) Method of determining d_{eff} and t_{eff} for each nanopore when direct TEM measurements were unavailable. Isolines for the experimentally measured G_0 and ΔG values as a function of nanopore diameter and membrane thickness (red lines with error designated as black dashed lines), according to a cylindrical nanopore model. The intersection of these two isolines gives a solution for d_{eff} and t_{eff} . When effective nanopore dimensions are listed, we have indicated that explicitly. b) G_0 , ΔG , and ΔG_s values plotted as a function of t_{eff} for all measurements for $t_{\text{eff}} < 10 \text{ nm}$. Nanopore diameters range from $d_{\text{TEM}} = 2.5 \text{ nm}$ to 5.3 nm , and the dashed lines are trend lines for $d = 2.7 \text{ nm}$. G_0 and ΔG increase as t decreases, but ΔG_s remains roughly constant. c) $\Delta G / G_0$ plotted as a function of nanopore diameter, where open circles are d_{eff} and filled circles are d_{TEM} . d) Translocation results from our own experiments plotted along with data from the literature for dsDNA (all data is scaled to 1 M KCl, 23°C). All measurements were in KCl electrolyte unless otherwise noted. Points close to the $\Delta G = G_0$ line have nanopore diameters close to the size of the molecule. For larger nanopore diameters, the maximum ΔG is limited by the membrane thickness, with thicker membranes giving smaller ΔG values. Isolines for $t = 0, 1, \text{ and } 2 \text{ nm}$ are shown as guides for the eye. Any data from Table 1 not represented in this graph falls outside the bounds of the graph, with either $\Delta G < 2 \text{nS}$, $G_0 > 45 \text{ nS}$, or both, or was obtained for ssDNA.

2.6 Prospectus on DNA Sequencing with Solid State Nanopores

With the STEM thinning method outlined above, we found that it is possible to consistently fabricate *a*-Si nanopores with thicknesses down to 1.4 nm (close to the limit of thinness as determined by MD) and diameters tailored to molecule size with sub-nanometer precision. DNA translocation measurements with these nanopores provide an estimate of the intrinsic ionic conductance detection limit in Si-based nanopores, which is ~ 10 nS at 1 M KCl at 23°C for dsDNA. The procedures for forming these nanopores are well calibrated and produce a high yield of high ΔG devices.

Despite the advantage in thinness, no 2D material has been able to outperform Si-based nanopores. Even when small nanopore diameters were achieved in 2D materials, the measured ΔG was no better than results from the thinnest Si-based nanopores. Given equal ΔG , Si-based nanopores wet more easily, are robust to higher voltages, and have lower noise than pores in 2D materials.

For the specific application of DNA sequencing, we determined that Si-based nanopores could provide a minimum membrane thickness equivalent to $\sim 4\text{-}5$ nucleotides. This is ~ 3 times thicker than the thinnest constriction of the MspA protein pore, but we have also shown that the differences in signals between nucleotides are larger when measured with slightly thicker solid state nanopores. Even with the MspA pore, the most recent reports consider the signal from combinations of nucleotides residing in the pore at the same time, rather than one nucleotide at a time.¹⁵

At this point we can realistically begin to consider measurements with ~ 1.4 nm thick *a*-Si nanopores, up to ~ 10 MHz bandwidth with custom electronics, with a reduction in noise by a factor of ~ 5 based on a recently reported capacitance reduction technique.²⁰ To become a viable technology for DNA sequencing, it will need to be shown whether ionic current measurements through solid state nanopores can detect unique current levels from all combinations of 4-nucleotide sequences. The next step in that development would be to measure short nucleotide repeats along the same molecule. For long repeated sequences, discrete levels should be discernible. By gradually reducing the number of nucleotide repeats, those discrete levels should begin to blend together as the length of the block approaches the thickness of the nanopore. In this way we can try to pinpoint the precise number of nucleotides contributing to the blocked current signals at once.

2.7 References

1. Li, J. *et al.* Ion-beam sculpting at nanometre length scales. *Nature* **412**, 166–169 (2001).
2. Wanunu, M. *et al.* Rapid electronic detection of probe-specific microRNAs using thin nanopore sensors. *Nature Nanotech* **5**, 807–814 (2010).
3. Yang, J. *et al.* Rapid and precise scanning helium ion microscope milling of solid-state nanopores for biomolecule detection. *Nanotechnology* **22**, 285310 (2011).
4. Sawafta, F., Carlsen, A. & Hall, A. Membrane Thickness Dependence of Nanopore Formation with a Focused Helium Ion Beam. *Sensors* **14**, 8150–8161 (2014).
5. Larkin, J. *et al.* Slow DNA Transport through Nanopores in Hafnium Oxide Membranes. *ACS Nano* **7**, 10121–10128 (2013).
6. Garaj, S. *et al.* Graphene as a subnanometre trans-electrode membrane. *Nature* **467**, 190–193 (2010).
7. Merchant, C. A. *et al.* DNA Translocation through Graphene Nanopores. *Nano Lett.* **10**, 2915–2921 (2010).
8. Schneider, G. F. *et al.* DNA Translocation through Graphene Nanopores. *Nano Lett.* **10**, 3163–3167 (2010).
9. Kim, M. J., Wanunu, M., Bell, D. C. & Meller, A. Rapid Fabrication of Uniformly Sized Nanopores and Nanopore Arrays for Parallel DNA Analysis. *Adv. Mater.* **18**, 3149–3153 (2006).
10. Venta, K. *et al.* Differentiation of Short, Single-Stranded DNA Homopolymers in Solid-State Nanopores. *ACS Nano* **7**, 4629–4636 (2013).
11. Chen, P. *et al.* Probing Single DNA Molecule Transport Using Fabricated Nanopores. *Nano Lett.* **4**, 2293–2298 (2004).

12. Meller, A., Nivon, L., Brandin, E., Golovchenko, J. & Branton, D. Rapid nanopore discrimination between single polynucleotide molecules. *Proc Natl Acad Sci U S A* **97**, 1079–1084 (2000).
13. Deamer, D. W. & Branton, D. Characterization of Nucleic Acids by Nanopore Analysis. *Acc. Chem. Res.* **35**, 817–825 (2002).
14. Derrington, I. M. *et al.* Nanopore DNA sequencing with MspA. *Proc Natl Acad Sci U S A* **107**, 16060–16065 (2010).
15. Manrao, E. A. *et al.* Reading DNA at single-nucleotide resolution with a mutant MspA nanopore and phi29 DNA polymerase. *Nat Biotechnol* **30**, 349–353 (2012).
16. Song, L. *et al.* Structure of staphylococcal α -hemolysin, a heptameric transmembrane pore. *Science* **274**, 1859–1865 (1996).
17. Faller, M., Niederweis, M. & Schulz, G. E. The structure of a mycobacterial outer-membrane channel. *Science* **303**, 1189–1192 (2004).
18. Kasianowicz, J., Brandin, E., Branton, D. & Deamer, D. Characterization of individual polynucleotide molecules using a membrane channel. *Proceedings of the National Academy of Sciences* **93**, 13770–13773 (1996).
19. Butler, T. Z., Pavlenok, M., Derrington, I. M., Niederweis, M. & Gundlach, J. H. Single-molecule DNA detection with an engineered MspA protein nanopore. *Proc Natl Acad Sci U S A* **105**, 20647–20652 (2008).
20. Balan, A. *et al.* Improving Signal-to-Noise Performance for DNA Translocation in Solid-State Nanopores at MHz Bandwidths. *Nano Lett.* **14**, 7215–7220 (2014).
21. Krasheninnikov, A. V. & Nordlund, K. Ion and electron irradiation-induced effects in nanostructured materials. *J. Appl. Phys.* **107**, 071301–071301 (2010).
22. Garaj, S., Liu, S., Golovchenko, J. A. & Branton, D. Molecule-hugging graphene nanopores. *Proceedings of the National Academy of Sciences* **110**, 12192–12196 (2013).
23. Liu, S. *et al.* Boron Nitride Nanopores: Highly Sensitive DNA Single-Molecule Detectors. *Adv. Mater.* **25**, 4549–4554 (2013).
24. Zhou, Z. *et al.* DNA Translocation through Hydrophilic Nanopore in Hexagonal Boron Nitride. *Sci Rep* **3**, – (2013).

25. Liu, K., Feng, J., Kis, A. & Radenovic, A. Atomically thin molybdenum disulfide nanopores with high sensitivity for DNA translocation. *ACS Nano* **8**, 2504–2511 (2014).
26. Heerema, S. J. *et al.* 1/f noise in graphene nanopores. *Nanotechnology* **26**, 1–7 (2015).
27. Kamps, A. C., Fryd, M. & Park, S.-J. Hierarchical self-assembly of amphiphilic semiconducting polymers into isolated, bundled, and branched nanofibers. *ACS Nano* **6**, 2844–2852 (2012).
28. Tang, Z. *et al.* Surface Modification of Solid-State Nanopores for Sticky-Free Translocation of Single-Stranded DNA. *Small* **10**, 4332–4339 (2014).
29. Schneider, G. F. *et al.* Tailoring the hydrophobicity of graphene for its use as nanopores for DNA translocation. *Nature Communications* **4**, 2619–2619 (2013).
30. Beamish, E., Kwok, H., Tabard-Cossa, V. & Godin, M. Precise control of the size and noise of solid-state nanopores using high electric fields. *Nanotechnology* **23**, 405301 (2012).
31. Smeets, R. M. M., Keyser, U. F. U., Wu, M. Y. M., Dekker, N. H. N. & Dekker, C. C. Nanobubbles in solid-state nanopores. *Phys. Rev. Lett.* **97**, 088101–088101 (2006).
32. Smeets, R. M. M., Keyser, U. F., Dekker, N. H. & Dekker, C. Noise in solid-state nanopores. *Proceedings of the National Academy of Sciences* **105**, 417–421 (2008).
33. Smeets, R. M. M., Dekker, N. H. & Dekker, C. Low-frequency noise in solid-state nanopores. *Nanotechnology* **20**, 095501 (2009).
34. Powell, M. R., Cleary, L., Davenport, M., Shea, K. J. & Siwy, Z. S. Electric-field-induced wetting and dewetting in single hydrophobic nanopores. *Nature Nanotech* **6**, 798–802 (2011).
35. Egerton, R. F., Li, P. & Malac, M. Radiation damage in the TEM and SEM. *Micron* **35**, 399–409 (2004).

36. Wu, M.-Y., Krapf, D., Zandbergen, M., Zandbergen, H. & Batson, P. E. Formation of nanopores in a SiN/SiO₂ membrane with an electron beam. *Appl. Phys. Lett.* **87**, 113106–113106–3 (2005).
37. Howitt, D. G., Chen, S. J., Gierhart, B. C., Smith, R. L. & Collins, S. D. The electron beam hole drilling of silicon nitride thin films. *J. Appl. Phys.* **103**, 024310 (2008).
38. Puster, M., Rodríguez-Manzo, J. A., Balan, A. & Drndic, M. Toward Sensitive Graphene Nanoribbon–Nanopore Devices by Preventing Electron Beam-Induced Damage. *ACS Nano* **7**, 11283–11289 (2013).
39. Egerton, R. F. *Electron Energy-Loss Spectroscopy in the Electron Microscope*. (Plenum Press, 1996).
40. Kowalczyk, S. W., Grosberg, A. Y., Rabin, Y. & Dekker, C. Modeling the conductance and DNA blockade of solid-state nanopores. *Nanotechnology* **22**, 315101 (2011).
41. Rosenstein, J. K., Wanunu, M., Merchant, C. A., Drndic, M. & Shepard, K. L. Integrated nanopore sensing platform with sub-microsecond temporal resolution. *Nat Meth* **9**, 487–492 (2012).
42. Carlsen, A. T., Zahid, O. K., Ruzicka, J., Taylor, E. W. & Hall, A. R. Interpreting the conductance blockades of DNA translocations through solid-state nanopores. *ACS Nano* **8**, 4754–4760 (2014).
43. Briggs, K., Kwok, H. & Tabard-Cossa, V. Automated fabrication of 2-nm solid-state nanopores for nucleic acid analysis. *Small* **10**, 2077–2086 (2014).
44. Hall, J. E. Access resistance of a small circular pore. *The Journal of general physiology* (1975).
45. Yanagi, I., Akahori, R., Hatano, T. & Takeda, K.-I. Fabricating nanopores with diameters of sub-1 nm to 3 nm using multilevel pulse-voltage injection. *Sci Rep* **4**, 5000 (2014).

Chapter 3

Positioning a Charge Sensor near the Nanopore

3.1 Introduction

As described in the previous chapters, there has been encouraging progress toward single-molecule DNA sequencing using both biological and solid state nanopores. At this point, there are mainly two divergent approaches toward improving the signal-to-noise of nanopore measurements: 1) slow down the speed of DNA translocation so that the ionic current measurement can be made at lower bandwidths with less high frequency noise¹⁻³ (the high capacitance of the lipid bilayer necessitates this approach for biological pores) or 2) reduce the noise of the amplifier and nanopore in order to measure at high bandwidths and preserve the intrinsic speed of the DNA translocation.^{4,5}

Incorporating electronic detection with a graphene charge sensor at the nanopore may be an alternative technique for nucleotide detection with even higher bandwidths than ionic current measurements and a spatial resolution that in principle could be as fine

as the graphene thickness (at ~ 0.3 nm it is approximately the same as the separation between nucleotides along the DNA backbone). With this technique, the nanopore localizes the DNA molecule near the sensor, ensuring that the bases flow past the sensor linearly while both the ionic current signal and the current through the graphene device are measured simultaneously. As nucleotides pass one-by-one through the nanopore and past the sensor, only one base abuts the graphene nanoribbon (GNR) at a time.

Graphene device geometry can be tailored *via* electron-beam lithography to form nanoribbons^{6,7} and nanoconstrictions^{8,9} to maximize the portion of the sensor perturbed by the molecule. Even finer device architectures can be formed by transmission electron beam ablation lithography (TEBAL),¹⁰ which work from our lab has shown can produce graphene structures down to a few nanometers in width¹¹ that are able to sustain the micro ampere currents needed to achieve sufficient signal-to-noise for high bandwidth detection.¹²

In this chapter, I outline methods to form a nanopore next to a graphene nanoribbon (Fig. 3.1) and discuss DNA translocation measurements of those devices in electrolyte solution. The graphene nanoribbon devices (typically of widths down to 50 nm and lengths of 600 nm, on SiN_x membranes) can sustain micro ampere currents at low voltages (~ 50 mV) in electrolyte solution and exhibit a sensitivity to uniform changes in potential of $\sim 1\% / \text{mV}$, in 1 M KCl solution.

The act of drilling a nanopore next to or inside the device, however, can cause damage to the sensor, significantly altering its response to changes in potential. GNR conductance measurements, conducted *in situ* inside a TEM operating at 200 kV, show

that during nanopore formation and imaging, GNR resistance increases linearly with electron dose and that GNR sensitivity decreases by a factor of ten or more upon exposure at high magnification. We present a methodology for forming a nanopore at the edge or in the center of the nanoribbon in scanning TEM (STEM) mode, in which the position of the converged electron beam can be controlled with high spatial precision, that minimizes the exposure of the GNRs to the beam before and during nanopore formation and preserves the high conductivity and sensitivity of the GNR-nanopore sensors.

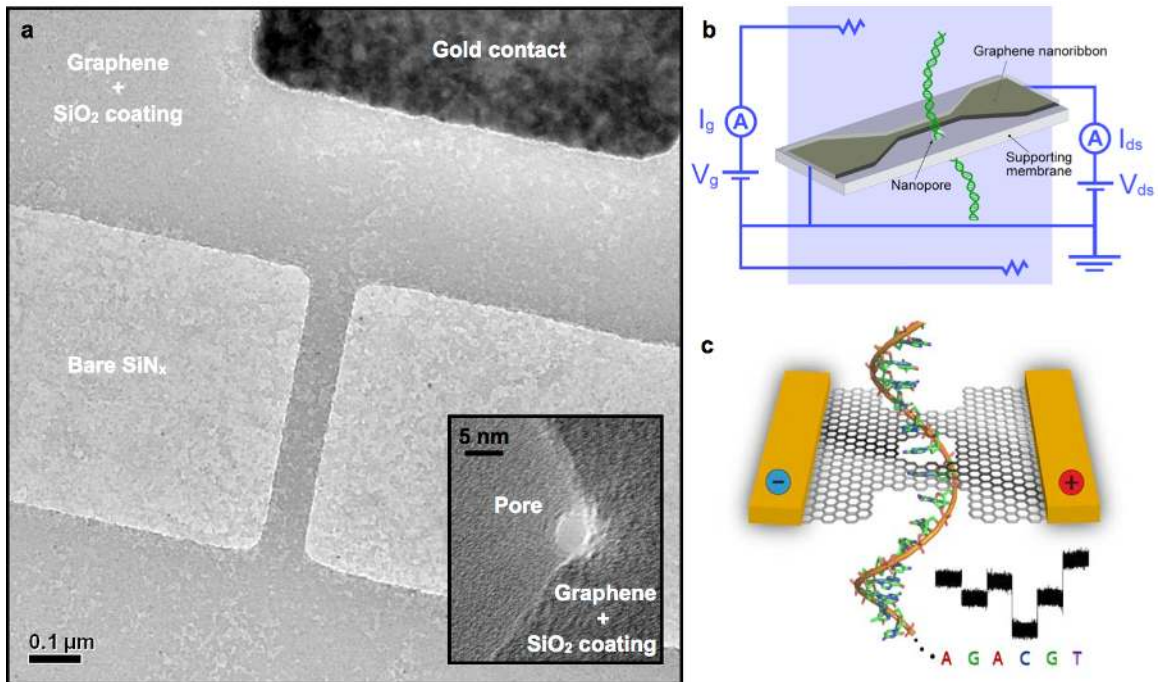


Figure 3.1. a) Graphene nanoribbon between gold contacts. (Note: this nanoribbon was fabricated via standard e-beam lithography. This is not the resolution limit for this resist. Lines can be thinned even further with the focused beam in the TEM.) Inset: Pore carved into the side of the ribbon. b) Measurement schematic. c) Cartoon illustrating DNA sequencing with a graphene nanoribbon. (Image courtesy of Bob Johnson)

3.2 Fabrication

3.2.1 Design Criteria and Challenges

The following design criteria were used as guidelines while designing and modifying the GNR devices:

1) *Visibility in the TEM:*

The nanopore must be positioned with nanometer precision in relation to the nanoribbon. Therefore, the ribbon must either be visible in the TEM, or there must be a protocol using markers for alignment that can provide the necessary precision (this is actually quite difficult).

2) *Wetting the pore:*

Immediately before an ionic current measurement, the nanopore must be cleaned, and the surface of the SiN_x and pore need to be made hydrophilic (they will naturally be somewhat hydrophobic). The conventional method of piranha cleaning (a heated mixture of sulfuric acid and hydrogen peroxide) to oxidize the SiN_x surface and make it hydrophilic will destroy the graphene device. Instead, an O_2 plasma clean can be used to make the pore hydrophilic, but because O_2 plasma will etch any exposed graphene, the ribbon must be covered with an etch mask. Or an alternative procedure must be developed to wet the pore.

3) *Minimize electrochemistry relative to ribbon current:*

When a potential is applied to the device, significant leakage currents can appear between the electrically connected device and the Ag/AgCl electrodes in solution which drive the ionic current through the nanopore. The leakage occurs either through the dielectrics sandwiching the graphene, from the exposed graphene edges, or from the gold contacts. At sufficient magnitude, these leakage currents can impact the potential field profiles that drive DNA through the pore. Electrochemistry can also limit the device lifetime. To reduce the influence of leakage currents, it is possible to grow an insulating, conformal atomic-layer deposition (ALD) oxide layer over the surface of the device. For applications involving large areas of graphene and/or gold, the insulation layer becomes important because leakage currents are high.

The goal is for the ionic current through the nanopore and the current through the ribbon to behave as two independent circuits. For nanoribbon devices with low resistance, the drain-source current through the graphene is high enough that 10-100 nA of constant leakage current is not detrimental to device performance because it is still one to two orders of magnitude lower than the current through the ribbon (μ As). Leakage currents can typically be ignored for low voltages (up to 250 mV), while for higher voltages (greater than 600 mV), leakage currents can reach 1 μ A. It is preferable to avoid using an ALD layer because the addition of an ALD layer makes the membrane thicker, lowers the signal-to-noise of the ionic current, and introduces the dynamics of a second material into the pore drilling process.

3.2.2 Standard Graphene Nanoribbon Design

Graphene nanoribbons were made using graphene grown via chemical vapor deposition (CVD). The graphene was grown on copper to be a continuous single layer with few multi-layer regions. C4-495 PMMA was spun onto the top of the graphene/copper foil, and any carbon on the back-side of the foil was etched with O₂ plasma. The copper was then etched away by floating the foil on an FeCl₄ solution overnight, transferred by means of a PET slide onto water, and then transferred again onto 4 M HCl and allowed to sit overnight to remove any residual iron particles.¹³

The contact pads were fabricated in a two step process. First, large Au contacts were defined *via* photolithography with NR-7 resist so that they aligned on the Si wafer with the suspended SiN_x membranes. Au was deposited by thermal evaporation with a 3 nm Ti adhesion layer. The second electrode layer of smaller contacts was defined by electron-beam lithography after the graphene was transferred onto the device. In this way the graphene is never exposed to the contaminants associated with photoresist.

After the large contacts but before the small contacts layer, the graphene was transferred onto a series of water baths and finally deposited onto a piece of wafer with large contact pads, where it was allowed to air dry. Once visibly dry, the piece of wafer was heated at 100°C for 1 min to promote adhesion of the graphene. Then the wafer with graphene was dipped into water to dissolve any salts that may have found their way onto the top side of the graphene/PMMA film. The PMMA on top of the graphene was then re-

dissolved with several drops of fresh PMMA resist, allowed to dry, and set in acetone overnight to remove the PMMA. Once the PMMA was removed in acetone and rinsed in IPA and water, residues were removed and adhesion of the graphene promoted by heating the sample at 350°C for 45 minutes in a rapid thermal annealer (RTA) in a continuous flow of 5% H₂ / 95% Ar.

Raman was used to characterize each graphene growth, and the electron diffraction pattern and film height (with AFM) were acquired for some samples. In a few instances single-crystal graphene hexagons were used for devices (Fig. 3.2).

The second layer of gold contacts (the small contacts that interface with the ribbon) was then defined by electron-beam lithography in C4-495 PMMA on top of the graphene sheet. Again, Au was thermally deposited with a 3 nm Ti adhesion layer, and after liftoff in acetone and rinsing in IPA and water, the graphene sheet was again cleaned with the same RTA procedure.

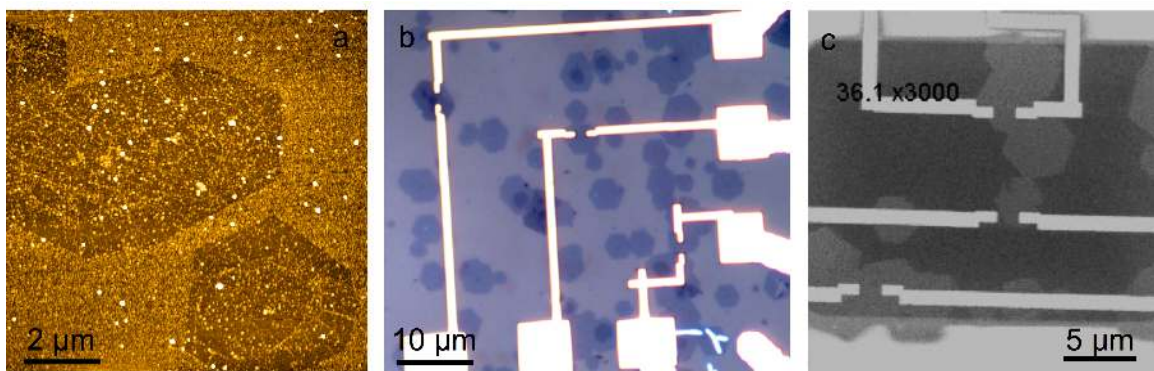


Figure 3.2. Images of graphene hexagons used for some devices. a) AFM image on SiN_x. b) Optical image on 90 nm SiO₂. Gold contacts lead to individual hexagons. c) SEM image on SiN_x window.

The nanoribbon was defined by electron-beam lithography in HSQ resist (Dow Corning, XR-1541, 2% solution in MIBK, spun at 4000 rpm for 60 s) and developed for 1 min in a home-made salty basic developer of 1% NaOH / 3% NaCl and rinsed in water.^{14,15} The dimensions of the ribbons were typically 600 nm long and 50–200 nm wide. Line-widths as thin as ~ 20 nm in width were achieved in HSQ dose tests. During developing, the exposed sections of the HSQ resist harden into an SiO₂ layer. Large HSQ pads were defined around the gold contacts leading to the ribbon (Fig. 3.3), and these large pads proved to be crucial for higher device yield. The large HSQ pads both ensure large contact area between graphene and gold and prevent enhanced under-etching of graphene near the gold during the O₂ plasma step.

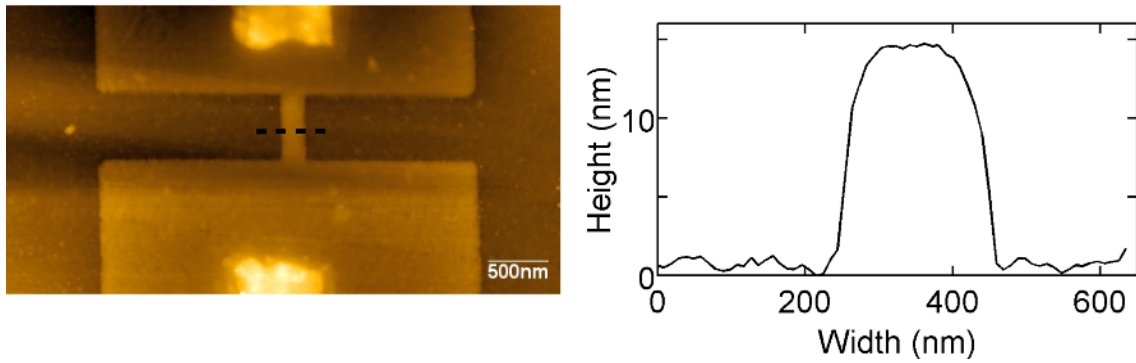


Figure 3.3. AFM image of a ~ 200 nm wide graphene nanoribbon (left) and the corresponding height profile along a black dashed line (right). The HSQ etch mask on top of the GNR has a thickness of ~ 15 nm.¹⁶

The developed HSQ served as an etch mask to define the pattern in the graphene sheet. A 50 W O₂ plasma etch was used to remove graphene from un-patterned areas.

Typically 10–20 s was a sufficient etch time (yielding no conduction between non-connected contact pads), but for the sake of cleaning the surface for subsequent nanopore experiments, longer etch times were frequently used. Some ribbon resistances would remain un-changed for etch times of minutes, while others would die. Yield of working ribbons was typically 33% despite: a) the apparent homogeneity in the graphene film as observed in the SEM and with raman and b) comparable sheet resistances before etching (100s of Ohms for 1-2 μm contact separation). Typical ribbon resistances were 10–40 k Ω . There was no correlation between ribbon width and resistance; however yield of 50 nm ribbons was slightly lower than thicker ribbons but still varied batch-to-batch.

3.2.3 Alternative Graphene Nanoribbon Designs

For the purpose of moving the operating range of the graphene ribbon to a more sensitive position on the gate-response curve (R_{ds} vs V_g , to be described in Section 3.3), some devices were also made with side gates. These devices were never used for nanopore experiments.

To improve sensitivity, the HSQ layer was removed on several devices in HF, and although the devices still functioned perfectly well, the bare graphene was impossible to see on SiN_x in the TEM. Markers were made for alignment in the TEM by lithographically defining a pattern near the edges of the ribbon and either evaporating gold or etching the SiN_x membrane in those defined areas.

Instead of markers, though, it proved to be faster, easier, and more precise to define a rectangle in the center of the ribbon with electron-beam lithography in PMMA resist, where the HSQ was removed with HF to expose the graphene in only that area. In this way, most of the ribbon could still be seen in the TEM, making it easy to find the bare graphene area where the nanopore was formed. Unfortunately wetting the pore in these devices proved to be the prohibitive step. Once the HSQ was removed, O₂ plasma could not be used to make the pore hydrophilic before the ionic current measurement, and no other method was found for consistently wetting the pore. The techniques attempted were the same as those described for measurements of nanopores in 2D materials (Section 2.4).

3.3 Mechanism of Detection

At the same time as the development of these experimental procedures, GNR-nanopore sensors were being investigated in theory and simulation work. The general idea of these calculations was to meld quantum transport simulations of the graphene ribbons with unique electrostatic perturbations generated by the different nucleotide atomic structures as they translocated through a nanopore formed inside the graphene ribbon.¹⁷⁻²¹ The nucleotide-specific perturbations were found to modulate the charge density and transmission coefficient of the graphene ribbon, even when considering a diversity of nucleotide orientations inside the pore, resulting in nucleotide-specific

conductance variations. Most of the calculations assume no interaction between substrate and graphene, consider a graphene ribbon < 10 nm in width, require an assumption of precise edge structure on the sides of the ribbon as well as at the nanopore formed inside the ribbon, and do not consider effects of the electrolyte, screening, or sources of noise. Their predictions also predict current variations at least an order of magnitude larger than what is possible given the maximum changes in R_{ds} vs. V_g in our devices.

Successful experimental detection of DNA translocating through a nanopore with a 50 nm diameter silicon nanowire was reported in 2011 by Xie, *et al.*,²² and they propose a somewhat different mechanism to explain their results. Instead of the charge of the DNA or electronegativity of the atoms in the nucleotide directly gating the device, they attribute changes in conductance of their device to a perturbation of the electric potential field in the electrolyte solution that is a result of the translocation of the entire molecule. As discussed in Chapter 2, when the DNA molecule is moving through the nanopore, the pore becomes effectively smaller, and the resistance to ion flow increases (hence the drop in ionic current). That change in resistance, along with the change in access resistance commensurate with a change in effective pore size, causes a change in the spherically symmetric potential gradient falling away from the pore through the electrolyte (Fig. 3.5a). It was hypothesized that this change in potential caused the conductance modulations in the Si nanowire device. This is effectively an amplification of the ionic signal because the change in the ionic current (ΔI_{pore}) is proportional to a change in the potential gradient in solution, which is in turn proportional to the observed change in

ribbon current (ΔI_{ribbon}). Any signal in the ionic channel is seen in the nanowire device with an amplification related to the transconductance of the device.

It is possible that both effects — shown experimentally and predicted theoretically — may be present to different degrees. When the molecule enters the pore, there would be a conductance modulation in the ribbon equivalent to the observation of Xie, *et al.* Within that signal, however, there may be finer fluctuations in the ribbon conductance due to the electrostatic variations generated by the passing nucleotides.

The sensitivity of our graphene nanoribbon devices to changes in electric potential can be characterized by measuring the response to a gate voltage in electrolyte solution. The devices were immersed in KCl solution (from 1 M to 1 mM), and a gate voltage (V_g) was applied to a Ag/AgCl electrode in the solution above the device while the resistance (R_{ds}) of the GNR was measured (schematic shown in Fig. 3.4a). The GNR sensors are most sensitive to external potentials at gate voltages where the R_{ds} vs. V_g curve is the steepest. The GNR resistance exhibits a maximum in this example at $V_g \sim 140$ mV, which indicates that the graphene is p-doped, most likely due to doping from residues left from processing.²³⁻²⁵ From the representative gating curve at 1 M KCl shown in Fig. 3.4b, a perturbation of the potential uniformly across the ribbon of ~ 10 mV at the most sensitive region of the transconductance curve should generate ~ 60 nA change in GNR current from a baseline current of 1.5 μ A, a variation significantly higher than the GNR noise level of $I_{\text{rms}} \sim 12$ nA at 1 MHz bandwidth in solution.

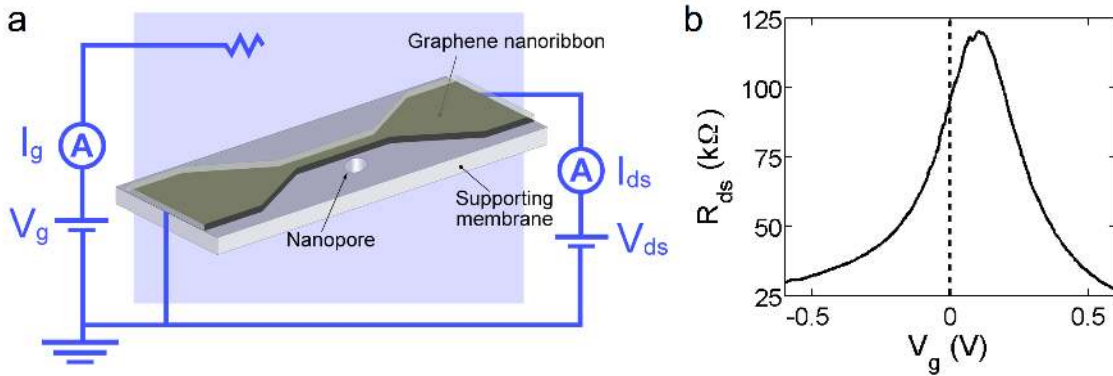


Figure 3.4. a) Schematic showing the GNR device and the circuit diagram used for electrolytic gating in KCl solution. b) GNR resistance (R_{ds}) vs. gate voltage (V_g) in 1 M KCl.¹⁶

Of course a change in potential would not be felt uniformly across the ribbon, as that calculation assumes. Models of the potential field as a function of radial distance from the pore show that the largest change in potential occurs near the pore, falling rapidly with radial distance away from the pore (Fig. 3.5).^{22,26}

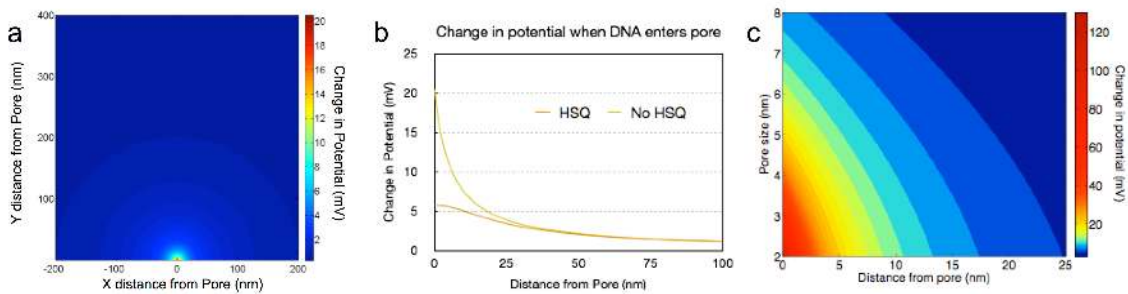


Figure 3.5. Plots of the potential field about the pore following the analytical analysis outlined by Xie, *et al.*²² a) Plot of the change in potential induced by DNA translocation. The potential falls off from the nanopore at the origin. b) The change in potential calculated above the HSQ, as compared to the change in potential across the ribbon with no HSQ. c) The trend of change in potential shown as a function of distance from the pore as well as nanopore size.¹⁶ The larger change in nanopore resistance upon translocation through a small pore induces larger changes in potential.

3.4 Nanopore Formation in STEM to Reduce Electron Damage

3.4.1 Damage to Graphene Ribbons in the TEM

Over the course of fabricating hundreds of devices and drilling nanopores in the TEM, we discovered that the process of forming the nanopore in the TEM caused significant damage to the graphene device. To precisely locate the position for nanopore drilling relative to the graphene nanoribbon, it was necessary to image some part of the device at relatively high magnification and thus high current densities. The 200 keV electron beam energy is high enough to damage graphene,^{27,28} so the exposure of the nanoribbon to the beam while determining the position for the pore before condensing the beam to drill the pore rendered portions of the device non-conductive. Fig. 3.6 shows resistance changes for ribbons of different widths with pores drilled either on the edge or in the middle of the ribbon.

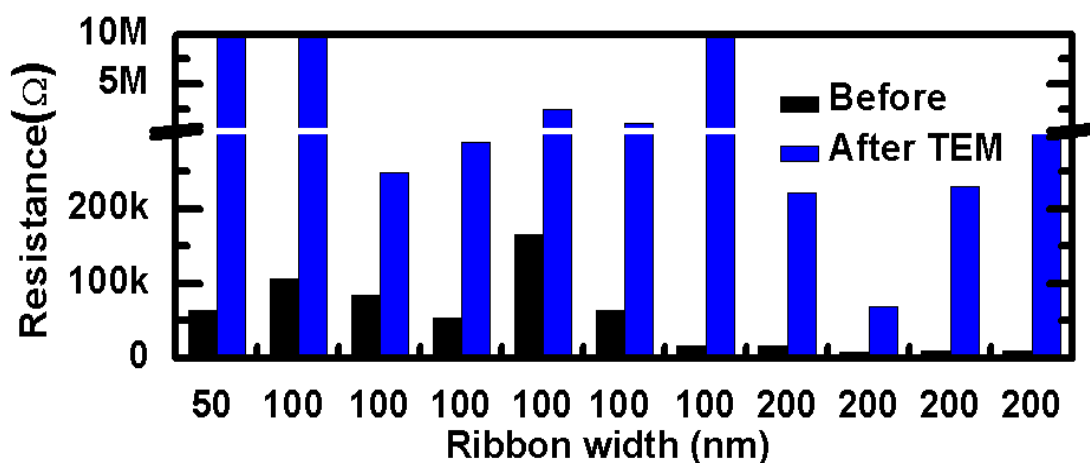


Figure 3.6. Ribbon resistances before and after forming the nanopore in the TEM. Thin ribbons (< 50 nm) rarely survive the pore fabrication procedure.¹⁶

Any portion of the ribbon that is imaged will be damaged, especially at high magnification where there are the highest current densities, but the predominant radius of damaged material appears from TEM images to be $\sim 50 - 100$ nm around the nanopore (Fig. 3.7). This nominal damage radius matches the observation that practically all of the 50 nm ribbons were dead after nanopore formation and corresponds with the area of the ribbon that would be imaged while zooming in to high magnifications to the spot where the pore would be drilled.

The area of damage was only observed in the TEM in devices insulated with a thick (20 nm) Al₂O₃ ALD layer (Fig. 3.7). The damage is not so clearly visible in devices without the insulation layer (Fig. 3.8). This highlights the differences in pore formation dynamics in the different materials.

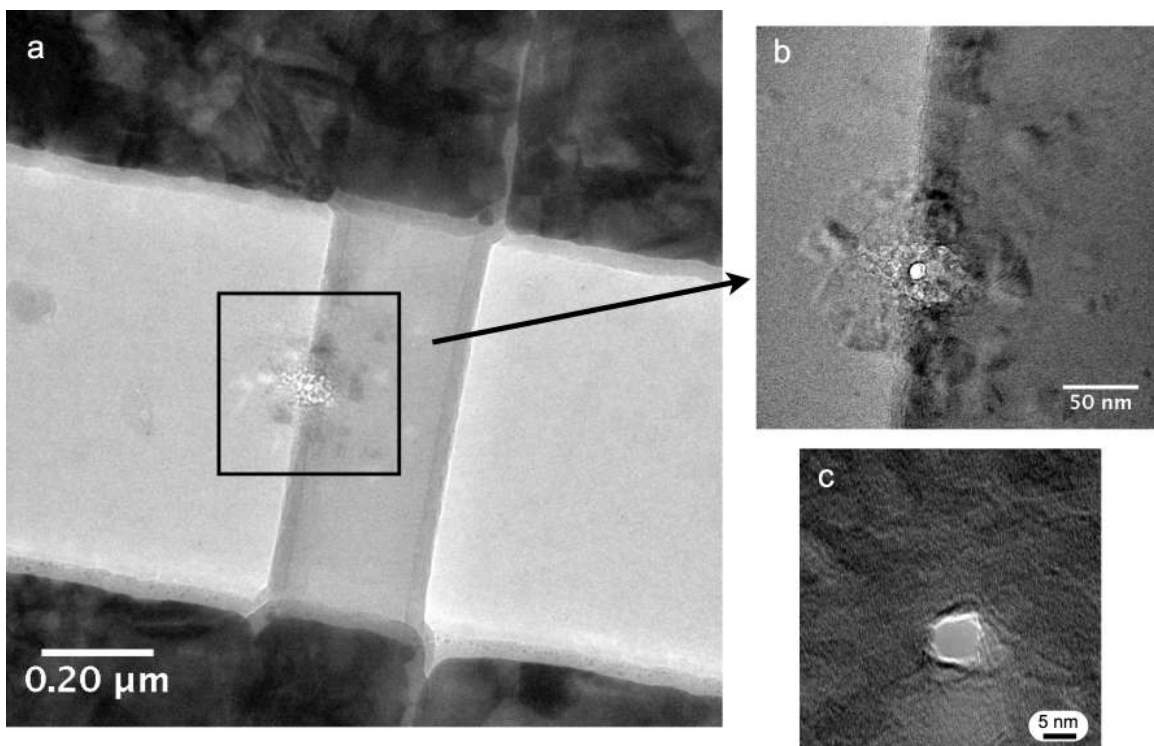


Figure 3.7. Beam-induced damage in a GNR device covered with an Al_2O_3 layer. TEM images at various magnifications (a-c) of one GNR device that was coated with an Al_2O_3 layer grown by atomic-layer-deposition (ALD) and then drilled in TEM mode to form a nanopore at the edge of the GNR. The circular area around the NP where material is damaged is indicated by the black square in (a) and is clearly visible in (b). The damage extends ~ 100 nm from the nanopore (c) shows the zoom in of the nanopore.¹⁶

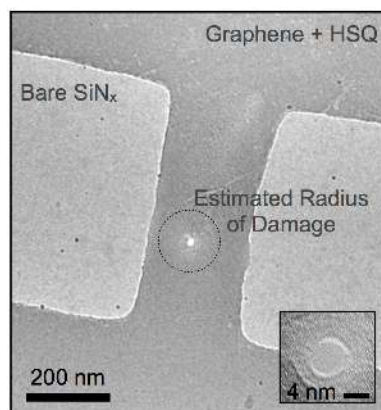


Figure 3.8. Nanopore formed in the center of the GNR ($L = 600$ nm, $w = 240$ nm) by converging the electron beam in TEM mode. The black circle indicates a damaged region within a radius of ~ 75 nm; however, that damage is not visible in the TEM image. *Inset:* High-magnification TEM image of the nanopore ($d = 7$ nm).¹⁶

3.4.2 *In Situ* Measurements of Electron-Beam-Induced Damage

To define optimal conditions for nanopore formation without damage to the GNR, we measured the electron-beam-induced damage in GNRs for different imaging conditions, namely TEM and STEM modes, which, for our purposes, differ mainly in the electron dose imparted on the GNR. In particular, we measured *in situ* the change in resistance of GNRs in a two terminal configuration as a function of electron dose using a TEM sample holder equipped with electrical feedthroughs (Hummingbird Scientific) (Fig. 3.9a).

In TEM imaging mode the spread electron beam continuously irradiates a broad area of the sample under observation, illustrated by a large red circle in the inset of Fig. 3.9b. In this mode, we observed an irreversible and linear increase in GNR resistance with electron irradiation time for imaging conditions used to locate the GNR edge, even prior to fully condensing the beam to form the nanopore (Fig. 3.9b main figure). The increase in resistance of the GNRs is due to the creation of defects in the graphene.^{29,30} For graphene, resistance scales linearly with the density of defects $n_d = \sigma \times D$, where σ is the displacement cross-section^{31,32} and D is the irradiation dose. The dose is defined as the product of the current density (j) and the irradiation time (t). Thus $R \propto n_d = \sigma \times D = \sigma \times t \times j$. Moreover, at higher j , the rate of change of GNR resistance increases, as shown in the inset of Fig. 3.9b for $j = 3, 9$, and $23 \times 10^4 \text{ A m}^{-2}$.

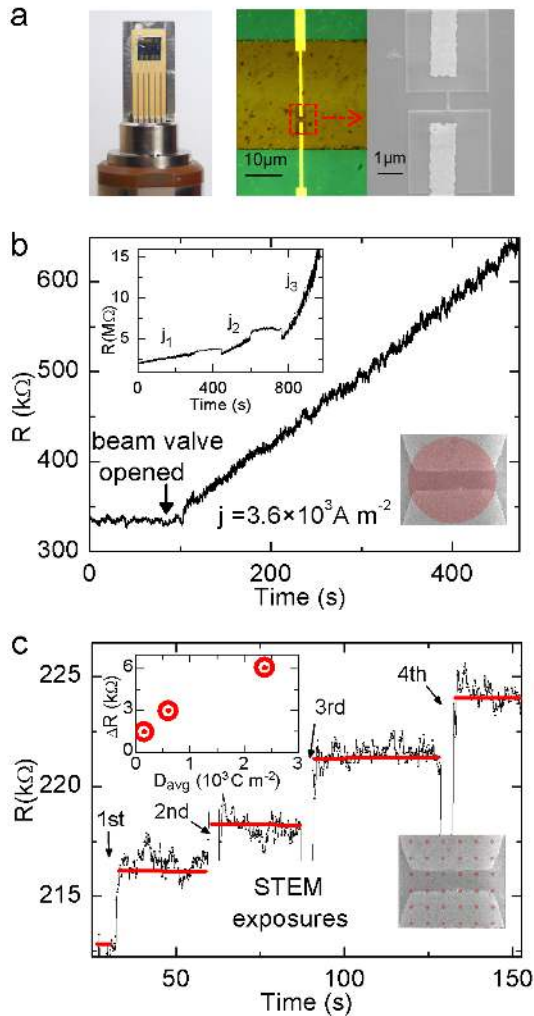


Figure 3.9. *In situ* electrical measurement of the GNR resistance upon exposure to TEM and STEM imaging conditions. a) Optical image of *in situ* TEM sample holder showing a chip with GNR devices. Right panel: optical image showing Au electrodes leading to a GNR device on top of a SiN_x membrane together with a magnified SEM image of the highlighted rectangle. b) *In situ* TEM electrical measurement of GNR resistance vs. time for spread beam TEM imaging. Upon exposure of the GNR at $j = 3.6 \times 10^3 \text{ A m}^{-2}$ (indicated as “beam valve opened”) the resistance increases linearly with time. *Top-left inset of (b)*: the rate of change of resistance increases with current density (j_1 , j_2 , and j_3 are 3 , 9 , and $23 \times 10^4 \text{ A m}^{-2}$, respectively). *Bottom-right inset of (b)*: illustration of a GNR exposed to a spread beam (red circle) in TEM imaging mode. c) *In situ* electrical measurement of GNR resistance vs. time for converged beam STEM imaging. GNR resistance increases in a step-like fashion after each 330 ms scan between the four steps, indicated by arrows. *Top-left inset of (b)*: average increase of resistance (ΔR) per STEM scan exposure as a function of average dose (D_{avg}). *Bottom-right inset of (b)*: illustration of the STEM scan over a GNR. The array of red spots simulates the position of the beam over different pixels.¹⁶

In practice, imaging at higher magnifications correlates with higher current densities. For example, at $\times 800k$ magnification, the GNR was continuously irradiated with a current density of $j = 2.3 \times 10^5 \text{ A m}^{-2}$, in contrast to $j = 3.6 \times 10^3 \text{ A m}^{-2}$ at $\times 100k$ magnification. In TEM mode, these high magnifications are needed to position the nanopore next to the GNR, and the GNR is significantly damaged in a short amount of time. In only 100 seconds of exposure at $j = 3.6 \times 10^3 \text{ A m}^{-2}$ (here $\times 100k$ magnification) a typical GNR resistance increase was $\sim 90 \text{ k}\Omega$ (Fig. 3.9b). For 100 seconds of exposure at $j = 2.3 \times 10^5 \text{ A m}^{-2}$ (here $\times 800k$ magnification), the GNR resistance increased by $\sim 5 \text{ M}\Omega$ (inset of Fig. 3.9b).

In STEM mode, it is possible to image the GNR in order to determine the location to form the nanopore with only one scan and with precise control over dose. In contrast to TEM mode, in STEM mode the converged beam irradiates the sample in discrete locations, schematically depicted as the array of red spots in the inset of Fig. 3.9c. Each STEM image scan results in a step increase in GNR resistance, which can be controlled by the pixel size, beam diameter, and dose at each pixel. A resistance step of $\sim 2.5 \text{ k}\Omega$ in a GNR was seen for a 256×256 pixel image scan with an electron beam diameter of 2.4 nm (convergence angle $\alpha = 24 \text{ mrad}$), a current density $j = 4 \times 10^8 \text{ A m}^{-2}$, a pixel size of 7.8 nm, and a dwell time of 5 μs per pixel. Each discrete spot was irradiated for a total dose $D = 2 \times 10^3 \text{ C m}^{-2}$. Each STEM acquisition takes 330 ms, and the constant resistance time-segments that occur immediately after each acquisition (marked with horizontal red lines in Fig. 3.9c) show that damage only occurs during the short time when the beam scans over the GNR (each scan time is indicated by arrows). We define an *average dose*

for STEM mode as $D_{\text{avg}} = D \times \text{Beam Area} / \text{Pixel Area}$. The average dose for the GNR can also be expressed as the total charge irradiating the GNR divided by the GNR surface area. For a fixed beam diameter, keeping all other parameters constant, decreasing the pixel size increases the average dose and causes a higher change in resistance (ΔR) per scan, as shown in the inset of Fig. 3.9b. Unlike nanopore formation in TEM mode, where damage is localized in a large radius where imaging was performed prior to nanopore formation (Fig. 3.7), any damage incurred during STEM imaging is uniform on average across the GNR, with no preference to the area around the nanopore, ensuring that the device area close to the nanopore is just as sensitive as the rest of the device.

3.4.3 Nanopore Formation in STEM

Based on the *in situ* TEM measurements outlined above, we developed a procedure to position and form nanopores next to or in the center of a GNR in STEM mode while preventing beam induced damage in the GNR. The procedure involves acquiring a single image of the graphene nanoribbon with the low dose conditions described above to resolve its edge, choosing a location to form the nanopore, and moving the beam to that position (Fig. 3.10a). We used High-Angle Annular Dark Field (HAADF) imaging in STEM mode, where the image intensities are proportional to the mass,³³ in order to generate high contrast between the HSQ and SiN_x in a single scan (Fig. 3.10b). Then, a pixel at the edge of the GNR is chosen, and the beam is placed over

that pixel until the pore is formed, as illustrated by the red point in the inset of Figure 3.10b. The 2.4 nm diameter beam was used both to image and then to make the nanopore. These imaging conditions correspond to an average dose of $D_{\text{avg}} = 150 \text{ C m}^{-2}$, a negligible number compared to the dose delivered in TEM mode, $D = 1.2 \times 10^7 \text{ C m}^{-2}$ (60 s at $j = 2.3 \times 10^5 \text{ A m}^{-2}$), during typical positioning of the GNR edge before forming the nanopore. An example of a 4 nm diameter nanopore made with this procedure next to a GNR is shown in the high resolution HAADF STEM image in Figure 3.10c (in contrast to the pixelated image of Figure 3.10b acquired with a lower dose to limit GNR damage). Typically, under these conditions, an electron dose of $D \sim 5 \times 10^{10} \text{ C m}^{-2}$, achieved by a longer dwell time, is sufficient to make a nanopore.^{34,35} A smaller pixel size can be chosen to increase the accuracy with which the nanopore is placed next to the GNR; however this increase in precision, with all other parameters constant, imparts a higher dose on the GNR. GNR resistance does not change while the beam is fixed in place next to the GNR sputtering the SiN_x in order to form the nanopore. Any damage to the GNR is incurred during the imaging prior to fixing the beam in place (provided that the nanopore is at the edge of the GNR and not in the center). A transient increase in resistance was sometimes observed during the STEM image scan due to charging of the SiN_x film, but the resistance quickly recovered to a value close to the original GNR resistance (Fig. 3.10d).

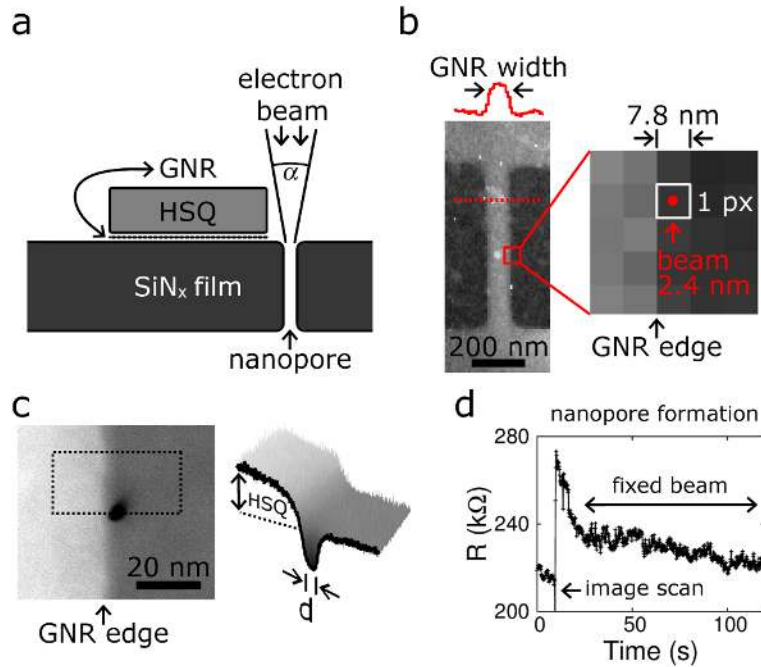


Figure 3.10. Formation of nanopores in STEM mode to avoid electron beam-induced damage in GNRs. a) Diagram showing a cross section of a device with a nanopore in a SiN_x membrane next to a GNR, and the converged electron beam at the nanopore position (diagram not a scale). b) HAADF STEM image showing a 100 nm-wide GNR. The image was taken with a 2.4 nm beam diameter ($j = 0.4 \times 10^9 \text{ A m}^{-2}$), a 7.8 nm pixel size, and a 5 μs dwell time per pixel. Therefore, each pixel received a dose of $2 \times 10^3 \text{ C m}^{-2}$. The inset shows that the contrast provided by the HSQ mask allows positioning of the beam at the edge of the GNR with a precision of ~ 4 nm. The red dot (2.4 nm in diameter) shows the spatial relationship between the beam and the pixel size of the image. c) High resolution HAADF STEM image of a nanopore next to a GNR (the image was taken with a 0.3 nm beam diameter). The right panel shows a perspective view of the image enclosed by the highlighted rectangle. From these intensity profiles it is possible to calculate the nanopore diameter (d) and the length between the nanopore and the GNR. d) Resistance of a GNR during nanopore formation. The spike in the resistance corresponds to an image scan and is indicated by the leftmost arrow. The decay of resistance is a discharging effect. Immediately after the image was acquired the beam was fixed next to the GNR (as in (b)) and left immobile in order to form the nanopore. There is only a small change of resistance in the GNR during this process.¹⁶

3.4.4 Comparison of TEM and STEM Nanopore Drilling Methods

The change in resistance of devices with nanopores drilled in STEM mode is shown in Fig. 3.11. Compared to the changes in resistance observed after TEM mode (Fig. 3.6), these devices show almost no change before and after nanopore formation.

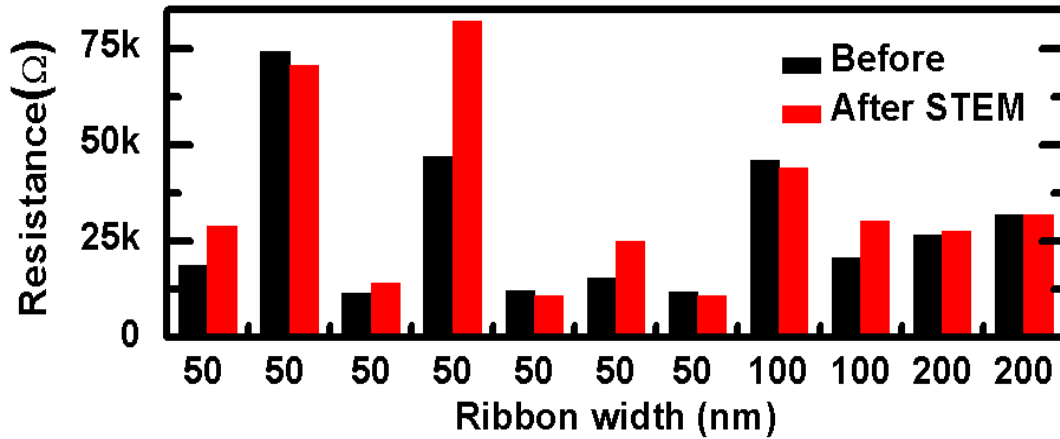


Figure 3.11. Ribbon resistances before and after forming the nanopore in STEM mode. In contrast to TEM mode nanopore formation, 50-nm-wide ribbons show almost no change in resistance after nanopore formation.¹⁶

Another comparison of the two methods of forming pores (TEM vs. STEM) is shown in Fig. 3.12a, where the ratios of the final and initial resistance values after nanopore formation (R_f/R_i) are given as a function of the initial resistance (R_i) for 28 devices (11 with STEM and 17 with TEM). Following nanopore formation in TEM mode (blue squares), 5 out of 17 devices were non-conducting ($R_f > 10 \text{ M}\Omega$), while the resistance for the other devices increased on average ~ 15 times, limiting the sensitivity. All 50 nm wide nanoribbons were practically non-conducting once the nanopore was

formed in TEM mode. In contrast, when the nanopore was formed using the STEM technique (red circles), the resistance was effectively unchanged with $R_f/R_i \sim 1$, regardless of GNR width. The striking difference in resistance is explained by the approximately five orders of magnitude difference in irradiation dose on the GNR between the two methods. It is also important to note that neither current annealing of the GNR after nanopore formation, nor *in situ* current annealing during nanopore formation in the TEM were effective in regaining or retaining the initial GNR resistance once the ribbon was damaged.

Fig. 3.12b compares electrolytic gating curves (conductance vs. V_g) for representative devices *before* (black curves) and *after* formation of the pore with both the STEM and TEM methods (red and blue curves, respectively). The TEM devices exhibit a significantly broader curve than the non-irradiated GNRs, with both lower conductivity and mobility, consistent with a higher density of defects. The gating curves for STEM devices fall within the range of gating curves for devices before irradiation (the three black curves show the device-to-device variation), preserving both conductivity and mobility and making the STEM devices more sensitive to changes in local electric potential than those produced in TEM mode. The STEM devices show a relative change of GNR resistance with gate voltage in solution as high as $(\Delta R/R) / \Delta V_g \sim 1\% / \text{mV}$. Because of their low resistances (on the order of $10 \text{ k}\Omega$), resulting STEM GNRs are able to sustain micro ampere currents at low voltages in buffered electrolyte solution, as needed for high bandwidth detection.

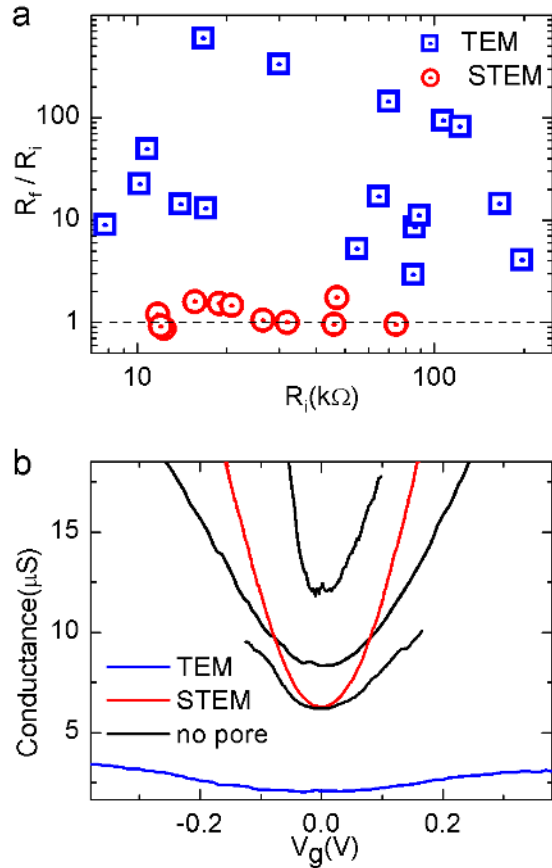


Figure 3.12. Comparison of GNR electrical properties after TEM and STEM nanopore formation methods. a) Relative increase in resistance before (R_i) and after (R_f) nanopore formation for 28 GNR-NP devices made with the TEM method (17, blue squares) and STEM method (11, red circles), as a function of initial resistance. b) GNR conductance vs. gate voltage (V_g) measured in 1M KCl solution for representative devices before (black curves) and after nanopore formation with TEM (blue) and STEM (red) methods. For clarity, these curves were shifted so that the charge neutrality point is at $V_g = 0$ V. There is some device-to-device variation in mobility and conductance, and three devices before nanopore formation were chosen to represent that variation.¹⁶

3.5 Graphene Nanoribbon Measurements during DNA Translocation

3.5.1 Methods

Although not mentioned before in the procedures for nanopore drilling, an important detail in the drilling procedure is that we use a gold plated TEM sample holder. Samples blew-up > 50% of the time while mounting the sample or in the TEM with standard brass holders. The gold plated holder makes better contact with the contact pads on the device and ensures that they are all at the same potential.

After the nanopore is formed, the sample is mounted overtop of a hole on a custom PCB, such that there is fluid access to both the top and bottom of the device (Fig. 3.13a). The device contacts are wire bonded to the PCB, and then the entire PCB is plasma cleaned for 1 minute in 5% H₂ / 95% O₂ using a Gatan plasma cleaner and recipe designed for fragile thin TEM samples. The plasma treatment makes the SiN_x hydrophilic and cleans the substrate again immediately before the measurement. One end of the PCB fits into a home-made teflon microfluidic cell (Fig. 3.13b) that feeds 50 µL of solution to each side of the membrane. The other side of the PCB plugs in to a BNC breakout box for easy interfacing with the device. The PCB and fluidic cell were designed to prevent device blow-ups during measurement, to make fluid exchange and the addition of DNA easy, and to reduce solvent evaporation, which raises the salt concentration (many thanks to Gautam Nagaraj for his summer work on this setup). Ag/AgCl electrodes connect to

each reservoir, and either a) shielding those electrodes or b) keeping their length short helps to reduce noise in the measurement.

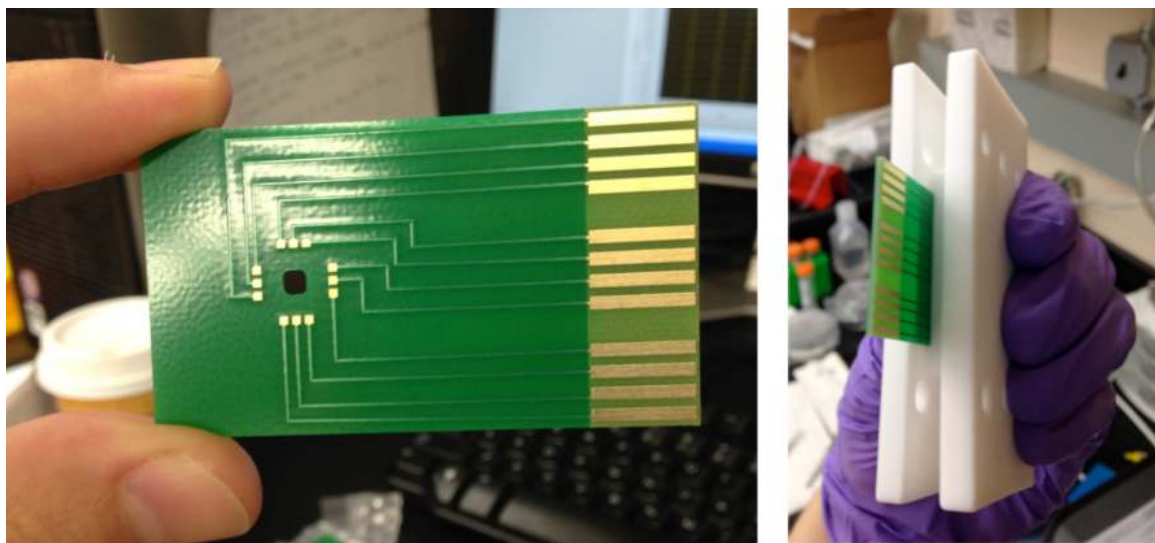


Figure 3.13. *Left*: Custom PCB with a hole on top of which the SiN_x chip with graphene device is mounted. *Right*: Home-built teflon microfluidic cell. Fluid is delivered to the device on one side through a channel, and there is a well on the opposite side.

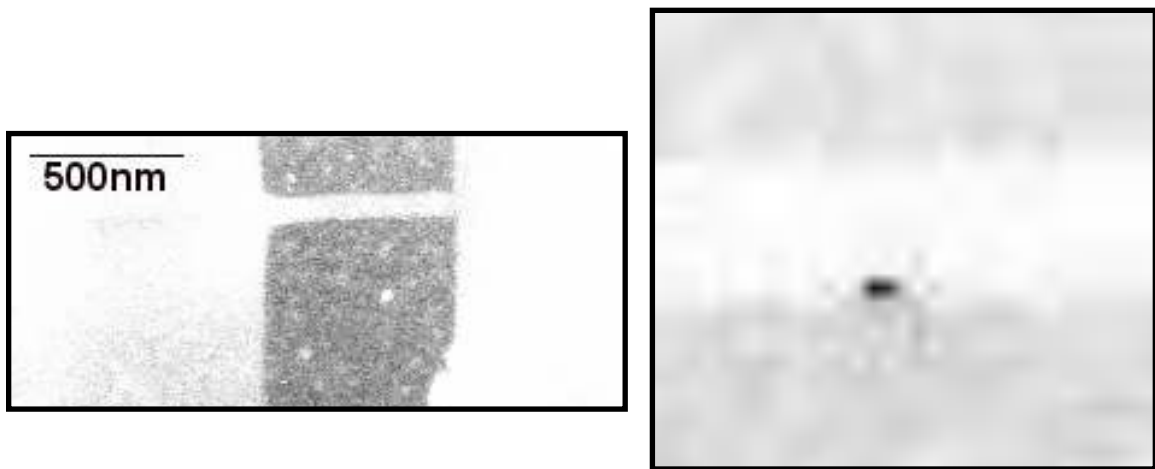


Figure 3.14. HAADF STEM images of the graphene nanoribbon before (*left*) and after (*right*) STEM drilling of a nanopore. There was no change in device resistance after pore formation and low-dose imaging.

Ionic translocations were observed in nanopores next to graphene ribbons (Fig. 3.14) for salt concentrations from a) 1 M KCl on both sides of the membrane down to b) 0.1 mM (ribbon side) / 1M (bottom side) and down to c) 10 mM KCl on both sides of the membrane. The currents through the ribbon and the pore were measured simultaneously with two HEKA patch-clamp amplifiers. An electrical cross-talk between the two headstages artificially inflates the noise seen in these graphs. That cross-talk comes in the form of periodic up and down spikes which, because of the periodicity and magnitude, can be easily distinguished from other signals when the data is viewed at shorter time-scales (it is not visible, for instance, when we zoom-in to events in Fig. 3.15 b,c). In the data shown, the cross-talk appears as a constant high frequency noise appearing to thicken the baseline current signal. The cross-talk is not present when we use a Fempto high-frequency amplifier in place of the HEKA amplifier.

3.5.2 Ribbon Detection Results

At low ribbon currents, at both high and low salts, there is a correlation between the signal in the ribbon data and the ionic current translocations (Fig. 3.15a) (note: the correlation can be seen regardless of choice of amplifiers and is not related to the cross-talk). The signal in the ribbon appears as the derivative of the ionic current (Fig. 3.15b,c). As we increase the current in the ribbon for both positive and negative voltages, the correlated peaks remain the same in magnitude but become enveloped in the increasing

noise (Fig. 3.16a). If this were a response of the ribbon to a change in potential, we would expect the magnitude of the response to increase in proportion to an increase in source-drain current.

Upon transitioning to lower salt on the device side of the membrane, there is no improvement in signal-to-noise of ribbon signal as expected for a longer screening length (Fig. 3.16b). Instead, there is actually a moderate decrease in the magnitude of the derivative response in the ribbon. This behavior was true for both damaged (after TEM drilling) and undamaged (after STEM drilling) graphene nanoribbon devices, contrary to what we expected. We also found that a gold contact held at ground near the nanopore with no graphene device, measuring only leakage into and out of the contact, shows the same correlated signal.

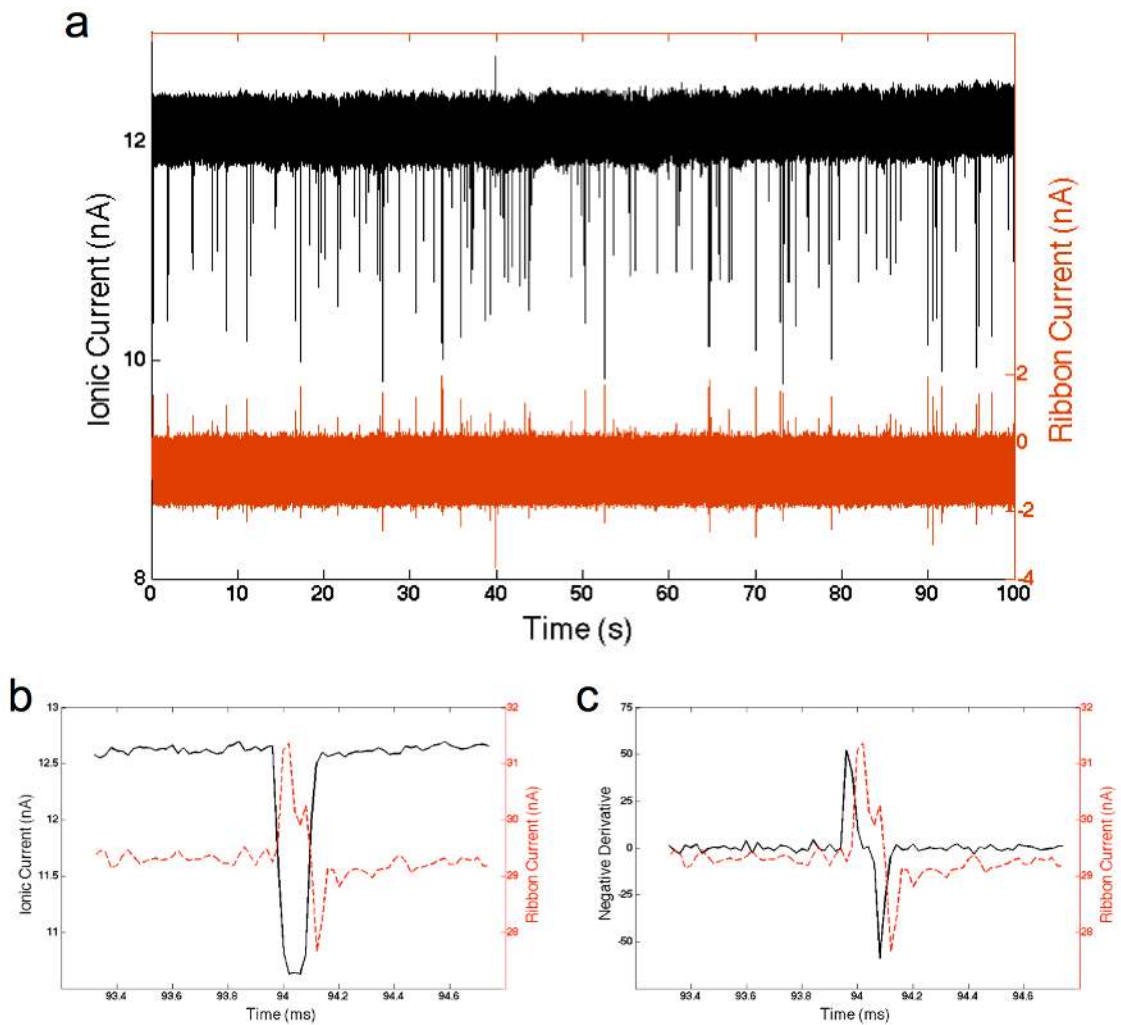


Figure 3.15. a) Correlation of ionic translocation signal (black) and graphene nanoribbon signal (red) for low currents in the graphene ribbon at 1 M KCl. The ribbon was 220 nm wide, 550 nm long with a 7 nm pore at the edge of the ribbon. Before creating the pore the resistance was $7.8\text{ k}\Omega$. After drilling the pore in TEM mode, the resistance went up to $70\text{ k}\Omega$. b) shows one ionic translocation event (black) plotted along with the correlated ribbon event (red). c) shows the negative derivative of the ionic translocation event (black) plotted along with the ribbon event (red). Note: the noise presented on the individual events is the noise when no cross-talk noise is present. Many events, like this one, occur between the periodic cross-talk signals.

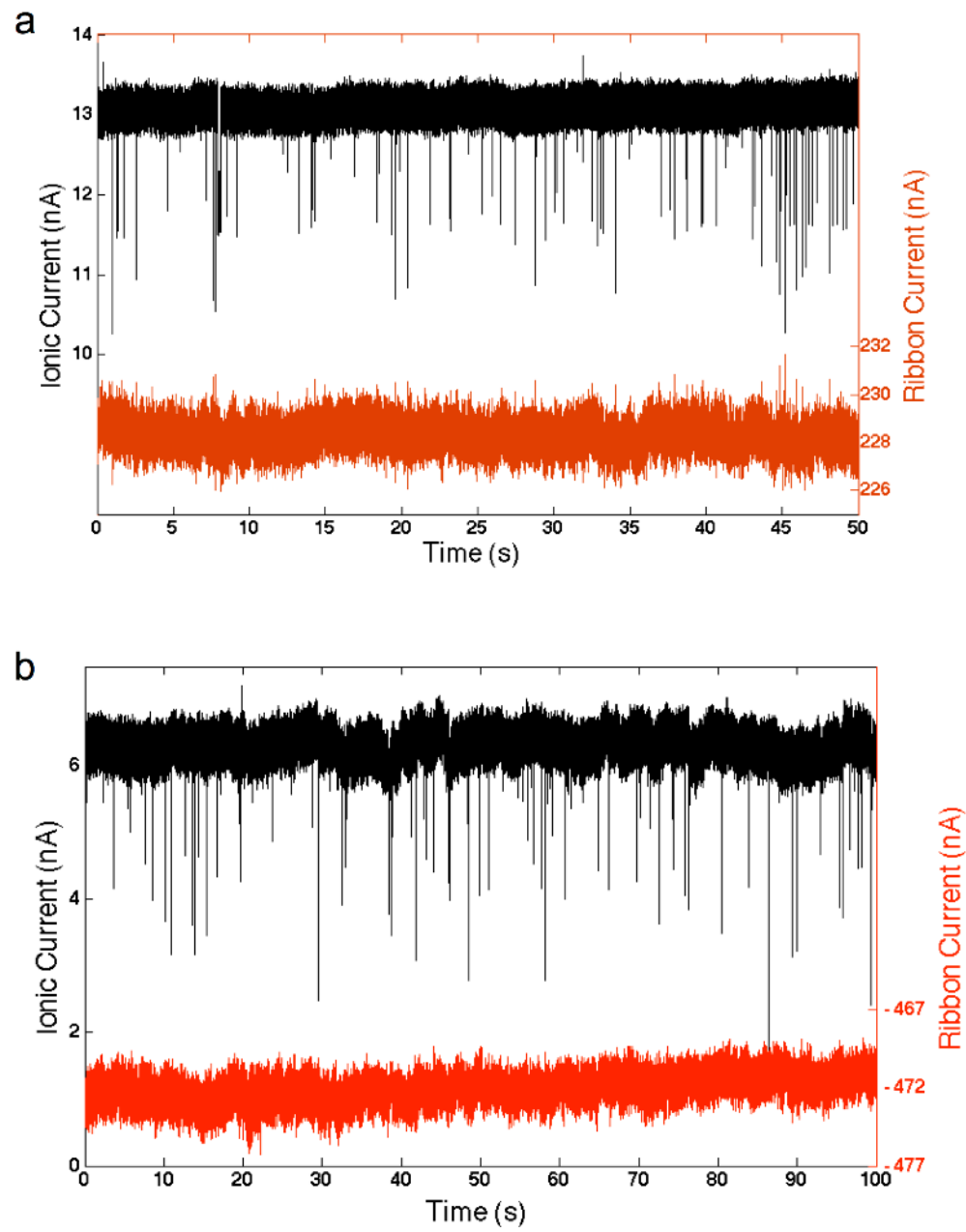


Figure 3.16. a) Same device from Fig. 3.15 but with a higher current through the ribbon (1 M KCl). b) High current through the ribbon at low salt (10 mM KCl on ribbon side, 1 M KCl on the opposite side) and no correlation (different device than a)).

It also appears that the addition of DNA in solution above the device does not influence the noise in the device, as indicated by the graph of the power spectral density (Fig. 3.17). The two curves are nearly overlapping, with the low frequency amplitudes within error of each other.

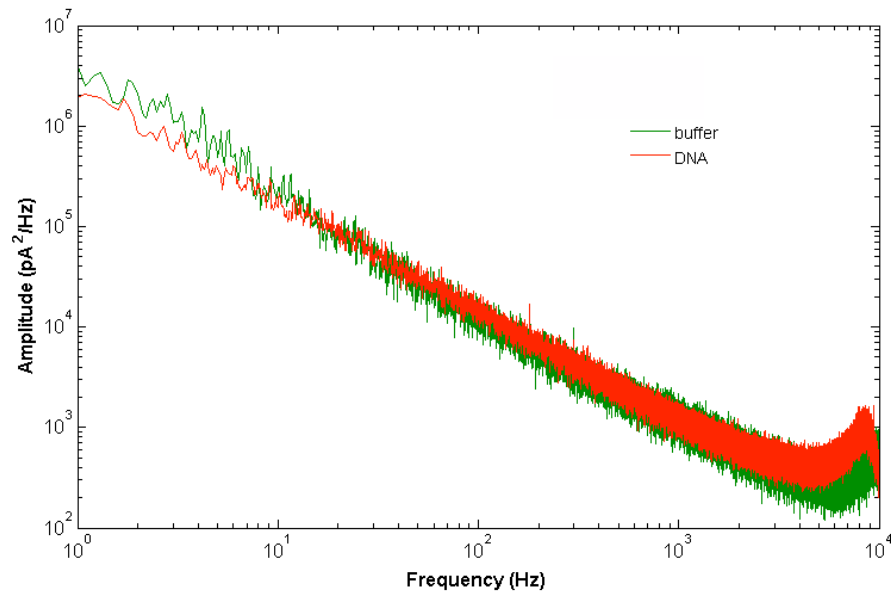


Figure 3.17. Power spectral density curves for a 100 nm graphene ribbon in 1 M KCl, with and without DNA (1 nM concentration of 15 kbp dsDNA). There is no nanopore on this device. 50 mV applied to the ribbon.

3.5.3 Circuit Simulation to Explain Correlation

The fact that we observe the same correlation in a grounded electrode near the pore suggests a capacitive source of the correlated signal. A schematic for the graphene device measurement is reproduced in Fig. 3.18 next to the effective circuit diagram for

the single gold electrode, where R_{sol} are solution resistances (\sim hundreds of Ohms, including the resistance at the electrode), R_{contact} is the resistance for leakage at the device (\sim MOhms), and C_{contact} is the capacitance between solution and the device. Circuit simulations of the circuit shown in Fig. 3.18b reveal, in response to translocation-like pulses on the ionic channel, a similar derivative signal on I_{contact} to those shown in Fig 3.15 when both of the following are true:

- a) $R_{\text{sol-1}} \gg R_{\text{contact}}$. i.e. the resistance for current flow from solution into the device (or *vice versa*) is much greater than resistance of the solution ($R_{\text{sol-1}}$) — this is certainly the case in our devices,
- b) the capacitance between the device and solution is $C_{\text{contact}} \sim 1 \text{ nF}$.

Essentially, the capacitance of the device and/or contact (C_{contact}) in solution is high enough that any change in potential couples through the capacitance to produce a transient current in the device ($I_{\text{contact}} = dq/dt = C \times dV/dt$), observed as the derivative of the ionic translocation event. For capacitance values several orders of magnitude smaller (which could be achieved with ALD insulation), the derivative signal was barely, if at all, visible.

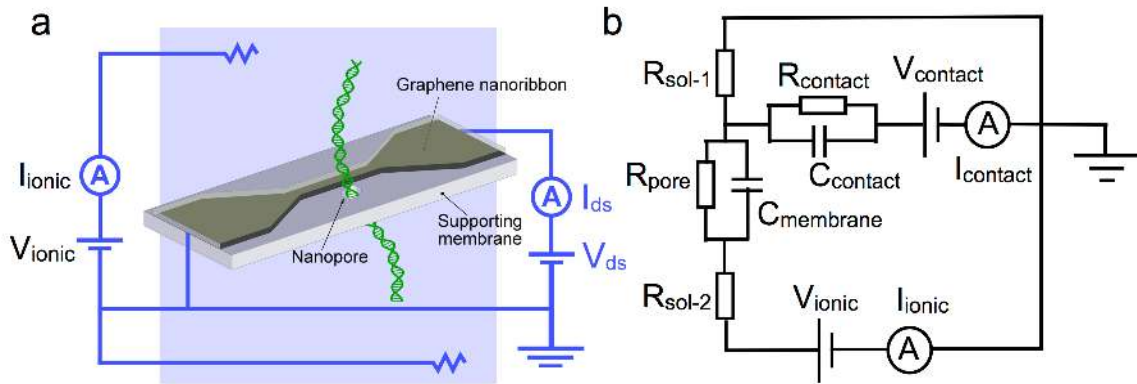


Figure 3.18. a) Cartoon depicting GNR + nanopore circuits. b) Circuit diagram for the case when a single gold contact on one side of the membrane in solution is connected to a second headstage, while the first headstage drives ionic translocations.

3.6 Conclusions and Prospectus

In summary, we developed a sensor for single-molecule detection in buffered electrolyte solution consisting of nanopores in SiN_x membranes next to or in the center of graphene nanoribbons with widths down to 50 nm. We prove with *in situ* TEM electrical measurements that a procedure of forming a nanopore next to a GNR in TEM mode exposes the GNR to an electron dose of $D \sim 10^7 \text{ C m}^{-2}$ and significantly decreases its conductance and mobility. A STEM-based method was developed with which it is possible to form a nanopore next to the edge of a GNR, exposing the GNR to an average dose of only $D_{\text{avg}} \sim 10^2 \text{ C m}^{-2}$, five orders of magnitude less than the TEM method. These

improved GNR devices show a modulation in resistance to uniform changes in the local potential of $\sim 1\% / \text{mV}$.

This degree of sensitivity is not enough, however, to detect DNA molecules translocating through the nanopore, considering the thickness of the HSQ and the width of the graphene ribbon.

With the STEM technique developed here for preventing damage to the ribbon, it would also be possible to intentionally damage the ribbon with high electron doses in specified regions to thin the ribbon to thicknesses less than 50 nm. Lithography of this precision is not possible with any other technique. This process requires no additional modification to the device design, which was optimized for high translocation yield, and the nanopore can be made within the same process flow next to the pristine portion of the ribbon – all of which can be done with *in situ* monitoring of the current through the device at each step.

Based on what we have reported on the currents, sensitivity, and noise of these graphene devices in solution, the most optimistic outlook would predict changes in graphene current during translocation of 10s of nAs. This would be only a few times larger than current solid-state nanopore signals, not an improvement of several orders of magnitude. 2D MoS₂ crystals would offer a much higher rate of change, with changes in resistance spanning several orders of magnitude. But this comes with the trade-off that at zero-gate-bias, the material is not very conductive. The techniques developed here, however, can be directly applied to make nanopores next to devices made out of any 2D material. Rather than a fabrication challenge, the challenge will be in simulating the

potential fields and ribbon response, in order to ensure that the device operates in a sensitive portion of its gate-response curve and generates signals that are large enough to be resolved above the noise and leakage.

3.7 References

1. Manrao, E. A. *et al.* Reading DNA at single-nucleotide resolution with a mutant MspA nanopore and phi29 DNA polymerase. *Nat Biotechnol* **30**, 349–353 (2012).
2. Squires, A. H., Hersey, J. S., Grinstaff, M. W. & Meller, A. A Nanopore-Nanofiber Mesh Biosensor To Control DNA Translocation. *J. Am. Chem. Soc.* **135**, 16304–16307 (2013).
3. Larkin, J. *et al.* Slow DNA Transport through Nanopores in Hafnium Oxide Membranes. *ACS Nano* **7**, 10121–10128 (2013).
4. Balan, A. *et al.* Improving Signal-to-Noise Performance for DNA Translocation in Solid-State Nanopores at MHz Bandwidths. *Nano Lett.* **14**, 7215–7220 (2014).
5. Rosenstein, J. K., Wanunu, M., Merchant, C. A., Drndic, M. & Shepard, K. L. Integrated nanopore sensing platform with sub-microsecond temporal resolution. *Nat Meth* **9**, 487–492 (2012).
6. Han, M., Özyilmaz, B., Zhang, Y. & Kim, P. Energy Band-Gap Engineering of Graphene Nanoribbons. *Phys. Rev. Lett.* **98**, 206805 (2007).
7. Chen, Z., Lin, Y.-M., Rooks, M. J. & Avouris, P. Graphene nano-ribbon electronics. *Physica E: Low-dimensional Systems and Nanostructures* **40**, 228–232 (2012).
8. Özyilmaz, B., Jarillo-Herrero, P., Efetov, D. & Kim, P. Electronic transport in locally gated graphene nanoconstrictions. *Appl. Phys. Lett.* **91**, 192107 (2007).
9. Lu, Y. *et al.* High-on/off-ratio graphene nanoconstriction field-effect transistor. *Small* **6**, 2748–2754 (2010).
10. Fischbein, M. D. & Drndic, M. Sub-10 nm device fabrication in a transmission electron microscope. *Nano Lett.* **7**, 1329–1337 (2007).
11. Fischbein, M. D. & Drndic, M. Electron beam nanosculpting of suspended graphene sheets. *Appl. Phys. Lett.* **93**, 113107 (2008).
12. Lu, Y., Merchant, C. A., Drndic, M. & Johnson, A. T. C. In Situ Electronic Characterization of Graphene Nanoconstrictions Fabricated in a Transmission Electron Microscope. *Nano Lett.* **11**, 5184–5188 (2011).

13. Luo, Z. *et al.* Effect of Substrate Roughness and Feedstock Concentration on Growth of Wafer-Scale Graphene at Atmospheric Pressure. *Chem. Mater.* **23**, 1441–1447 (2011).
14. Yang, J. K. *et al.* Understanding of hydrogen silsesquioxane electron resist for sub-5-nm-half-pitch lithography. *J. Vac. Sci. Technol. B* **27**, 2622–2627 (2009).
15. Nam, S.-W. *et al.* Contrast enhancement behavior of hydrogen silsesquioxane in a salty develope. *J. Vac. Sci. Technol. B* **27**, 2635–2639 (2009).
16. Puster, M., Rodríguez-Manzo, J. A., Balan, A. & Drndic, M. Toward Sensitive Graphene Nanoribbon–Nanopore Devices by Preventing Electron Beam-Induced Damage. *ACS Nano* **7**, 11283–11289 (2013).
17. Nelson, T., Zhang, B. & Prezhdo, O. V. Detection of Nucleic Acids with Graphene Nanopores: Ab Initio Characterization of a Novel Sequencing Device. *Nano Lett.* **10**, 3237–3242 (2010).
18. Min, S. K., Kim, W. Y., Cho, Y. & Kim, K. S. Fast DNA sequencing with a graphene-based nanochannel device. *Nature Nanotech* **6**, 162–165 (2011).
19. Saha, K. K., Drndic, M. & Nikolić, B. K. DNA Base-Specific Modulation of Microampere Transverse Edge Currents through a Metallic Graphene Nanoribbon with a Nanopore. *Nano Lett.* **12**, 50–55 (2012).
20. Avdoshenko, S. M. *et al.* Dynamic and Electronic Transport Properties of DNA Translocation through Graphene Nanopores. *Nano Lett.* **13**, 1969–1976 (2013).
21. Girdhar, A., Sathe, C., Schulten, K. & Leburton, J.-P. Graphene quantum point contact transistor for DNA sensing. *Proceedings of the National Academy of Sciences* **110**, 16748–16753 (2013).
22. Xie, P., Xiong, Q., Fang, Y., Qing, Q. & Lieber, C. M. Local electrical potential detection of DNA by nanowire–nanopore sensors. *Nature Nanotech* **7**, 119–125 (2011).
23. Chen, J. H. *et al.* Charged-impurity scattering in graphene. *Nat Phys* **4**, 377–381 (2008).
24. Pirkle, A. *et al.* The effect of chemical residues on the physical and electrical properties of chemical vapor deposited graphene transferred to SiO₂. *Appl. Phys. Lett.* **99**, 122108 (2011).
25. Lin, Y.-C. *et al.* Graphene annealing: how clean can it be? *Nano Lett.* **12**, 414–419 (2011).

26. Wanunu, M., Morrison, W., Rabin, Y., Grosberg, A. Y. & Meller, A. Electrostatic focusing of unlabelled DNA into nanoscale pores using a salt gradient. *Nature Nanotech* **5**, 160–165 (2009).
27. Meyer, J. C. *et al.* Accurate measurement of electron beam induced displacement cross sections for single-layer graphene. *Phys. Rev. Lett.* **108**, 196102 (2012).
28. Banhart, F., Kotakoski, J. & Krasheninnikov, A. V. Structural Defects in Graphene. *ACS Nano* **5**, 26–41 (2011).
29. Childres, I. *et al.* Effect of electron-beam irradiation on graphene field effect devices. *Appl. Phys. Lett.* **97**, 173109 (2010).
30. Chen, J.-H., Cullen, W., Jang, C., Fuhrer, M. & Williams, E. Defect Scattering in Graphene. *Phys. Rev. Lett.* **102**, 236805 (2009).
31. Banhart, F. Irradiation effects in carbon nanostructures. *Rep. Prog. Phys.* **62**, 1181 (1999).
32. Egerton, R. F., Li, P. & Malac, M. Radiation damage in the TEM and SEM. *Micron* **35**, 399–409 (2004).
33. Williams, D. B. & Carter, C. B. *Transmission Electron Microscopy*. (Springer, 2009).
34. Howitt, D. G., Chen, S. J., Gierhart, B. C., Smith, R. L. & Collins, S. D. The electron beam hole drilling of silicon nitride thin films. *J. Appl. Phys.* **103**, 024310 (2008).
35. Kim, H.-M., Lee, M.-H. & Kim, K.-B. Theoretical and experimental study of nanopore drilling by a focused electron beam in transmission electron microscopy. *Nanotechnology* **22**, 275303 (2011).

Chapter 4

EFM Imaging of Charge Transport through Quantum Dot Arrays

4.1 Introduction

The size dependent properties of colloidal quantum dots (QDs), or semiconducting nanocrystals, make them compelling tunable nano-materials for optical and electronic applications.^{1,2} While quantum dots are sometimes referred to as “artificial atoms,” the wealth of superlattice structures³ that self-assemble from these building blocks have earned the moniker of “artificial solids” because of the potential for emergent material properties as a function of the constituent QD “atoms” and their crystalline-like structures.

Arrays of quantum dots, as assembled by drop casting or spinning, tend to be insulating. This is, perhaps, not surprising because the semiconducting particles are typically separated by insulating organic molecules (ligands) which stabilize the particle during synthesis and in solvents. There are a variety of tricks to improve conduction,

including annealing,⁴ removing the ligands, or exchanging the ligands,⁵ all of which in general reduce the inter-particle spacing. The combination of tunable size, size-dependent properties, and inter-particle coupling in assemblies make for a rich, albeit complex, space for manipulating and studying electrical transport processes in these materials.

Inspired by the diversity of transport phenomena reported in the literature for QD arrays,⁶⁻²⁰ we examined how local thickness variations, particle spacing, and local structure variation affected conduction in arrays of 6.8 nm PbSe QDs. To do so, we made a two-terminal QD device on a suspended SiN_x membrane that allows for measurement of topography with atomic force microscopy (AFM), of film charging and conduction with electrostatic force microscopy (EFM),²¹⁻²³ and of structural details and inter-particle spacing with TEM, all on the same sample.

After annealing the film and upon application of a voltage across the device, rather than a homogeneous diffusion of charge away from the electrodes,^{23,24} we found an immediate, voltage dependent, inhomogeneous charging of the QD film. The pattern of charge followed topographic features seen in the AFM image, but in some areas abruptly stopped even while the thickness of the film appeared continuous. In the TEM, we were able to inspect the QD film structure more closely and found that grain boundaries between superlattices, narrow lateral constrictions, and monolayers all limited conduction. There were also instances where charge injection appeared limited by disruptions to QD lattice structure near the contacts.

For many applications, it is possible to simply fill in these voids and cracks with additional depositions of QDs. What our work highlights, however, is that the superlattice microstructure can have an important effect on the macro-device properties. This is especially true as the field begins to harness emergent properties from carefully tailored superlattice structures and compositions. By filling in voids, it is possible to make the film continuous, but the composition and continuity of the superlattice structures will be altered. Just as grain boundaries, interstitials, and lattice mismatches can affect crystalline material properties, analogous features will affect emergent properties in QD “artificial solids.”

4.2 Theoretical Description of AFM Techniques

In this chapter we use a combination of tapping mode AFM and electrostatic force microscopy²⁵ — sometimes also referred to as electric force microscopy and very similar to kelvin probe microscopy (KPM) — to characterize the charging of annealed QD films. Tapping mode AFM is a classic example of a driven simple harmonic oscillator. In this mode a piezo drives the AFM cantilever near its resonant frequency, and the motion of the tip position can be described by:

$$\frac{d^2z}{dt^2} + \frac{\omega_0}{Q} \frac{dz}{dt} + \omega_0^2 z = \frac{F_0}{m} \cos(\omega t) \quad (4.1)$$

where t is time, z is the tip position away from equilibrium, ω_0 is the cantilever resonance, Q is the quality factor of the cantilever ($Q = m\omega_0/b$, where b is the damping coefficient), F_0 is the amplitude of the driving force, and m is the mass of the tip or the effective mass.

The solution to the driven oscillator equation can be expressed as:

$$z(t) = A(\omega) \cos(\omega t - \varphi(\omega)) \quad (4.2)$$

And the amplitude and phase, respectively, are:

$$A(\omega) = \left(\frac{F_0}{m} \right) \frac{1}{\sqrt{(\omega_0^2 - \omega^2)^2 + \left(\frac{\omega_0 \omega}{Q} \right)^2}} \quad (4.3)$$

$$\varphi(\omega) = \tan^{-1} \left(\frac{\omega_0 \omega}{Q (\omega_0^2 - \omega^2)} \right) \quad (4.4)$$

When the tip and cantilever are lowered to a distance only a few nanometers away from the surface of a material, Van der Waals forces exert an attractive force on the cantilever (F), perturbing the frequency at which it is resonating. The change in oscillation amplitude, frequency, and phase are given by:

$$\Delta A = \frac{2QA_0}{3\sqrt{3} \left(k - \frac{\partial F}{\partial z} \right)} \left(\frac{\partial F}{\partial z} \right) \quad (4.5)$$

$$\Delta \omega = - \frac{\omega_0}{2k} \frac{\partial F}{\partial z} \quad (4.6)$$

$$\Delta \varphi = - \frac{Q}{k} \frac{\partial F}{\partial z} \quad (4.7)$$

Tapping mode height measurements typically operate in amplitude-feedback mode, which means that when the AFM detects a decrease in amplitude of oscillation, it retracts the tip until the original amplitude is restored. In this way it directly maps out the topography of the sample.

EFM is a dual scan measurement, meaning that each line of the sample is scanned twice. The first scan is a standard height scan, but in the second scan, the tip retraces the topography at a constant lift height (in our case we use 10 nm). During this second scan, a voltage is applied to the electrodes and/or the tip. At a distance of 10 nm, the tip detects only longer range electrostatic forces between the charged film and the conductive tip. The general method for quantifying the changes in potential across a sample is to consider the electrostatic force on the tip when the tip and sample are treated as a capacitor:

$$F = -\frac{dU}{dz} = -\frac{d}{dz}\left(\frac{CV^2}{2}\right) = -\frac{V^2}{2} \frac{dC}{dz} \quad (4.9)$$

Changes in potential across the film cause a phase shift in the cantilever, and the EFM image maps the magnitude of those phase shifts across the sample. Note that the force is proportional to the square of the voltage; therefore there is an attractive force between tip and sample for both positive and negative potentials.

Previous quantum dot EFM measurements have extracted the magnitude and sign of charge, the dielectric constant, and the polarizability of single isolated quantum dots using an AC-voltage lock-in EFM technique.^{26,27} The results here proved difficult to

quantify because of the inhomogeneity of the charging patterns, but qualitatively we were still able to observe the influence of the film microstructure on the charge transport.

4.3 EFM Imaging Correlated with TEM and AFM

4.3.1 Methods

The optical and electrical properties of PbSe QDs degrade upon exposure to oxygen, therefore all AFM measurements were made in an environmentally controlled AFM chamber, which also offers *in situ* stage heating capabilities. 6.8 nm PbSe QDs (with ~ 2 nm oleic acid ligands) in 9:1 hexane / octane solvent were drop-cast onto a 2 terminal device on a SiN_x window that was attached to the AFM stage and immediately placed in the AFM chamber. The chamber was then evacuated down to ~ 10⁻⁵ Torr. The sample was allowed to dry in high vacuum for several hours, imaged with AFM/EFM, and then annealed at 130°C overnight in high vacuum. After annealing, all AFM/EFM measurements were made under N₂ gas flow. Despite the environmental control, the conductance of the QD arrays was still observed to decrease over the course of two weeks.

The AFM stage was modified to allow for *in situ* application of voltages to the device electrodes during AFM/EFM imaging (Fig. 4.1). Sample contacts were wire bonded to pins on the stage, which connect by electrical feedthroughs to a BNC break-out

box outside the AFM. The minimum current levels measurable with this setup are ~ 20 pA. It is also possible to apply voltages directly to the conductive AFM tip.

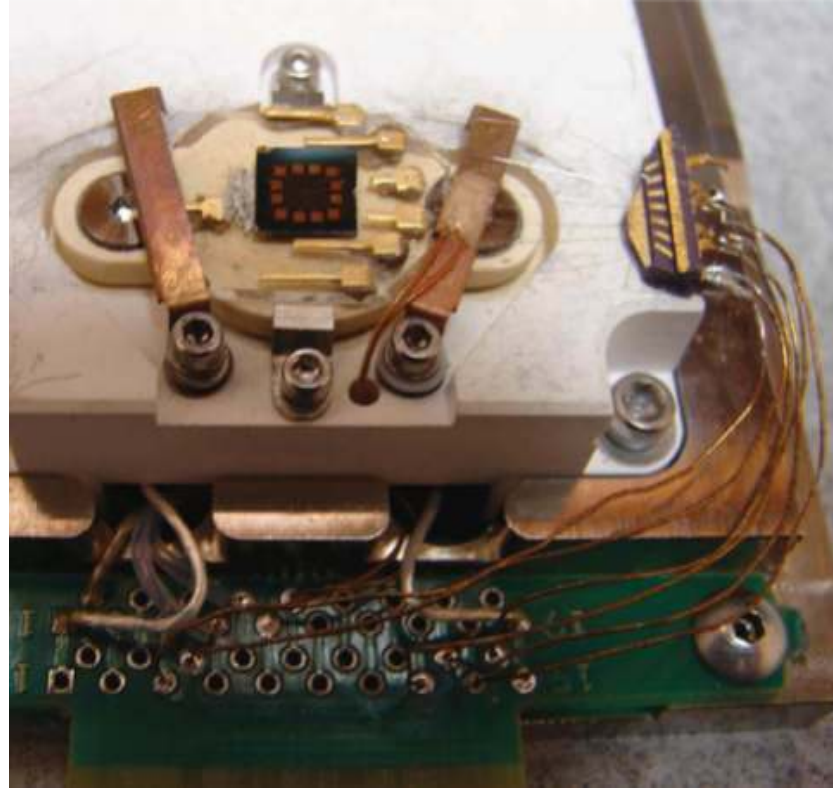


Figure 4.1. Modified AFM stage for EFM measurements of QD array devices. The QD array sits on top of the contacts on the SiN_x window shown in the center of the stage.

4.3.2 Results

Before depositing the QDs, the response of a bare device was measured with both AFM and EFM (Fig. 4.2). The top electrode does not appear in the EFM image because it is held at the same potential as the AFM tip (ground). The bottom electrode is held at -10 V, which induces an attractive force on the grounded tip and results in a measured frequency shift in the cantilever oscillations. The halo around the electrode represents a

lateral force on the tip and is a limitation to EFM resolution at high voltage differences. This measurement serves as a control to ensure that only the locations where voltage is applied are detected in the EFM scan.

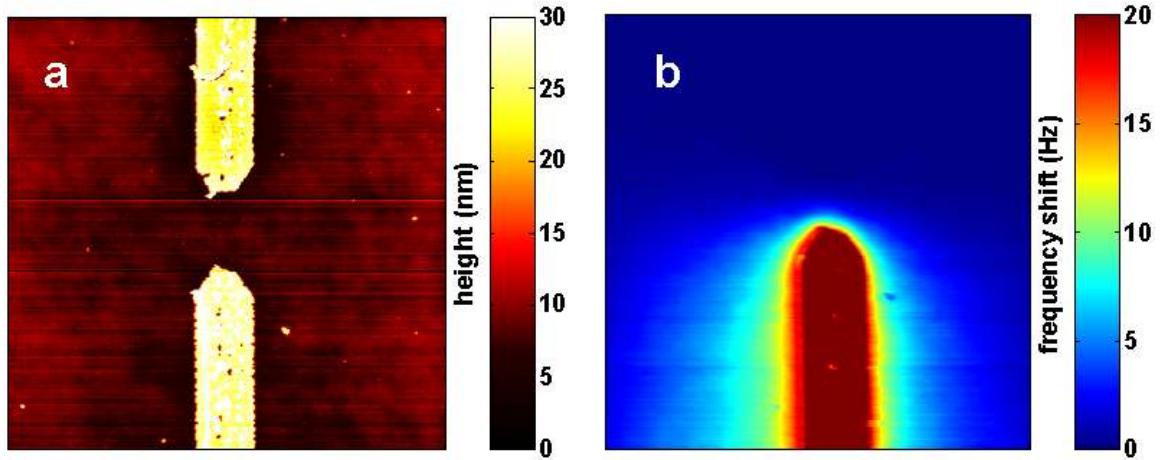


Figure 4.2. Bare device before QDs were drop-cast. a) AFM height image with no voltage applied to the electrodes (voltage was never applied to the electrodes during the height scan). b) EFM frequency shift image with -10 V on the lower electrode and the top electrode and AFM tip grounded. (each image is 15 $\mu\text{m} \times 15 \mu\text{m}$)²⁸

The pattern of the QD film upon drop-casting and rapid drying under high vacuum is shown in Fig. 4.3. From the AFM image (Fig. 4.3a), it is not clear whether there is a percolating path for current between the electrodes, and in fact for a potential difference of 10 V between electrodes, there was no measurable current. The EFM image (Fig. 4.3b) still exhibits a similar halo as seen in Fig. 4.2 for the bare device. The faint charging observed on the top electrode is residual charge slowly discharging after previous application of voltage on the top electrode.

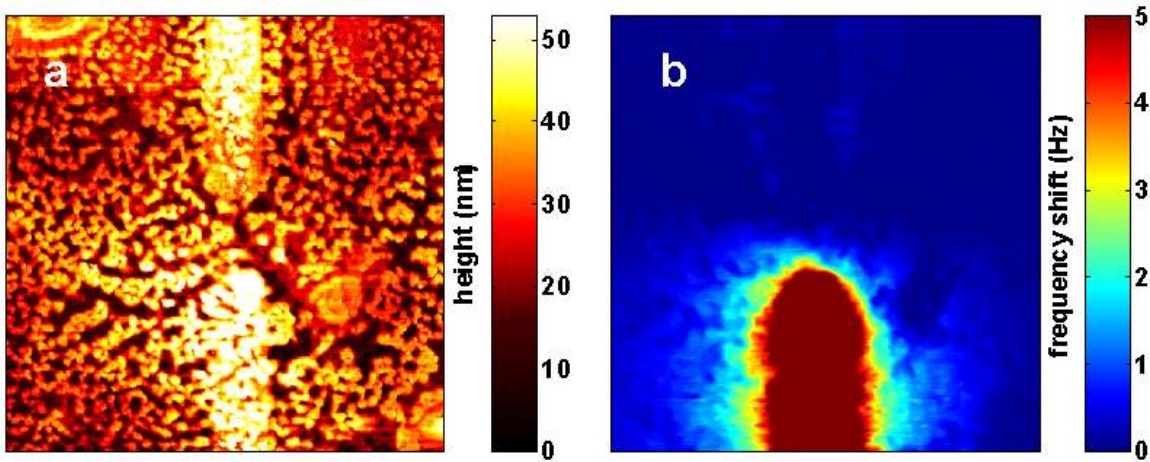


Figure 4.3. Inhomogeneous QD film formed after drop-casting and rapid drying. a) AFM height image. b) EFM frequency shift image with -10 V on the lower electrode and the top electrode and AFM tip grounded. (each image is $15 \mu\text{m} \times 15 \mu\text{m}$)²⁸

After annealing, the topography of the film remained relatively unchanged (Fig. 4.4a).

Now, although there was still no measurable current between the electrodes, there is a distinct charging pattern, indicating that some areas of the film contain a higher charge density and also implying that some areas are more well connected to the electrodes than others (Fig. 4.4b). The series of EFM images at increasing voltage magnitudes in Fig. 4.5 show a voltage dependence in the charging behavior.

After all AFM/EFM imaging was completed, the film was inspected at higher resolution in the TEM. The network structure observed in the AFM (as thick as $\sim 3\text{-}5$ QDs) proved to be multilayer regions separated by monolayers or voids (Fig. 4.4c,d). The QDs remained independent particles after annealing, but the inter-particle spacing was reduced to under 1 nm on average in multilayer regions (the nominal ligand length was ~ 2 nm). It is this reduction in spacing that improves the efficiency of tunneling between

particles and produces a conducting, rather than insulating, film. The unconstrained QD monolayers, however, exhibited inter-particle spacing > 1.8 nm.

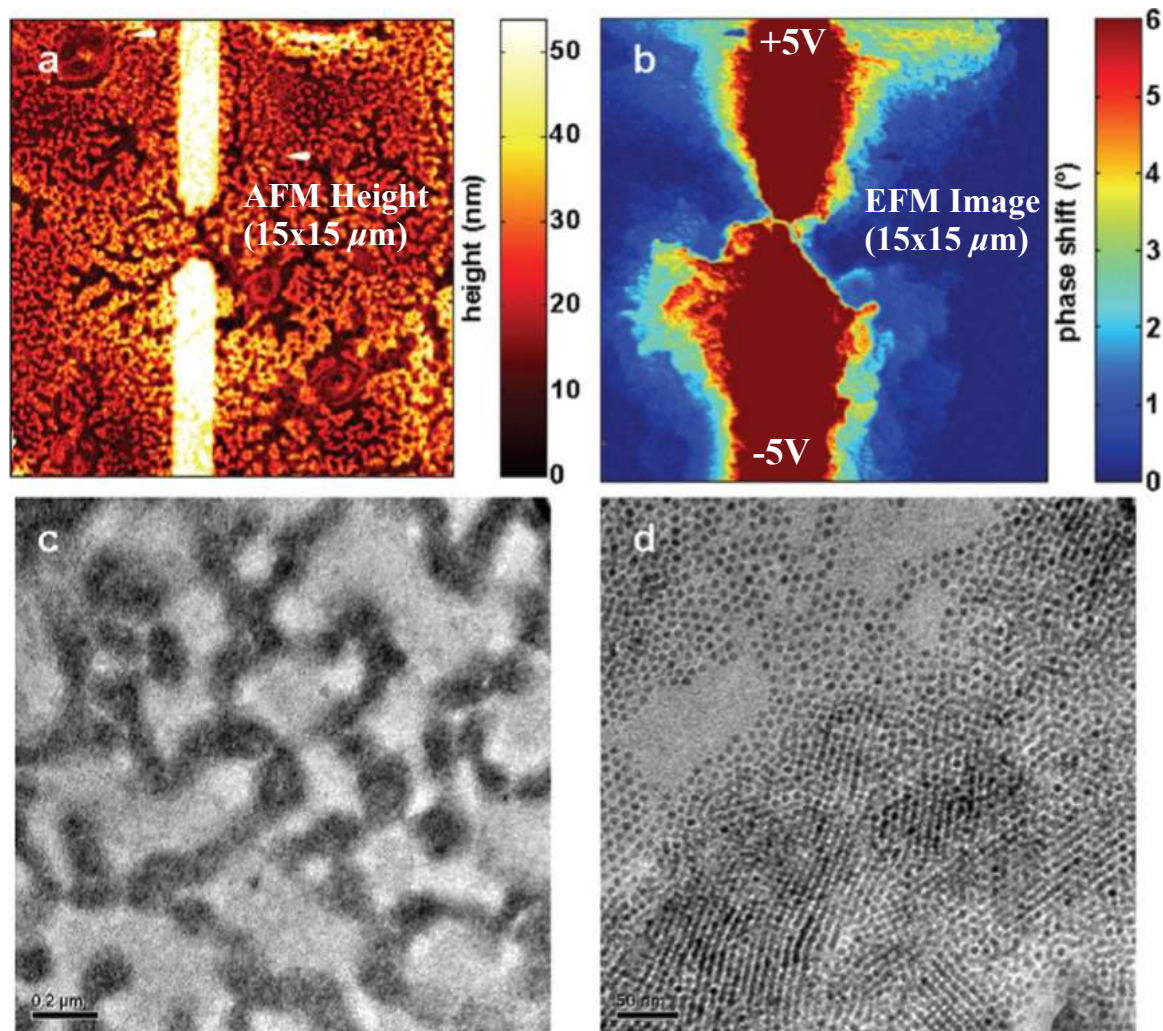


Figure 4.4. QD film after annealing. a) AFM height image, which looks very similar to the pre-annealed image. b) EFM phase shift image with +5 V applied to the top electrode and -5 V applied to the bottom electrode. c) Large-scale view of the QD network. d) Smaller-scale view showing that the dark areas in (c) are multilayer arrays separated by monolayers or voids.²⁸

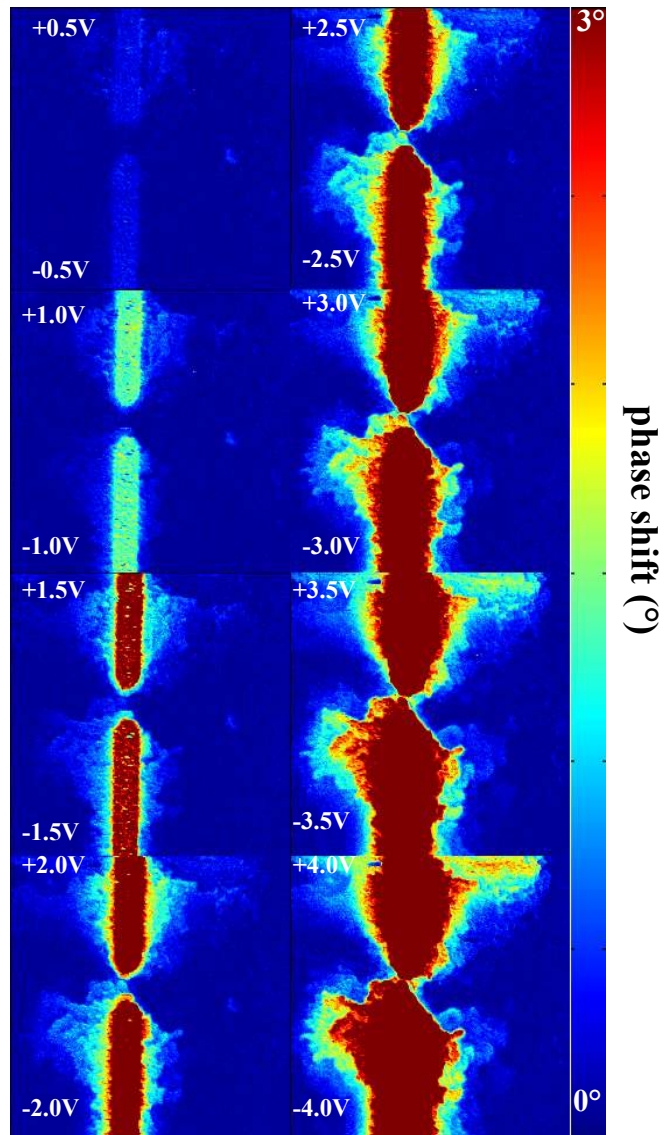


Figure 4.5. EFM images showing the voltage dependence of the charging behavior.²⁸

Inspection of over 30 areas where charge propagation appears limited showed that charge does not propagate past monolayer regions (Fig. 4.6). The larger inter-particle spacing in monolayers as compared to multi-layer regions, is one likely explanation for the limited charge transport. The contrast between charging behavior through multilayer and

monolayer regions is highlighted in Fig. 4.6 (f) and (e). Both regions connect thick patches of QDs, but in (f), where the spacing is tighter, charge can propagate, whereas in (e), where the spacing is larger, charge propagation comes to an abrupt halt.

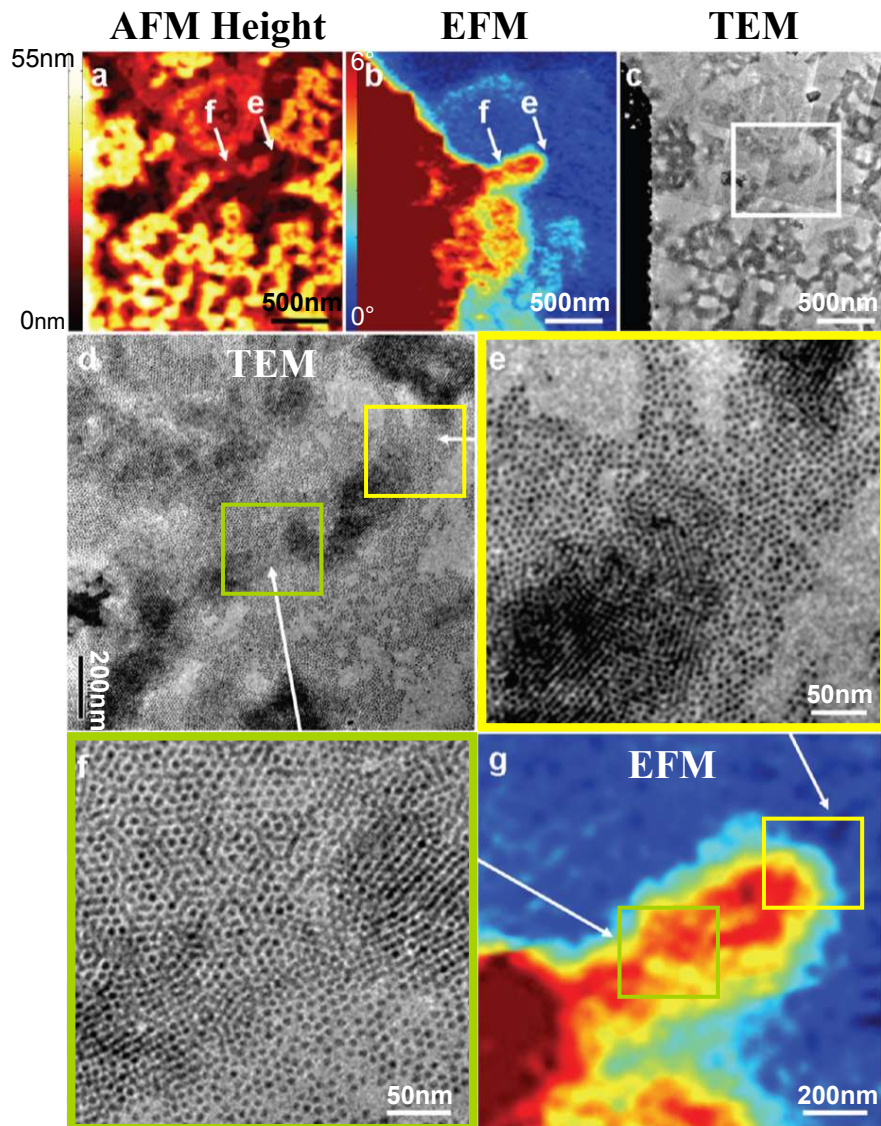


Figure 4.6. Series of AFM/EFM/TEM images showing limitations to charge propagation. a-c) Same-sized images of the right side of the electrode. d) and g) show a particularly conductive region, while f) show a TEM zoom-in image of a conductive junction between two multilayer regions, and e) shows an image of a non-conductive junction between two multilayer regions.²⁸

The wider electrode gap in Fig. 4.7 shows particularly nice examples of annealed PbSe superlattice structures separated by voids, cracks, and grain boundaries. Again, there was no measurable current through the film, despite the presence of multi-layer structures that connect the two electrodes. In some instances the lattice structure is disrupted near the electrode, clearly limiting charge transfer between the electrode and the superlattice. In many instances cracks limit conduction, while in other instances charge flow is halted by barely distinguishable grain boundaries between superlattices oriented in different directions. Fig. 4.7 d-f shows that even a narrow multi-layer constriction can present a limit to conduction. The overlaid TEM and EFM images in Fig. 4.8 and 4.9 help to show the large-scale correlation between structure and charging.

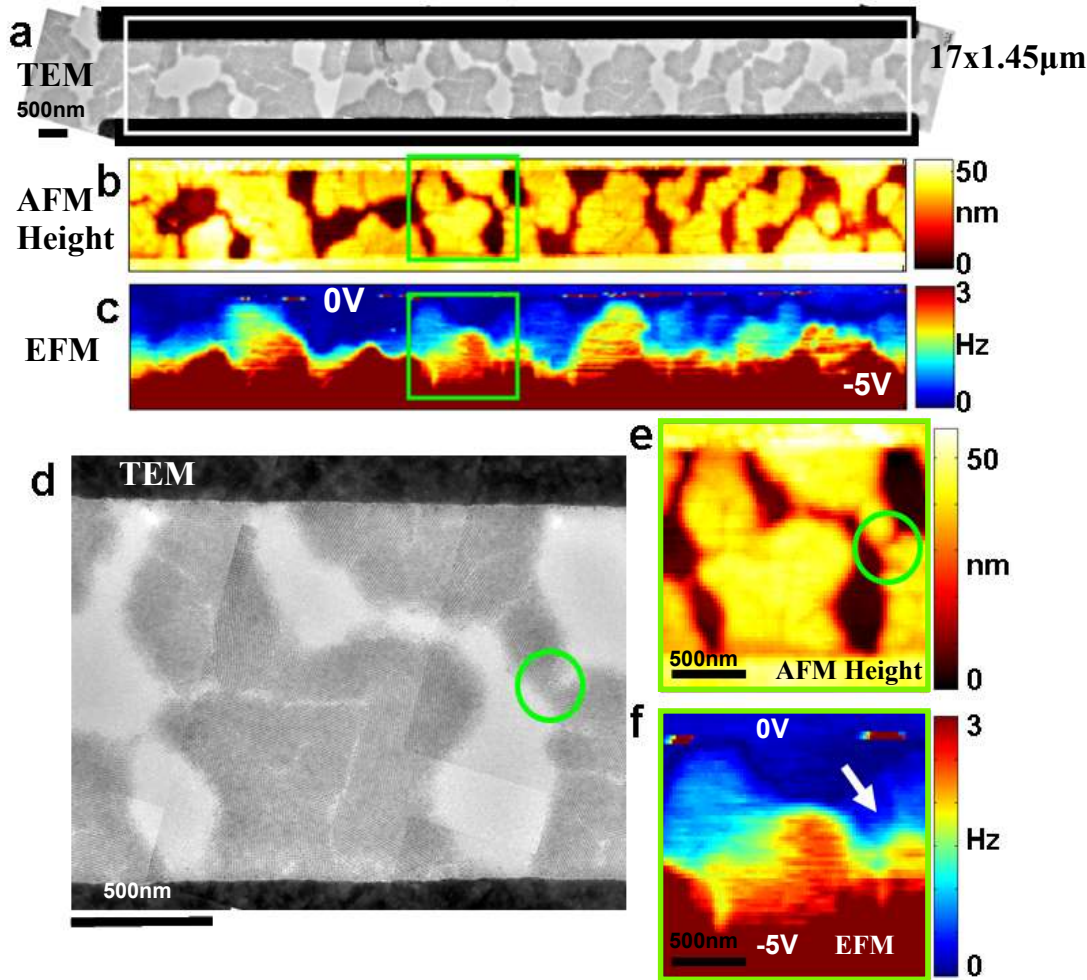


Figure 4.7. TEM/AFM/EFM images of a 17- μm -wide gap containing PbSe superlattice structures separated by voids, cracks, and grain boundaries. -5 V was applied to the bottom electrode, and both the tip and top electrode were grounded. d)-f) highlight a multi-layer junction that is not conductive. Gaps and grain boundaries in (d) also limit charge flow through a structure that appears to connect both electrodes.²⁸

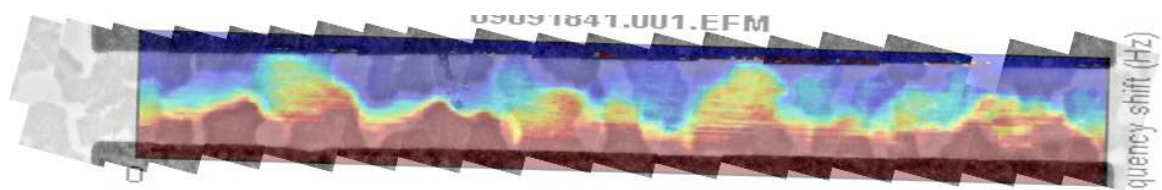


Figure 4.8. EFM image of the device overlaid on stitched TEM images.

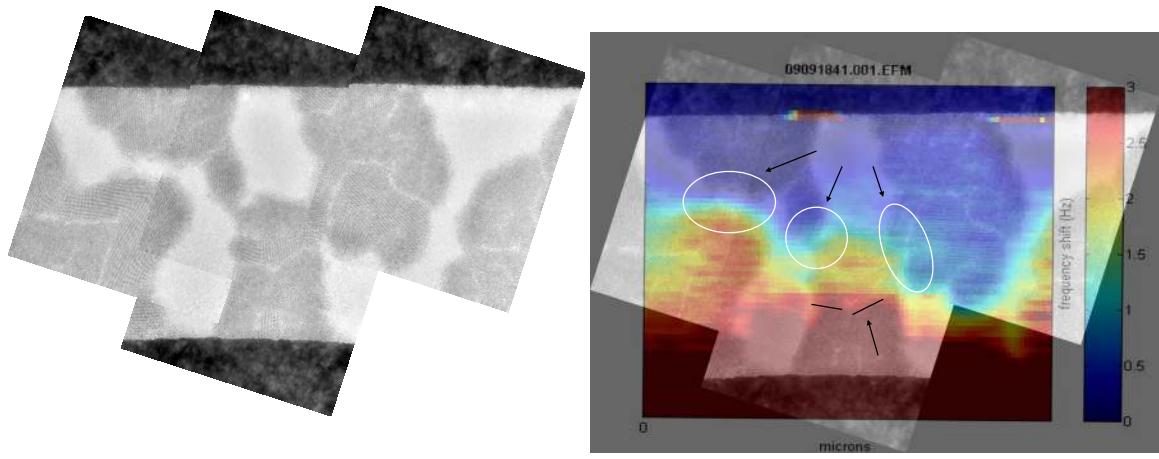


Figure 4.9. Another EFM overlay that allows for precise comparison between structural details seen in TEM and charge flow seen with EFM.

4.4 Conclusions

The combination of TEM, AFM, and EFM imaging allows us to correlate the microstructure of a sample with its transport behavior. We found that in inhomogeneous QD films, conduction was limited by monolayers, where QDs were more separated than in the close-packed multilayer regions. Even in devices where electrodes appear by AFM to be connected by multilayer ordered QD superlattices, EFM imaging revealed transport limitations, and TEM imaging showed that grain boundaries, lateral constrictions, and contact between the QD film and electrode were the limiting factors. This combination of measurements can be an effective way to assess the structural and transport modifications induced by a variety of film treatments, in addition to the annealing treatment used here.

4.5 References

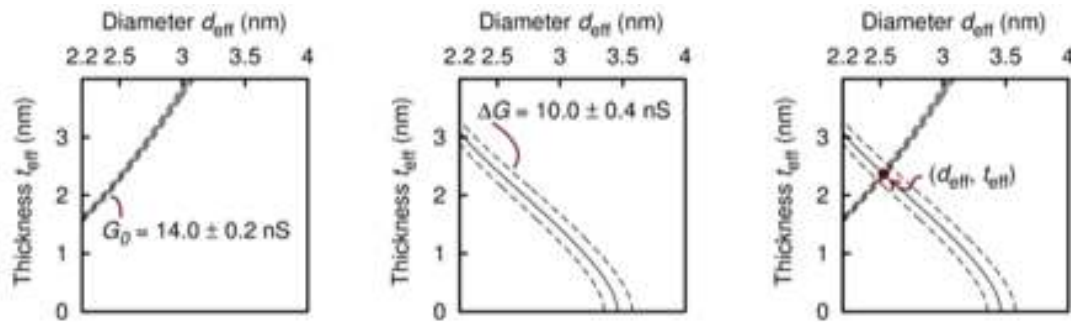
1. Alivisatos, A. P. Semiconductor Clusters, Nanocrystals, and Quantum Dots. *Science* **271**, 933–937 (1996).
2. Klimov, V. *Semiconductor and metal nanocrystals: Synthesis and electronic and optical properties.* (CRC Press, 2004).
3. Shevchenko, E. V., Talapin, D. V., Kotov, N. A., O'Brien, S. & Murray, C. B. Structural diversity in binary nanoparticle superlattices. *Nature* **439**, 55–59 (2006).
4. Drndić, M., Jarosz, M. V., Morgan, N. Y., Kastner, M. A. & Bawendi, M. G. Transport properties of annealed CdSe colloidal nanocrystal solids. *J. Appl. Phys.* **92**, 7498 (2002).
5. Talapin, D. V. & Murray, C. B. PbSe Nanocrystal Solids for n- and p-Channel Thin Film Field-Effect Transistors. *Science* **310**, 86–89 (2005).
6. Mentzel, T. *et al.* Charge transport in PbSe nanocrystal arrays. *Phys. Rev. B* **77**, 075316 (2008).
7. Porter, V., Mentzel, T., Charpentier, S., Kastner, M. & Bawendi, M. Temperature-, gate-, and photoinduced conductance of close-packed CdTe nanocrystal films. *Phys. Rev. B* **73**, 155303 (2006).
8. Yu, D., Wang, C., Wehrenberg, B. & Guyot-Sionnest, P. Variable Range Hopping Conduction in Semiconductor Nanocrystal Solids. *Phys. Rev. Lett.* **92**, 216802 (2004).
9. Porter, V. J., Geyer, S., Halpert, J. E., Kastner, M. A. & Bawendi, M. G. Photoconduction in Annealed and Chemically Treated CdSe/ZnS Inorganic Nanocrystal Films. *J. Phys. Chem. C* **112**, 2308–2316 (2008).
10. Fischbein, M. D. & Drndić, M. CdSe nanocrystal quantum-dot memory. *Appl. Phys. Lett.* **86**, 193106 (2005).
11. Willis, L. J., Fairfield, J. A., Dadosh, T., Fischbein, M. D. & Drndić, M. Controlling Nanogap Quantum Dot Photoconductivity through Optoelectronic Trap Manipulation. *Nano Lett.* **9**, 4191–4197 (2009).

12. Jarosz, M., Porter, V., Fisher, B., Kastner, M. & Bawendi, M. Photoconductivity studies of treated CdSe quantum dot films exhibiting increased exciton ionization efficiency. *Phys. Rev. B* **70**, 195327 (2004).
13. Lifshitz, E. *et al.* Air-stable PbSe/PbS and PbSe/PbSexS1-x core-shell nanocrystal quantum dots and their applications. *J. Phys. Chem. B* **110**, 25356–25365 (2006).
14. Williams, K. J. *et al.* Strong Electronic Coupling in Two-Dimensional Assemblies of Colloidal PbSe Quantum Dots. *ACS Nano* **3**, 1532–1538 (2009).
15. Kang, M. S., Lee, J., Norris, D. J. & Frisbie, C. D. High Carrier Densities Achieved at Low Voltages in Ambipolar PbSe Nanocrystal Thin-Film Transistors. *Nano Lett.* **9**, 3848–3852 (2009).
16. Law, M. *et al.* Structural, optical, and electrical properties of PbSe nanocrystal solids treated thermally or with simple amines. *J. Am. Chem. Soc.* **130**, 5974–5985 (2008).
17. Luther, J. M. *et al.* Structural, optical, and electrical properties of self-assembled films of PbSe nanocrystals treated with 1,2-ethanedithiol. *ACS Nano* **2**, 271–280 (2008).
18. Murphy, J. E., Beard, M. C. & Nozik, A. J. Time-resolved photoconductivity of PbSe nanocrystal arrays. *J. Phys. Chem. B* **110**, 25455–25461 (2006).
19. Novikov, D. *et al.* Lévy statistics and anomalous transport in quantum-dot arrays. *Phys. Rev. B* **72**, 075309 (2005).
20. Morgan, N. *et al.* Electronic transport in films of colloidal CdSe nanocrystals. *Phys. Rev. B* **66**, 075339 (2002).
21. Viswanathan, R. & Heaney, M. Direct Imaging of the Percolation Network in a Three-Dimensional Disordered Conductor-Insulator Composite. *Phys. Rev. Lett.* **75**, 4433–4436 (1995).
22. Marchi, F., Dianoux, R., Smilde, H., Mur, P. & Comin, F. Characterisation of trapped electric charge carriers behaviour at nanometer scale by electrostatic force microscopy. *J. Electrostat.* **66**, 538–547 (2008).

23. Hu, Z., Fischbein, M. D. & Drndić, M. Local Charge Transport in Two-Dimensional PbSe Nanocrystal Arrays Studied by Electrostatic Force Microscopy. *Nano Lett.* **5**, 1463–1468 (2005).
24. Drndić, M. *et al.* Imaging the charge transport in arrays of CdSe nanocrystals. *Appl. Phys. Lett.* **83**, 4008–4010 (2003).
25. Bonnell, D. A. & Huey, B. L. *Scanning Probe Microscopy and Spectroscopy, Theory, Techniques and Applications*. (John Wiley and Sons, 2001).
26. Krauss, T. & Brus, L. Charge, Polarizability, and Photoionization of Single Semiconductor Nanocrystals. *Phys. Rev. Lett.* **83**, 4840–4843 (1999).
27. Cherniavskaya, O., Chen, L., Weng, V., Yuditsky, L. & Brus, L. E. Quantitative Noncontact Electrostatic Force Imaging of Nanocrystal Polarizability. *J. Phys. Chem. B* **107**, 1525–1531 (2003).
28. Fischbein, M. D., Puster, M. & Drndic, M. Monolayer suppression of transport imaged in annealed PbSe nanocrystal arrays. *Nano Lett.* **10**, 2155–2161 (2010).

Appendix

A. Effective diameter and thickness calculation



Eq. 1.3 is an equation for G_0 in terms of d and t . An equation for ΔG in terms of d and t can be obtained by substituting Eq. 1.3 and 1.4 into $\Delta G = G_0 - G_{\text{with molecule}}$. Each constant value of G_0 and ΔG can be thought of as an isoline in diameter-thickness space. Considering an experimentally measured value of G_0 and the corresponding ΔG , the crossing of the two isolines (i.e., the set of d and t that satisfy both equations) defines the

nano pore effective diameter and thickness (d_{eff} , t_{eff}). The above Figure illustrates an example of this procedure for experimental values of $G_0 = 14.0 \pm 0.2$ and $\Delta G = 10.0 \pm 0.4$. The left and center panels show isolines corresponding to G_0 and ΔG , respectively. Dashed lines indicate the estimated errors. The right panel shows the crossing of the two isolines. For this case $(d_{\text{eff}}, t_{\text{eff}}) = (2.5 \text{ nm}, 2.3 \text{ nm})$.

B. Complete datasets from STEM thinned pores

Nanopore	# of events (@ 500 mV)	G_o (nS) (%)	All-points histogram analysis, filtered	Shallow level AG (%) blocked	Shallow level AG (%) blocked	Lowest point per event analysis	% Blocked (AG / $G_o \times 100$)	Shallow level AG (%) blocked	Shallow level AG (%) blocked	Nanopore dimensions	Film thickness (nm)	Film thickness EELS (nm) fitted	Nanopore diameter (nm)	Shallow TEM (nm)	Nanopore diameter (nm)	Film thickness (nm)	Error in G_o (nS) (RMS noise from 1s data @ 500 mV)	Error in G_o (nS) (RMS noise from 1s data @ 500 mV)	Error in G_o (nS) (stat. dev. from histogram)	Scaling G_o (nS)	Scaled G_o (nS)
S1	744	8.9	85.2	7.6	—	—	92.8	8.3	—	—	4.1	2.3	—	—	—	4.0	0.04	0.2	12.16	7.9	6.8
S2 – folding	712	23.4	22.4 and 69	5.2	—	—	36.3 and 79	9.0	—	—	5.3	4.2	—	—	3.9	0.1	0.6	12.16	20.8	4.7	
S3	139	11.6	72.3	8.4	55.6	6.4	79.8	9.3	—	—	3.1	2.5	—	—	3.1	0.2	0.2	12.16	10.3	7.4	
S4	870	6.6	58.4	3.9	—	—	65.5	4.3	—	—	3.2	2.8	—	—	9.1	0.2	0.1	12.16	5.9	3.4	
S5	1835	14.0	63.9	8.9	30.0	4.2	71.4	10.0	38.2	5.3	4.0	2.6	—	—	2.6	0.2	0.2	12.16	12.4	7.9	
S6	182	5.8	69.4	4.0	54.6	3.2	89.4	5.2	—	—	3.3	2.6	—	—	9.1	0.1	0.1	12.16	5.1	3.6	
S7	3044	21.0	35.3	7.4	19.1	4.0	41.6	8.7	24.0	5.0	4.7	3.4	—	—	2.5	0.3	0.4	12.16	18.7	6.6	
S8	1312	29.1	25.1	7.3	10.8	3.1	29.1	8.5	14.0	4.1	2.5	3.8	—	—	1.7	0.4	0.4	12.16	23.8	6.5	
S9	1408	10.1	80.8	8.2	42.9	4.3	95.0	9.6	66.5	6.7	2.5	—	—	—	3.5	0.1	0.2	12.16	9.0	7.3	
S10	443	18.7	57.7	10.8	25.9	4.8	62.5	11.7	31.6	5.9	—	2.7	—	—	1.5	0.2	0.4	12.0	16.8	9.7	
S11	493	14.5	73.1	10.6	42.4	6.2	82.6	12.0	55.1	8.0	2.6	2.5	—	—	2.0	0.1	0.2	12.2	12.8	9.4	
S12	3911	24.9	41.2	10.2	16.7	4.1	43.8	10.9	19.9	4.9	4.6	3.0	1.4	—	1.1	0.2	0.4	12.2	22.0	9.1	